FLUID ANTENNA MULTIPLE ACCESS UNDER NAKAGAMI-m FADING CHANNELS

PAULO RODRIGO DE MOURA

TESE DE DOUTORADO
EM ENGENHARIA ELÉTRICA

DEPARTAMENTO DE ENGENHARIA ELÉTRICA

FACULDADE DE TECNOLOGIA

UNIVERSIDADE DE BRASÍLIA

UNIVERSIDADE DE BRASÍLIA
FACULDADE DE TECNOLOGIA
DEPARTAMENTO DE ENGENHARIA ELÉTRICA

FLUID ANTENNA MULTIPLE ACCESS UNDER NAKAGAMI-m FADING CHANNELS

PAULO RODRIGO DE MOURA

ORIENTADOR: UGO SILVA DIAS
COORIENTADOR: HUGERLES SALES SILVA

TESE DE DOUTORADO EM ENGENHARIA ELÉTRICA

PUBLICAÇÃO: PPGEE 221/26
BRASÍLIA/DF: MAIO/2026

Universidade de Brasília
Faculdade de Tecnologia
Departamento de Engenharia Elétrica

Fluid Antenna Multiple Access under Nakagami-m Fading Channels

Paulo Rodrigo de Moura

TESE DE DOUTORADO SUBMETIDA AO PROGRAMA DE PÓS-GRADUAÇÃO EM ENGENHARIA ELÉTRICA DA UNIVERSIDADE DE BRASÍLIA COMO PARTE DOS REQUISITOS NECESSÁRIOS PARA A OBTENÇÃO DO GRAU DE DOUTOR.

APROVADA POR:

Ugo Silva Dias, Doutor (UnB)
(Orientador)

Hugerles Sales Silva, Doutor (UnB)
(Coorientador)

Richard Demo Souza, Doutor (UFSC)
(Examinador Externo)

José Carlos Marinello Filho, Doutor (UTFPR)
(Examinador Externo)

Robson Domingos Vieira, Doutor (UnB)
(Examinador Interno)

Brasília/DF, 15 de maio de 2026.

FICHA CATALOGRÁFICA

DE MOURA, PAULO RODRIGO

Fluid Antenna Multiple Access under Nakagami-m Fading Channels. [Brasília/DF] 2026.

xxvi, 114p., 210 x 297 mm (ENE/FT/UnB, Doutor, Tese de Doutorado, 2026).

Universidade de Brasília, Faculdade de Tecnologia, Departamento de Engenharia Elétrica.

1. Fluid antenna system (FAS)	2. Fluid antenna multiple access (FAMA)
3. Nakagami-m fading	4. Spatial block-correlation
5. Outage probability	6. Multiplexing gain
7. Sixth generation (6G) networks	8. Maximum ratio transmission (MRT)
I. ENE/FT/UnB	II. Título (série)

REFERÊNCIA BIBLIOGRÁFICA

DE MOURA, P. R. (2026). Fluid Antenna Multiple Access under Nakagami-m Fading Channels. Tese de Doutorado, Publicação PPGEE 221/2026, Departamento de Engenharia Elétrica, Universidade de Brasília, Brasília, DF, 114p.

CESSÃO DE DIREITOS

AUTOR: Paulo Rodrigo de Moura

TÍTULO: Fluid Antenna Multiple Access under Nakagami-m Fading Channels.

GRAU: Doutor ANO: 2026

É concedida à Universidade de Brasília permissão para reproduzir cópias desta Tese de Doutorado e para emprestar ou vender tais cópias somente para propósitos acadêmicos e científicos. O autor reserva outros direitos de publicação e nenhuma parte deste trabalho pode ser reproduzida sem autorização por escrito do autor.

Paulo Rodrigo de Moura

Universidade de Brasília (UnB)

Campus Darcy Ribeiro

Faculdade de Tecnologia - FT

Departamento de Engenharia Elétrica (ENE)

Brasília - DF, CEP 70919-970

In loving memory of my father Pedro and mother Maria José (Marisa). You taught me the value of education, perseverance, and integrity. Although you are not here to celebrate this milestone, your presence remains in every achievement and every challenge overcome. This thesis is dedicated to you, with love that transcends time and absence.

ACKNOWLEDGEMENTS

I express my gratitude to the National Telecommunications Agency (Anatel) for the indispensable institutional support provided throughout the course of my doctoral studies, and to the Coordination for the Improvement of Higher Education Personnel (CAPES) for ensuring access to the scientific journals that were fundamental to the development of this thesis.

I also extend my thanks to the University of Brasília (UnB), in particular the Department of Electrical Engineering, as well as to my supervisors, Professors Ugo Dias and Hugerles Silva, and to Professors Higo Thaian, Daniel Guerreiro and Kleber Melo, for their guidance and academic contributions.

Furthermore, I acknowledge the academic collaboration of Professors Rausley Souza and Felipe Figueiredo from the National Institute of Telecommunications (Inatel) and my colleague at Anatel, Alexandre Moraes.

Special thanks to my former master supervisor, Professor Franklin C. Silva, whose encouragement and belief in my potential inspired me to pursue a PhD.

I extend my sincere acknowledgments to the staff and students of UnB, in particular to the administrative professional Vera Simões and to the former students Pedro Alvim, Pedro Dornelas, Rômulo Santos, Douglas Aguiar and Roberto Brito.

My deepest thanks go to my family, especially my siblings Ana Catarina, Patrícia, Jacqueline, Aurélio, and Alexandre (*in memorian*), and to my friends, whose care and friendship made my journey smoother.

Endless gratitude to my wife, Rafaela, and my daughters, Maria Clara and Sofia, whose unwavering patience, steadfast support, and love made this journey possible.

ABSTRACT

Fluid antenna systems (FASs) have recently emerged as a key enabler for the forthcoming sixth generation (6G) of wireless communication systems. The performance benefits of fluid antennas have been explored in multiuser systems in an approach known as fluid antenna multiple access (FAMA). This thesis investigates FAMA under Nakagami-m fading channels, considering different correlation models. For slow FAMA, considering the constant correlation model, exact expressions for the outage probability (OP) based on the signal-to-interference ratio (SIR) or the signal-to-interference plus noise ratio (SINR) are presented. An upper bound for the SIR-based OP and an approximate expression for the SINR-based OP are derived using the Gauss-Laguerre quadrature approach. Bounds for the multiplexing gain are also derived. Considering the new and realistic spatial block-correlation model, this thesis also investigates slow, fast, and opportunistic FAMA under the effect of Nakagami-m fading channels. For this correlation model, expressions for the OP, based on the SIR, are derived for slow FAMA. Interestingly, we provide mathematical relationships that allow the expressions of fast FAMA to be obtained from slow FAMA. Multiplexing gains are presented for an opportunistic FAMA (O-FAMA) network for both slow and fast FAMA scenarios. Additionally, the analysis is extended to networks that employ maximum ratio transmission (MRT) precoding at base stations (BSs), called MRT-FAMA networks. The analytical results are validated through Monte Carlo simulations, under various channel and system parameters. To the best of author's knowledge, the expressions derived in this thesis are original.

Keywords: FAMA, FAS, MRT, multiplexing gain, Nakagami-m fading, OP, opportunistic scheduling, SINR, SIR, spatial block-correlation.

RESUMO

Título: Acesso Múltiplo por Antenas Fluidas em Canais com Desvanecimento Nakagami-m.

Os sistemas de antenas fluidas (FASs) surgiram recentemente como um catalisador essencial para a próxima sexta geração (6G) de sistemas de comunicação sem fio. Os benefícios de desempenho das antenas fluidas foram explorados em sistemas multiusuário, em uma abordagem conhecida como acesso múltiplo por meio de antenas fluidas (FAMA). Esta tese investiga o FAMA sob desvanecimento Nakagami-m, considerando dois modelos de correlação. Para o FAMA com seleção lenta de canais (FAMA lento), considerando o modelo de correlação constante, são apresentadas as expressões exatas para a probabilidade de interrupção (OP) com base na relação sinal-interferência (SIR) ou na relação sinal-interferência mais ruído (SINR). Um limitante superior para OP, baseado em SIR, e uma expressão aproximada para a OP, baseada em SINR, são derivados usando a abordagem da quadratura de Gauss-Laguerre. Os limitantes para o ganho de multiplexação também são deduzidos. Para o novo e realista modelo de correlação espacial por blocos, esta tese investiga o FAMA com seleção lenta, rápida e oportunista de canais, chamados de: FAMA lento, rápido e oportunista, respectivamente, sob o efeito do desvanecimento Nakagami-m. Para esse modelo de correlação, expressões para a OP, com base na SIR, são derivadas para o FAMA lento. Interessantemente, foram encontradas relações matemáticas que permitem que as expressões do FAMA rápido sejam obtidas a partir das expressões do FAMA lento. Os ganhos de multiplexação para uma rede FAMA oportunista (O-FAMA) são apresentados para cenários com FAMA lento e FAMA rápido. A análise é então estendida para redes FAMA cujas estações rádio-base (BSs) utilizam pré-codificação do tipo transmissão com razão máxima (MRT), essas redes são chamadas de MRT-FAMA. Os resultados analíticos são validados por meio de simulações de Monte Carlo, sob vários parâmetros. Até onde se estende o conhecimento do autor, as expressões derivadas nesta tese são originais.

Palavras-chave: Correlação espacial por blocos, desvanecimento Nakagami-m, escalonamento oportunista, FAMA, FAS, ganho de multiplexação, MRT, OP, SINR, SIR.

TABLE OF CONTENTS

LIST OF FIGURES

LIST OF SYMBOLS

$r_n^{(u)}$	Received signal by the u-th user at n-th port
r_n	Received signal at n-th port
s_u	Transmitted symbol to the u-th user
$s_{\tilde{u}}$	Transmitted symbol to the $\tilde{u}$-th user
s	Transmitted symbol to a user
s_i	Transmitted symbol by the i-BS in an MRT-FAMA network
σ_s^2	Average power of the transmitted symbol
h_n	Channel coefficient at the n-th port
$h_n^{(u,u)}$	Channel between the BS and the n-th port of the u-th user
$h_n^{(\tilde{u},u)}$	Interference channel at the n-th port of the u-th user
$\widetilde{h}_n^{(u)}$	Total interference signal at the n-th port of the u-th user
$\tilde{h}_n$	Overall channel at the n-th port of a user in an MRT-FAMA network
h_{nk}	Channel from the k-th fixed antenna of the BS to the n-th port of a user in an MRT-FAMA network
$\tilde{h}_n^{(i)}$	Interference channel at the n-th port of a user from i-th BS in an MRT-FAMA network
$\tilde{h}_n^{(s)}$	Total interference channel at the n-th port of a user in an MRT-s-FAMA network
$\tilde{h}_n^{I}$	Total interference signal at the n-th port of a user in an MRT-f-FAMA network

$2\sigma^2$	Variance of the complex Gaussian RVs g_{knl} or $g_{nl}^{(u,u)}$, with $\sigma_u = \sigma, \forall u$
m	Fading parameter of the Nakagami-m RVs $\lvert h_n^{(u,u)}\rvert$, $\lvert h_{kn}\rvert$ or $\lvert\tilde{h}_n^{(i)}\rvert$
Ω	Scale parameter of the Nakagami-m RV $\lvert h_n^{(u,u)}\rvert$
$m_{\tilde{u}}$	Fading parameter of the Nakagami-m RV $\lvert h_n^{(\tilde{u},u)}\rvert$
$\Omega_{\tilde{u}}$	Scale parameter the Nakagami-m RV $\lvert h_n^{(\tilde{u},u)}\rvert$
m_s	Fading parameter of the Nakagami-m RV $\lvert\tilde{h}_n^{(s)}\rvert$
Ω_s	Scale parameter of the Nakagami-m RV $\lvert\tilde{h}_n^{(s)}\rvert$
m_f	Fading parameter of the Nakagami-m RV $\lvert\tilde{h}_n^{I}\rvert$
Ω_f	Scale parameter of the Nakagami-m RV $\lvert\tilde{h}_n^{I}\rvert$
$\widetilde{m}$	Fading parameter of the Nakagami-m RV $\lvert\widetilde{h}_n^{(u)}\rvert$
$\widetilde{\Omega}$	Scale parameter of the Nakagami-m RV $\lvert\widetilde{h}_n^{(u)}\rvert$
$\eta_n^{(u)}$	Complex AWGN at the n-th port of the u-th user
η_n	Complex AWGN at the n-th port of a user
σ_η^2	Average noise power
Υ	Average received SNR
U	Number of users in a FAMA network or number of BS $-$ 1 in an MRT-FAMA network
$\widetilde{U}$	Sum of the fading parameters of all interferers, $\widetilde{U} = \sum_{\tilde{u}=1,\,\tilde{u}\neq u}^{U} m_{\tilde{u}}$
$\widehat{U}$	Parameter of a f-FAMA network, $\widehat{U} = \widetilde{U}/\widetilde{m}$
$U^\star$	Optimal number of users that maximizes multiplexing gain
M	Poll of users for an O-FAMA network, such as $M \geq U$
α	Path loss exponent in an MRT-FAMA network
d_0	Distance from the BS to the served user in an MRT-FAMA network
d_i	Distance from the i-th interference BS to a non-served user in an MRT-FAMA network

d	Distance from a interference BS to a non-served user, with $d_i = d, \forall i$
K	Number of FPAs of a BS for an MRT-FAMA network
N	Number of ports of a fluid antenna
$n^\star$	Optimal port in a fluid antenna
$W\lambda$	Size of a fluid antenna, where W is the normalized size and λ is the wavelength
δ	Common power correlation coefficient between ports in an FA
$\boldsymbol{\Sigma}$	Correlation matrix
$(\boldsymbol{\Sigma})_{n,k}$	Element of the matrix $\boldsymbol{\Sigma}$ located at the n-th row and k-th column
$\mathrm{diag}(\rho_1, \ldots, \rho_N)$	Diagonal matrix with elements $\{\rho_1, \ldots, \rho_N\}$ in the diagonal
$\mathrm{trace}(\mathbf{A})$	Trace of the matrix $\mathbf{A}$ (sum of elements in the main diagonal of $\mathbf{A}$)
$\mathbf{A}^H$	Hermitian operator (transpose and conjugate of the matrix $\mathbf{A}$)
ρ_{th}	Threshold for an eigenvalue of $\boldsymbol{\Sigma}$ to be considered dominant
$\widehat{\boldsymbol{\Sigma}}$	Block-diagonal matrix
$\mathbf{A}_b$	Sub-matrix (or block) of $\widehat{\boldsymbol{\Sigma}}$ with dimension $L_b \times L_b$. It is a correlation matrix with all non-diagonal elements equal to δ_b
b	Block index
δ_b	Element of the common correlation matrix A_b
B	Number of blocks (or sub-matrices) of $\widehat{\boldsymbol{\Sigma}}$, $N = \sum_{b=1}^{B} L_b$
L_b	Length (number of ports) of block b
$\mathcal{N}_b$	Set of port indices corresponding to block b
$\mathrm{J}_\nu(\cdot)$	Bessel function of the first kind and order ν
$j_0(\cdot)$	Spherical Bessel function of the first kind
$\mathrm{I}_\nu(\cdot)$	Modified Bessel function of the first kind and order ν
$\mathcal{I}(\cdot\,,\cdot)$	Regularized incomplete beta function

$\Gamma(\cdot)$	Gamma function
$\Gamma(\cdot\,,\cdot)$	Lower incomplete Gamma function
$\mathrm{Q}_\nu(\cdot\,,\cdot)$	Marcum-Q function of order ν
$\lfloor x \rfloor$	Floor function, the largest integer $\leq x$
$(x)_n$	Pochhammer symbol
$\mathcal{L}\{\cdot\}$	Laplace transform
$L_n(x)$	Laguerre polynomial of order n
$L_{n_I}^{\beta}(x)$	Generalized Laguerre polynomial of order n_I and parameter β
x_i	i-th root of the Laguerre (or generalized Laguerre) polynomial of order n_I
w_i	Weight corresponding to root x_i of the GLQ (or generalized GLQ) approximation
n_I	Number of roots of the GLQ (or generalized GLQ) approximation, with roots denoted by x_i
γ	SIR, SNR or SINR threshold
P_{out}	SIR-based, SNR-based or SINR-based outage probability
$\mathcal{G}_m$	Multiplexing gain
R	Transmission rate
$\mathrm{Prob}(\mathcal{A})$	Probability of the event $\mathcal{A}$
$\mathrm{Prob}(\mathcal{A}\,\vert\,\mathcal{M})$	Conditional probability of the event $\mathcal{A}$ assuming $\mathcal{M}$
$X \sim p_X(x)$	RV X has the distribution $p_X(x)$
$\mathcal{N}(\mu, \sigma^2)$	Real Gaussian RV with mean μ and variance σ^2
$\mathcal{CN}(\mu, \sigma^2)$	Complex Gaussian RV with mean μ and variance σ^2
$F_X(x)$	Cumulative distribution function
$p_X(x)$	Probability density function
$\mathbb{E}[X]$	Expected value (or mean) of the RV X

$\mathbb{V}[X]$	Variance of the RV X
$\lvert\cdot\rvert$	Absolute value
$\lVert\cdot\rVert_2$	Euclidean norm
$(a)^+$	Max$\{0, a\}$
$\binom{n}{k}$	Binomial coefficient
j	Imaginary unit, $j = \sqrt{-1}$
$\mathbb{R}$	Set of real numbers
$\mathbb{C}$	Set of complex numbers

GLOSSARY

1D-FAS	One-Dimensional Linear FAS
2D-FAS	Two-Dimensional Planar FAS
2G	Second Generation of Mobile Communication Systems
3G	Third Generation of Mobile Communication Systems
3GPP	Third Generation Partnership Project
4G	Fourth Generation of Mobile Communication Systems
5G	Fifth Generation of Mobile Communication Systems
5G-NR	5G New Radio
6G	Sixth Generation of Mobile Communication Systems
AI	Artificial Intelligence
AoA	Angle of Arrival
AoD	Angle of Departure
AWGN	Additive White Gaussian Noise
BLER	Block Error Rate
BS	Base Station
CAPEX	Capital Expenditure
CDF	Cumulative Distribution Function
cGAN	conditional Generative Adversarial Network
CCN	Content-Centric Network

CSI	Channel State Information
CUMA	Compact Ultra-Massive Antenna Array
DoF	Degree of Freedom
EE	Energy Efficiency
FA	Fluid Antenna
FAMA	Fluid Antenna Multiple Access
FAS	Fluid Antenna System
f-FAMA	Fast Fluid Antenna Multiple Access
FPA	Fixed-Position Antenna
FPGA	Field-Programmable Gate Array
FRIS	Fluid Reconfigurable Intelligent Surface
FSO-RF	Free-Space Optical-Radio Frequency
GLQ	Gauss-Laguerre Quadrature
HK-FAMA	Han-Kobayashi Fluid Antenna Multiple Access
HRLLC	Hyper-Reliable and Low-Latency Communication
IEEE	Institute of Electrical and Electronics Engineers
IEEE ComSoc	IEEE Communications Society
i.i.d.	independent and identically distributed (RVs)
IEEE ICC	IEEE International Conference on Communications
IMT	International Mobile Telecommunications
IMT-2030	IMT for 2030 and beyond
IoT	Internet of Things
IRS	Intelligent Reflecting Surface
ISAC	Integrated Sensing and Communication

ISI	Inter-Symbol Interference
ITU	International Telecommunication Union
JSCC	Joint Source-Channel Coding
L3SCR	Low-Sample-Size Sparse Channel Reconstruction
LMFA	Liquid-Metal Fluid Antenna
LSTM	Long Short-Term Memory
LS	Least Square
MIMO	Multiple-Input Multiple-Output
MIMO-FAS	Multiple-Input Multiple-Output FAS
MA	Movable Antenna
MFA	Meta-Fluid Antenna
ML	Machine Learning
MLE	Maximum Likelihood Estimation
mmWave	Millimeter-Wave
MRC	Maximum Ratio Combining
MRT	Maximum Ratio Transmission
MSE	Mean Squared Error
MU	Mobile User
NOMA	Non-Orthogonal Multiple Access
O-FAMA	Opportunistic Fluid Antenna Multiple Access
OFDMA	Orthogonal Frequency-Division Multiplexing
OMP	Orthogonal Matching Pursuit
OP	Outage Probability
OPEX	Operational Expenditure
PCB	Printed Circuit Board

PDF	Probability Density Function
PIN diode	Positive-Intrinsic-Negative diode
PBFA	Pixel-Based Fluid Antenna
RF	Radio Frequency
RIS	Reconfigurable Intelligent Surface
RSMA	Rate-Splitting Multiple Access
RV	Random Variable
SBL	Sparse Bayesian Learning
SBS	Small-Cell Base Station
SC	Selection Combining
SDO	Standards Development Organization
s-FAMA	Slow Fluid Antenna Multiple Access
SIC	Successive Interference Cancellation
SINR	Signal-to-Interference plus Noise Ratio
SIR	Signal-to-Interference Ratio
SISO-FAS	Single-Input Single-Output FAS
SNR	Signal-to-Noise Ratio
SIW	Substrate-Integrated Waveguide
TAS	Traditional Antenna System
TDD	Time-Division Duplexing
TDL	Tapped Delay Line
UAV	Unmanned Aerial Vehicle
UE	User Equipment
UN	United Nations

CHAPTER 1

INTRODUCTION

1.1 CONTEXT AND MOTIVATION

In recent years, mobile communications have become deeply embedded in everyday life that it is difficult to imagine a typical day without a mobile phone near us, from the time we wake-up to the moment we go to sleep. For younger generations, this may seem natural, but it has not always been this way. We are currently living in the era of fifth generation (5G) of mobile communication. And although a great technological evolution made it possible for us to reach this point, the sixth generation (6G) of mobile communication is being planned, proposed, and studied by industry, academia [1] and standardization bodies [2]. This ongoing evolution is driven by the growing requirements of an increasingly interconnected world, in which the Internet functions as an ubiquitous socio-technical infrastructure and mobile phones have become integral components of individuals' everyday lives and social environments.

Regarding mobile technologies, numerous transformative innovations have emerged over the past decades. In 2G, advances in coding, digital modulation, and routing protocols signaled the onset of the packet-switching era [3]. Subsequently, inspired by the seminal work of Paulraj and Kailath [4], 3G was propelled by the adoption of multiple-input multiple-output (MIMO) techniques [5, 6, 7, 8] together with spread spectrum methods [9, 10], enabling, for the first time, multimedia communication over wireless links. Later, 4G introduced a shift from single-link MIMO to multiuser MIMO [11, 12, 13, 14, 15], which has further progressed into massive MIMO in 5G systems [16, 17].

The 6G networks are also called IMT-2030 (International Mobile Telecommunications for 2030 and beyond) by the International Telecommunication Union (ITU), which recently published a framework and objectives for its development [2]. The TKμ extreme-connectivity paradigm, first articulated for 6G in [18], specifies an ambitious performance target characterized by a peak data rate of 1 Tbps, a spectral efficiency of 1 kbps/Hz, and an end-to-end latency on the order of 1 μs.

Historically, each new mobile generation has required a significant physical-layer breakthrough (e.g., analog to digital, circuit to packet switching, single- to multi-antenna, and single- to multiuser processing). In line with this pattern, 6G will need to further increase the physical-layer degrees of freedom (DoFs) to satisfy future performance demands. The development of novel mobile technologies is essential to achieve emerging performance targets and address the increasing demands of an interconnected society.

The fundamental resource enabling the mobile communications industry is the electromagnetic spectrum, which serves a role analogous to that of railway infrastructure in terrestrial transport systems. With high demand, spectrum pricing is a common industry concern [19]. As the lower-frequency bands are already heavily utilized and mobile data traffic continues to grow, a natural evolutionary direction is the exploitation of higher-frequency bands to meet future capacity requirements.

The increasing data-rate demands push mobile systems to higher-frequency bands, especially in millimeter-wave (mmWave), e.g. 24–28 GHz and 37–43.5 GHz, which can deliver very high throughput in short-range hotspots such as stadiums or malls [20, 21]. However mmWave are ill-suited for wide-area mobile coverage. Compared with 4G, 5G at mmWave has shorter range and significantly higher power consumption per base station (BS), with operators expecting up to three times more BSs and three times the power use to achieve equivalent coverage. The mmWave channels are highly directional, offering antenna gain but making performance sensitive to beam misalignment and requiring line-of-sight links; they also lose the rich fading that supports spatial multiplexing at lower frequencies. The primary barrier for operators is deployment cost. According to [22], for 95 mmWave gNodeB units, the total cost is about US$ 12 million in ten years, considering the initial capital expenditure (CAPEX) and ten years of operational expenditure (OPEX). With more BS, 5G networks will likely consume more energy than 4G [23]. The academic community is also investigating even higher frequency bands, above 100 GHz, called THz bands [24], which will probably result in increased network densification [25].

A growing body of research is dedicated to designing sophisticated network architectures that are enabled and enhanced by artificial intelligence (AI) and various learning-based paradigms [26, 27, 28]. These studies explore how AI-driven algorithms can be deeply integrated into network control, management, and optimization processes. However, it is important to clearly distinguish between the enabling role of AI and the communication technologies themselves: although AI provides an extremely powerful framework for tasks such as network optimization, intelligent control, and adaptive resource allocation in wireless systems, AI itself does not constitute a wireless communication technology or a physical-layer transmission mechanism.

Non-orthogonal multiple access (NOMA) leverages successive interference cancellation (SIC) at the user equipment (UE) to enhance downlink throughput. The concept was formally introduced in 2013 [29, 30], although earlier considerations of NOMA can be traced back to 2006 [31]. Subsequently, it was further established and disseminated through fundamental analytical results, and the scheme gained significant attention due to its potential to support massive connectivity. This is achieved by allowing multiple user signals to overlap within the same time–frequency resources and separating them via SIC, thereby enabling highly efficient spectrum reuse and increased aggregate data rates [32]. Despite these advantages, NOMA and its generalization, rate-splitting multiple access (RSMA) [33], constitute theoretically capacity-achieving strategies for scenarios with massive connectivity but require substantial implementation complexity. In particular, user equipment must perform advanced multiuser detection (typically SIC), while the BS must execute sophisticated optimization procedures for power allocation, user clustering, and accurate channel state information (CSI) acquisition. Owing to this overall complexity, NOMA was not standardized in 5G, and, even if incorporated into prospective 6G systems, it is anticipated that it will be applied to only a limited number of users per resource block.

To advance in the state-of-the-art of physical-layer design, the fluid antenna system (FAS) has emerged as a promising paradigm, allowing adaptive reconfigurability in both the position and structural configuration of the antenna and thus substantially improving available spatial DoFs [34, 35]. In contrast to conventional fixed-position antennas (FPAs), also referred to as traditional antenna system (TAS), FAS is a software-defined architecture that can employ fluidic, conductive, dielectric, or other metamaterial-based media to enable real-time adjustment of the antenna's location and geometry within a specified spatial region. This huge flexibility of FAS allows the receiver to choose the optimal antenna position for the best reception of the signal.

With this new idea of a disruptive antenna system, a natural application is to use FAS to improve multi-user communication systems. Therefore, along with the proposition of FAS came the idea of a new multiple access technology using FAS which was termed fluid antenna multiple access (FAMA) [36]. Multiple access is achieved by receivers equipped with FAS, which choose the optimal antenna position to avoid interference.

We now direct our attention to the underlying motivation for this research. As the reception positions in a fluid antenna (FA) are close to each other, they are inherently correlated. The correlation models originally used in the analysis of [37, 38, 39] are based on restricted forms of the correlation matrix [40, 41] for easy mathematical tractability. However, they do not capture well the physical behavior of FAS. New correlated channel models are also presented in [42] and [43], that have been proven to be prohibitively complex, resulting in intractable analysis in FAS and FAMA [42, 43, 44], due to multi-folded integrals involved. The spatial block-correlation model recently proposed in [45], accurately characterizes the correlation, as predicted by classical realistic models such as Jakes', while maintaining analytical tractability and simplicity of the constant correlation model presented in [41]. This thesis employs two correlation models: the constant correlation model [41] and the spatial block-correlation model [45].

Effective design and implementation of future FAMA systems require a thorough evaluation of the impact of the channel on network performance. The present thesis aims to advance the understanding of FAMA networks operating under Nakagami-m fading channels. The Nakagami-m distribution, originally introduced due to its strong alignment with empirical data [46], offers higher DoFs than the Rayleigh distribution. Despite being a well-known and established model in the wireless communication field, the Nakagami-m distribution has been continuously used to evaluate the performance in different applications such as intelligent reflecting surface (IRS) [47], also named reconfigurable intelligent surface (RIS), NOMA [48], free-space optical-radio frequency (FSO-RF) [49] system, cognitive radio systems [50], mmWave, unmanned aerial vehicle (UAV) communication [51], integrated sensing and communication (ISAC) [52], and others, to cite a few recent results. This thesis contributes to the body of research concerning Nakagami-m channels under FAMA systems. More specifically, this study seeks to deepen the understanding of FAMA networks under Nakagami-m fading by deducing novel expressions for critical performance metrics, such as outage probability (OP) and multiplexing gain.

In summary, this thesis explores the knowledge gap of FAMA networks operating over Nakagami-m fading channels, employing mathematically tractable correlation models. The analysis begins with the simplified constant correlation model and subsequently extends to a spatial block-correlation model, which more accurately captures practical propagation conditions.

1.2 OBJECTIVES

This thesis is based on work published in leading journals and conferences, and submitted articles, which contain contributions to the state-of-the-art, as follows:

- Chapter 3 presents: (i) a study about slow FAMA (s-FAMA) under Nakagami-m fading channels, in which new expressions are derived for the OP, based on signal-to-interference ratio (SIR) and signal-to-interference plus noise ratio (SINR); (ii) a simple upper bound for SIR-based OP under Nakagami-m fading channels; (iii) bounds for the multiplexing gain under Nakagami-m fading channels; (iv) a closed-form and approximate OP expressions under Nakagami-m in noisy channels using Gauss-Laguerre quadrature.

- Chapter 4 presents: (i) novel expressions for OP-based on SIR for s-FAMA under the effect of Nakagami-m fading, considering the spatial block-correlation model, which is more realistic, compared to constant correlation model used in Chapter 3; (ii) approximate expression for the SIR-based OP for s-FAMA under Nakagami-m channels with spatial block-correlation; (iii) an upper bound for the SIR-based OP; (iv) interesting similarities between fast FAMA (f-FAMA) and s-FAMA, where mathematical relationships are presented (these relationships allow expressions of one type of FAMA to be obtained from the other); (v) analysis of opportunistic FAMA (O-FAMA) for fast and slow modes, under the perspective of Nakagami-m channels and spatial block-correlation, where results are provided for the multiplexing gain.

- Chapter 5 presents: (i) a study on FAMA networks with maximum ratio transmission (MRT) precoding in BSs, considering small-scale fading with Nakagami-m distribution and large-scale fading, in which new and approximate expressions are derived for SIR-based OP concerning fast and slow FAMA; (ii) reduced expressions for OP that help gain insights about the system behavior; (iii) comparative analysis for f-FAMA and s-FAMA, where an unusual behavior of superior performance of s-FAMA was reveled; (iv) the utilization of FAS to decrease the number of antennas required at the BS, thereby lowering the overall network complexity.

1.3 PUBLICATIONS AND SOFTWARE DEVELOPED IN THE FRAMEWORK OF THE PRESENT THESIS

1. P. R. de Moura, H. S. Silva, U. S. Dias, H. T. P. Silva, "Slow, Fast and Opportunistic FAMA: A Spatial Block-Correlation Analysis under Nakagami-m Fading Channels", *IEEE Wireless Communications Letters*, vol. 15, pp. 1787–1791, Jan. 2026

2. P. R. de Moura, H. S. Silva, U. S. Dias, H. T. P. Silva, O. S. Badarneh, and R. A. A. de Souza, "Slow FAMA under Nakagami-m Fading Channels," *Digital Signal Processing*, vol. 163, p. 105208, Aug. 2025.

3. P. R. de Moura, A. C. Moraes, H. S. Silva, U. S. Dias, F. A. P. de Figueiredo, and R. A. A. de Souza, "Standardization Steps for FAS in 6G Networks," in *Proceedings of the 17th International Conference on Signal Processing and Communication System (ICSPCS)*, Surfers Paradise, Australia, Dec. 2024, pp. 1–6.

4. P. R. de Moura, H. S. Silva, U. S. Dias, H. T. P. Silva, and R. A. A. de Souza, "Certificate of Registration of Computer Program," *Title: Performance Analysis of Slow Fluid Antenna Multiple Access Systems under Nakagami-m Fading Channels*, Language: MATLAB, Field of Application: TC0-2, Type of Program: SM-01, Process No.: BR512025004101-2, National Institute of Industrial Property (INPI), Brazil, Date of issuance: September 2, 2025.

1.4 ADDITIONAL ACHIEVEMENT

Recognition as a finalist in the Four Minute Thesis Competition, organized by the IEEE Communications Society (ComSoc) and held during the IEEE International Conference on Communications (ICC) on 25 May 2026 in Glasgow, Scotland, United Kingdom.

1.5 DOCUMENT ORGANIZATION

This thesis is organized in six chapters, including this, described as follows. This chapter presents the context, motivation for the study, the research question, and the structure of the thesis. In Chapter 2, the foundational concept of FAS is elucidated along with a comprehensive review of the existing literature. Chapter 3 examines the performance of s-FAMA under Nakagami-m channels. Chapter 4 provides novel and more precise expressions for OP based on SIR for s-FAMA, f-FAMA and O-FAMA under the effect of Nakagami-m fading, considering the spatial block-correlation model. Chapter 5 presents a study on FAMA networks with MRT precoding in BSs, considering small-scale fading with Nakagami-m distribution and large-scale fading concerning s-FAMA and f-FAMA. Chapter 6 presents the conclusions of this study and proposes future research directions.

CHAPTER 2

FLUID ANTENNA SYSTEM: FROM THE CONCEPT TO STANDARDIZATION

This chapter presents a comprehensive survey of FAS and FAMA. Given that this is a relatively recent research area, introduced only a few years ago, the chapter provides a structured overview that progresses from fundamental concepts to advanced challenges. In doing so, it establishes the conceptual foundations for the core contributions of this thesis, which are developed in the subsequent chapters.

2.1 FAS OPERATING PRINCIPLE

Multi-antenna technologies have advanced over the past decades, but the fundamental idea is unchanged: to harness the diversity offered by multiple signal copies received at different, independent locations, thereby mitigating fading and reducing the randomness of wireless channels.

In multiple-input multiple-output (MIMO) systems, multiple antennas are placed in sufficiently separated fixed positions at both the transmitter and the receiver. Independent fading channels between different pairs of antennas contribute to stabilizing the wireless link, leading to the well-known phenomenon of channel hardening.

Fluid antennas (FAs) represent a disruptive paradigm that promotes software-controlled antennas whose positions and shapes can be reconfigured flexibly. This concept frees antennas from fixed and rigid implementations, enabling them to leverage the vast diversity available within the limited physical space of a mobile device and opening up new, previously unimaginable possibilities.

The concept of FAS was originally introduced by the works of Wong *et al.* [34, 53, 36], with its core concept drawing in part inspiration from Bruce Lee's philosophy of adaptability and fluidity [54]:

> *"Be like water making its way through cracks. Do not be assertive, but adjust to the object, and you shall find a way round or through it. If nothing within you stays rigid, outward things will disclose themselves. Empty your mind, be formless. Shapeless, like water. If you put water into a cup, it becomes the cup. You put water into a bottle and it becomes the bottle. You put it in a teapot it becomes the teapot. Now, water can flow or it can crash. Be water, my friend."*

FAS exploits microscopic multipath fading by densely deploying a large number of closely spaced ports that finely sample rapid spatial variations of the wireless channel. By continuously selecting the port exhibiting the highest instantaneous signal-to-noise ratio (SNR), the FAS effectively implements selection combining (SC), yet in a manner that is fundamentally distinct from conventional diversity architectures, which typically rely on widely separated antennas with low mutual correlation. The strong spatial correlation observed among FAS ports reflects deliberate spatial oversampling beyond the spatial Nyquist rate, thereby enabling the system to accurately track ("surf") the spatial fading profile and pinpoint its local maxima.

The term FAS constitutes a concept that encompasses any fluidic, conductive, or dielectric structure controlled by software that is capable of dynamically modifying its geometry and/or spatial position to reconfigure its radiation behavior. This reconfigurability can target a range of antenna characteristics, including but not limited to radiation pattern, gain, and operating frequency, and can be tailored to meet diverse communication requirements. The descriptor "fluid" is used in a predominantly metaphorical sense, drawing inspiration from the adaptability emphasized in Bruce Lee's philosophy of "Be water" [54]. It is intended to highlight the intrinsic flexibility, configurability and lack of a fixed form of the system, rather than strictly denote a physically liquid state [55].

Figure 2.1 shows the received signal in a rich multipath fading environment along the linear distance. It is clear that there is a great variation in the channel magnitude. This variation can be exploited by the FAS to identify the optimal location where the magnitude of the reception field is maximized.

Figure 2.2 shows a mobile network with an UE equipped with an FAS, which is composed of N different fixed locations, which are called "ports" and are considered an ideal point antenna for the best reception of the signal, distributed over a linear dimension $W\lambda$, in which λ is the

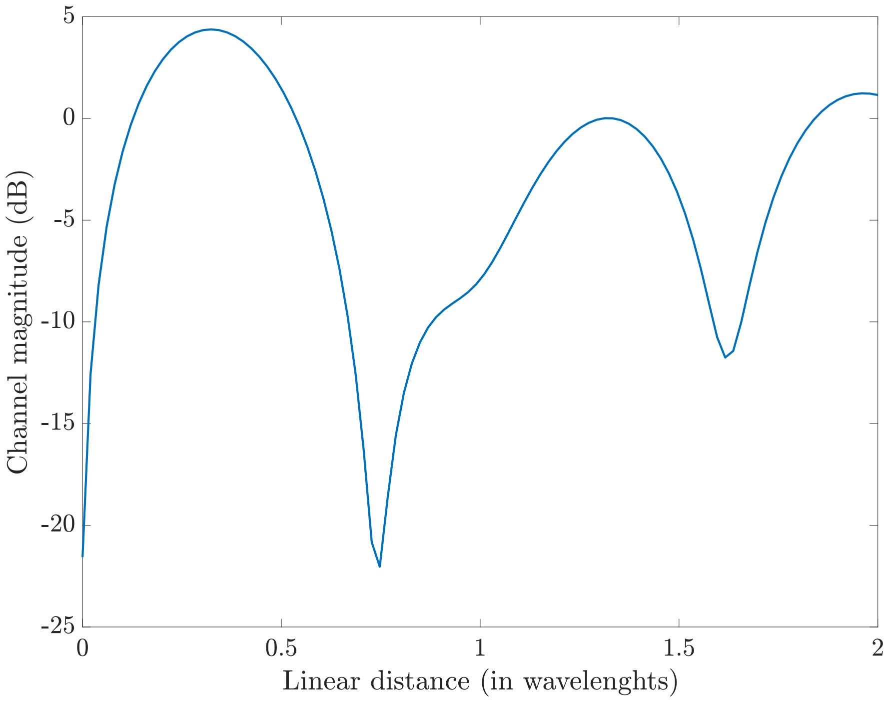

Figure 2.1. Magnitude as function of distance of typical received signal in a rich multipath fading environment.

wavelength and W is the normalized antenna size [36]. The red dot is an idealized fluid that can freely move along the length of the antenna.

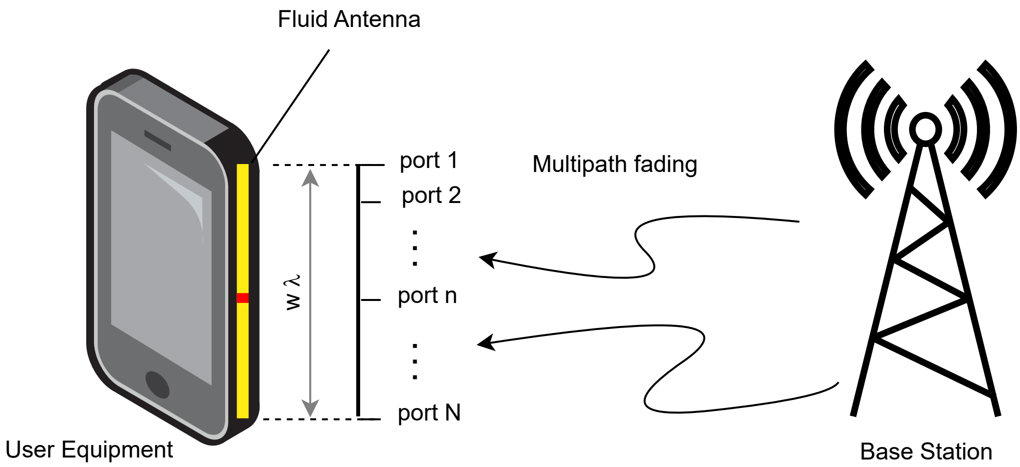

Figure 2.2. Mobile network with an UE equipped with an FAS.

Figure 2.3 compares the OP for FAS-equipped receivers with different normalized sizes W versus number of ports, and for maximum ratio combining (MRC) receivers equipped with L-antennas. It is a Rayleigh fading environment and the signal-to-noise ratio (SNR) considered as a threshold is equal to the average received SNR. The expression of OP for FAS is obtained from [41, Eq. (16)], and for the MRC receiver in [56, Eq. (6.25)]. The high diversity of FAS can exceed or surpass the MRC receiver, even in a small physical aperture (e.g., $W < \lambda/2$).

This result challenges the classical premise that large inter-antenna spacing and weakly correlated channels are prerequisites for achieving substantial diversity gains, and instead demonstrates that pronounced diversity can be harnessed from a highly constrained spatial region through high-resolution spatial sampling and adaptive port selection.

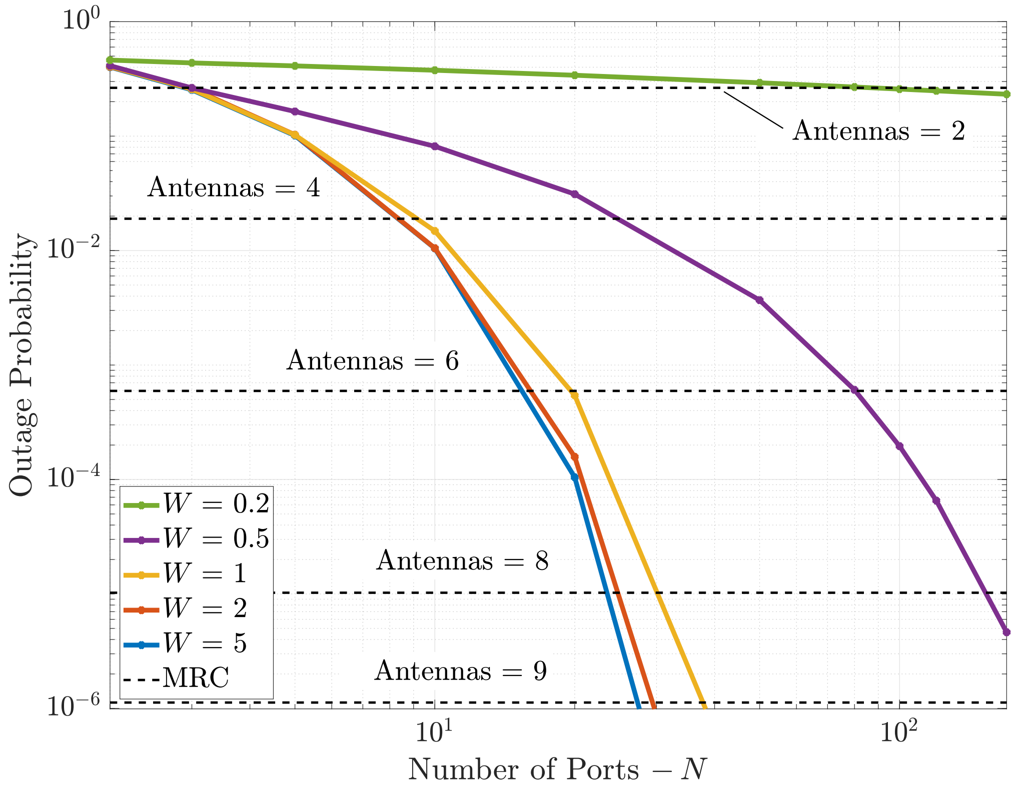

Figure 2.3. Outage probability for receivers equipped with FAS with different normalized sizes W versus number ports, and for receivers equipped with MRC L-antennas.

A significant development in this area is the emerging conceptual and practical convergence between the FAS paradigm and the notion of movable antennas (MAs) [57, 58, 59]. Both frameworks are centered on the adaptive selection and/or adjustment of antenna positions in space in order to exploit channel fluctuations for performance enhancement. Consequently, in a substantial portion of the recent literature that concentrates on the optimization of antenna placement, the terms FAS and MA are often employed in an almost interchangeable manner.

The term FAS is adopted in academic research as a hardware-agnostic description of wireless systems by modeling each "port" as an abstract and selectable spatial sampling point. This abstraction yields a unified analytical framework that is independent of the specific physical implementation (mechanical, electronic, fluidic, or metamaterial), thus supporting a systematic study of fundamental limits, resource allocation, and signal processing across diverse architectures and technologies.

2.2 HARDWARE DESIGN

The hardware design of FAS is in early stages; therefore, practical aspects, such as integration with RF circuits, compatibility with existing devices, cost, or scalability of the prototypes, are not considered at this time. However, the choice of technology is crucial to the feasibility of future applications, especially due to the reconfiguration time of the antenna ports.

This section briefly describes the current state-of-the-art designs for FAs: liquid-metal fluid antennas (LMFAs), mechanically movable antennas (MAs), pixel-based fluid antennas (PBFAs) and meta-fluid antennas (MFAs) [60].

2.2.1 Liquid-Metal Fluid Antenna (LMFA)

In LMFA the radiating element is a liquid-metal that moves in a container. The paper [61] describes two prototypes that were simulated, fabricated, and measured across the 24-30 GHz band, one with single-channel and the other with double-channel. Figures 2.4 and 2.5, from [61], present these FA prototypes featuring dynamically position-flexible radiators, which use the liquid-metal Galinstan as fluid radiator.

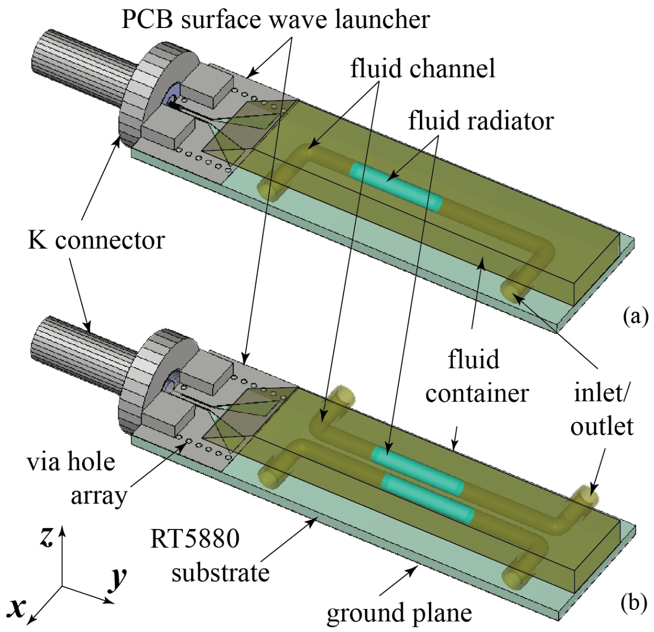

Figure 2.4. The top view of two LMFAs: (a) single-channel LMFA and (b) double-channel LMFA. **Source:** [61] ©2026 IEEE.

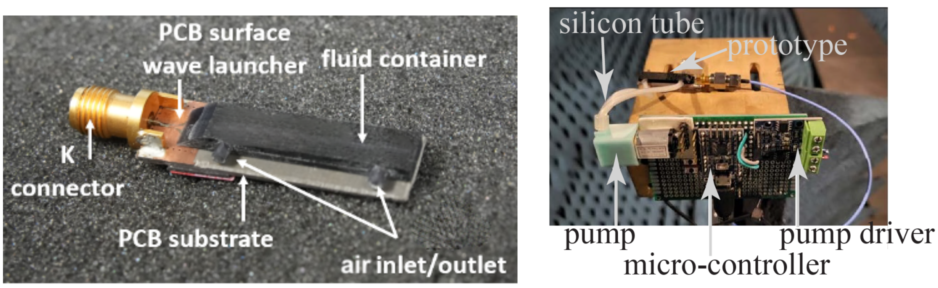

(a) (b)

Figure 2.5. The fabricated prototype of a single-channel LMFA: (a) top view of LMFA and (b) LMFA setup on a turntable in an anechoic chamber for radiation pattern measurement.
Source: [61] ©2026 IEEE.

The system employed surface-wave launchers and a fluid-control system with a pump driver. The principle of operation is to inject the signal through the K connector into the printed circuit board (PCB) launcher, and a surface wave is excited and guided along the $+y$-direction on the grounded substrate. When the wave reaches the liquid-metal, part of the energy is re-radiated into free space. Depending on the position of the liquid-metal, the radiation pattern changes.

In [62], a pump-free prototype with a continuous electro-wetting technique was shown, where the movement of the liquid metal radiating element is controlled by applying a voltage to the two electrodes in the electrolyte, thus changing the surface tension of the liquid metal to enable movement.

If a precise control system is available, the radiators in LMFA can basically be traversed continuously inside the fluid channels, giving a huge number of radiating positions. However, the drawback is the high transition time between ports.

2.2.2 Movable Antenna (MA)

In MAs the antennas are mechanically moved to the desired position. The MA prototype described in [63] functionally decouples the communication subsystem from the mechanical positioning subsystem. The system operates at 3.5 or 27.5 GHz. Specifically, a receiver module comprising a conventional rigid four-element antenna array and associated RF chains is operated independently of an antenna-positioning module, which employs stepper and servo motors mounted on a mechanical slide to adjust the antenna position and orientation within a Cartesian coordinate space. Both subsystems are orchestrated by a host computer responsible for signal processing as well as low-level and high-level motor control.

Although MAs enable flexible positioning, there are substantial practical limitations: their bulky, high-mass structures constrain deployment options, slow mechanical actuation impairs dynamic responsiveness, and progressive component degradation compromises long-term operational reliability.

2.2.3 Pixel-Based Fluid Antenna (PBFA)

The speed of port switching can be improved with pixels that emulate a fluid or mechanical movement and is the principle of pixel based FA (or pixel reconfigurable antenna). Some prototypes of this concept have been presented in recent publications [64, 65, 66].

Figure 2.6, from [65], presents a PBFA where the pixels made of metal patches are turned on and off by fast RF switches, such as positive-intrinsic-negative (PIN) diodes, to create the desired radiation pattern. The switching time can be as low as tens of microseconds.

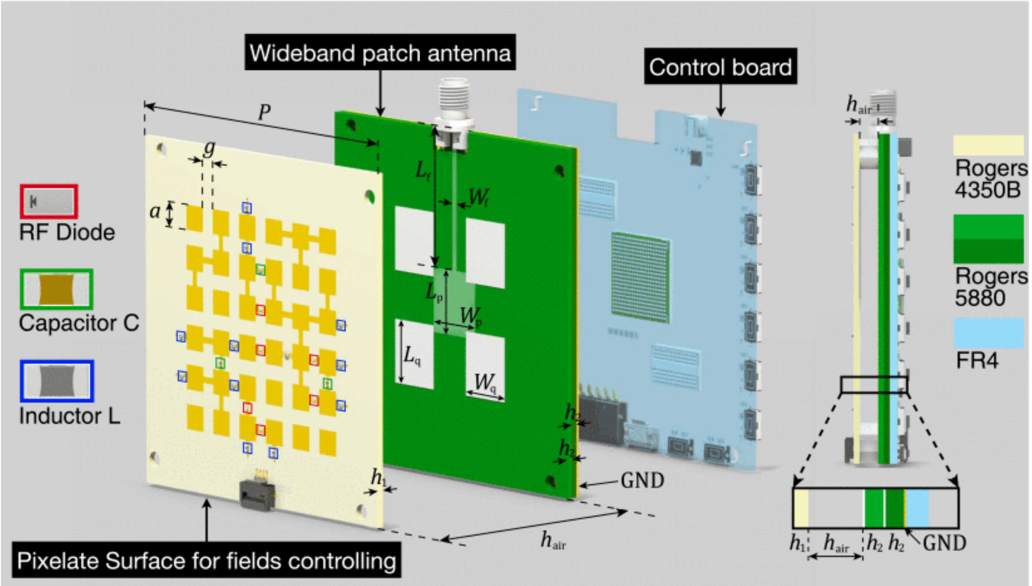

Figure 2.6. Configuration of a PBFA, showing the driven patch, parasitic elements, and pixel-switching structure. Some dimensions of the antenna are: $P = 70$ mm, $a = 5$ mm, $g = 3$ mm.
Source: [65] ©2026 IEEE.

2.2.4 Meta-Fluid Antenna (MFA)

The switching time can be reduced to less than a microsecond with the use of an MFA with the architecture proposed in [67] and [68], where a metasurface is composed of an array of resonant elements that allows fine control over the radiation pattern and fast switching speeds.

Figure 2.7, from [67], presents the MFA architecture which uses PIN diodes to control the state of each meta-atom for activation and deactivation, and adopts millimeter-wave substrate-integrated waveguides (SIWs) to gather the energy from the metasurface for radiation.

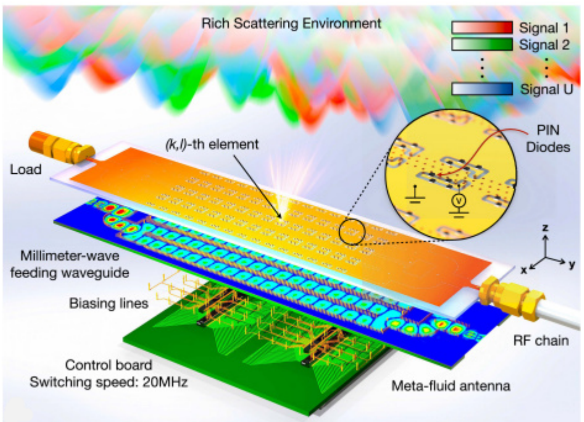

Figure 2.7. Illustration of the MFA architecture. The control of the meta-atom or radiating elements is managed by an FPGA underneath.
Source: [67].

A meta-atom is made up of two elements, referred to as the slot " + " and slot " − ". The elements can be dynamically switched between radiating and non-radiating states, as illustrated in Figure 2.8. By utilizing a field-programmable gate array (FPGA) controller, a single element with four PIN diodes can be selectively activated to radiate energy from the waveguide to air, while the remaining elements remain in a non-radiating state. Considering that the lattice size of the meta-atom is much smaller than the wavelength, the elements can be considered as sampling points (or FA ports).

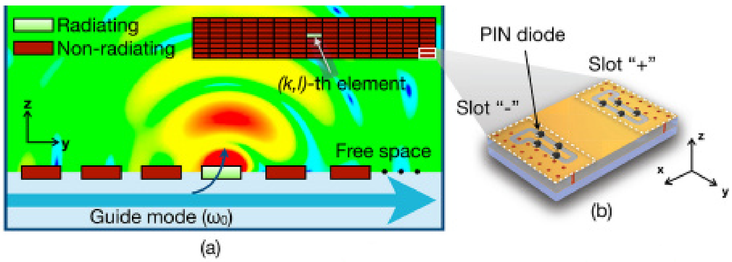

Figure 2.8. Schematic representation of an MFA: (a) shows the MFA architecture with radiating elements and the radiating pattern in the yz-plane if a given element is activated and (b) shows the basic structure of a meta-atom which consists of two elements, called slots.
Source: [67].

2.3 APPLICATION SCENARIOS FOR FAS

This section outlines possible key application scenarios for FAS described in the literature, following the categories considered in [69]: single-user FAS networks, multi-user FAS networks, and heterogeneous networks. Single-user FAS networks refer to BS serving a single user within a macro-cell. For this category, the applications: basic FAS, RIS-aided FAS and RIS-aided IM will be presented. Multi-user FAS networks refer to BS serving multiple users within a macro-cell. For this category, the applications: multi-user MIMO-FAS, FAMA and FAS-aided ISAC will be presented. For heterogeneous networks, applications of content-centric FAS and FAS-assisted cell-free networks will be presented.

The objective here is to present a glimpse of the great amount of research that has been done on FAS with a focus on applications. Although this is a relatively emerging research topic, a recent tutorial has already cataloged more than 300 articles in the field [70].

2.3.1 Basic FAS

Fluid antennas can be deployed at the BS, at the UE, or simultaneously at both ends of the link. Depending on the number of activated ports, the resulting architecture is referred to as single-input single-output FAS (SISO-FAS) or multiple-input multiple-output FAS (MIMO-FAS). In the SISO-FAS configuration, a single port is active at both the transmitter and the receiver, whereas in the MIMO-FAS configuration, multiple ports are activated concurrently.

In [70], additional prefixes (Rx, Tx and Dual) were introduced in the nomenclature to describe configurations that combine FAS and TAS. The prefix denotes the position of FAS in the configuration. For example, an Rx-MIMO-FAS architecture denotes a transmitter equipped with a multiple TAS and a receiver equipped with multiple activated ports FAS.

The fluid antenna structure can be realized in a linear configuration, referred to as a one-dimensional linear FAS (1D-FAS), or in a planar configuration, referred to as a two-dimensional planar FAS (2D-FAS).

The fluid antenna has gained considerable attention after the recent works of Wong *et al.* [34, 53, 36], who coined the concept of a FAS. Performance limits were introduced in [53], in which expressions were presented for important statistics and metrics, such as ergodic capacity and level crossing rate, under Rayleigh fading channels. In [71], a study on FAS is made over α-μ channels to evaluate the impact of the non-linearity of the propagation medium. In an Rx-SISO-FAS configuration, for 1D-FAS, the seminal work [36] demonstrated that OP of FAS can outperform TAS in a MRC configuration if the number of ports is large, and later [35] extended the results for 2D-FAS.

The performance of Dual-MIMO-FAS were also compared with traditional MIMO. In [72] the diversity-multiplexing tradeoff was studied and one conclusion is that the diversity gain for Dual-MIMO-FAS in a 2D-FAS setup is much superior to traditional MIMO. For example, for planar transmitter and receiver antennas with dimensions of 1×1 wavelength, the maximum diversity gain of traditional MIMO is $9 \times 9 = 81$, while it is approximately 529 for Dual-MIMO-FAS. This superior performance is due to the fact that the MIMO-FAS outage only occurs when all ports experience a deep fade. The higher diversity suggests a higher rate.

2.3.2 RIS-Aided FAS

Reconfigurable intelligent surfaces (RISs) improve base station coverage cost-effectively by adjusting element phase shifts to steer signals. When integrated with FAS, they yield synergistic gains. In the RIS-assisted FAS network considered, a base station with TAS transmits to an UE, equipped with FAS, through a RIS, because the direct BS–UE link is blocked. Synergy between RIS and FAS was initially reported in [73], where a randomized phase shift of RIS was proposed to reduce the complexity of acquiring and coordinating CSI between RIS and UE. In [74], RISs are used as distributed artificial scattering surfaces to enable receiver users equipped with FAS. Additionally, precoding at BS appeared ineffective if a direct link does not exist.

In the works [75] and [76], instead of using random phase shifts for RIS, the overall channel was maximized. This was made by choosing the phase of the RIS elements as the negative of the sum of the phases of the channel coefficients from BS to RIS and from RIS to UE.

In [77] a performance analysis framework was presented for two schemes: CSI-based and CSI-free. More recently, the work [78] extended the paradigm of RIS incorporating position reconfigurable elements, in what was called fluid reconfigurable intelligent surface (FRIS).

2.3.3 FAS-Aided IM

Index modulation (IM) constitutes a transmission paradigm in which information is encoded by selectively activating distinct dimensions of available communication resources. These resources may include, for example, different carrier frequencies, time slots, or antenna ports in FAS, which is called FAS-aided IM. In this scenario, it comprises a transmitter with FAS and a receiver with conventional FPAs.

The modulation is performed over the fluid antenna ports by selecting specific ports for transmitting modulated symbols. In each transmission interval, the incoming block of bits is split into two segments: one is mapped to a constellation symbol, and the other determines the active port index set. The rich port-selection combinations offered by FAS thus increase the spectral efficiency of the FAS-aided IM system [79]. It should be noted that the analysis of IM has already been extended to MIMO [80].

2.3.4 Multi-User MIMO-FAS

Within this framework, both the BS and multiple UEs can be equipped with FAS. This concept can be further extended to general cellular network architectures, in which the predominant challenge lies in formulating and solving high-dimensional optimization problems. To effectively address these problems, advanced mathematical optimization methodologies and machine learning (ML) techniques are typically used [81].

A comparison of the performance achieved by multiuser MIMO-FAS and traditional MIMO in rich scattering environments was presented in [70]. Due to the capability to precisely adjust the locations of the radiating elements within a fixed region, the average channel-to-interference ratio of FAS can be markedly improved relative to TAS, assuming the same number of active ports or antennas.

In [82], it was demonstrated that FAS-MIMO configurations employing a limited number of active radiating ports can achieve a degree of channel hardening comparable to that obtained with TAS-MIMO systems utilizing a substantially larger number of transmit antennas.

2.3.5 FAMA

As explained in Chapter 1, the state-of-the-art multiple access technology, such as massive MIMO, NOMA and RSMA require enormous efforts at the BS to acquire full CSI and optimize its transmission. The latter two also need to perform SIC at the receiver side.

FAMA provides a fundamentally different view on mitigating inter-user interference, in which multipath fading is actually treated as a beneficial effect [37]. It allows each UE to use its own FAS to choose the best spatial ports. Since interference mitigation and channel optimization are handled directly at the UE side, the BS does not require CSI. Moreover, the distributed BS antennas guarantee that transmissions to different UEs are effectively independent. This decentralized approach eliminates CSI feedback procedures, reduces latency and signaling overhead, and improves scalability for scenarios with massive connectivity.

Additional details on FAMA technology are presented in Section 2.6.

2.3.6 FAS-Aided ISAC

ISAC can be enhanced with the help of FAS by flexibly trading off sensing and communication. In [83] an algorithm was developed based on sparse optimization, convex approximation, and a penalty approach. In multicast ISAC, the BS transmits a common signal to the users and exploits the echoes for target and sensing. That reduced the transmit power by one third with the same sensing and communication performance. In [84], deep reinforcement learning was adopted for joint optimization of antenna port selection and the precoder to maximize the sum rate of the system with a sensing constraint. The simulation results showed that the FAS can deliver impressive ISAC performance with partial CSI.

2.3.7 Content-Centric FAS

Using 5G's predictive capabilities, along with context awareness and social network information, allows mobile operators to proactively cache frequently requested content at base stations and user devices. This predictive edge caching can significantly reduce peak data traffic and help operators manage growing data demands [85]. In content-centric networks (CCNs), frequently requested content is pre-stored at small-cell base stations (SBSs) and edge nodes. In prospective 6G systems, a central approach is to densely integrate SBSs into current macrocells and proactively cache popular content at these SBSs during off-peak periods. Owing to its capability to dynamically adapt to time-varying channel conditions, FAS constitutes a highly promising enabling technology for heterogeneous networks. In [86], the authors demonstrated that employing an FAS with only a single active port at the UEs can enhance the overall performance of CCN-enabled heterogeneous networks compared with conventional UEs equipped with fixed antennas.

2.3.8 FAS-Assisted Cell-Free Networks

In cell-free networks, there are a very large number of distributed access points (APs). An FAS-assisted cell-free network synergistically combines the distributed processing capabilities and coverage advantages of cell-free architectures with the spatial adaptability offered by FAS.

When FASs are deployed in APs, they can dynamically adjust their effective position, orientation, or radiation pattern to exploit spatial diversity, thus enhancing the average achievable sum-rate of users, as demonstrated in [87] for the particular case of movable antennas.

In contrast, the FAS at each UE can adaptively select the ports associated with the most favorable AP clusters or propagation paths, thus suppressing interference and improving uplink and downlink reliability. In a cell-free network, all APs cooperate to serve each user. However, in practice, as noted in [88], coordination complexity limits joint beamforming to only a small set of APs per user. In that model, a BS performing MRT effectively represents a small cluster of coordinated APs. In particular, a network in which every UE uses FAS to mitigate interference and is associated with its closest neighboring BS (or cluster of APs), equipped with fixed-position antennas (FPAs), which employ MRT precoding to form beams toward their respective UEs, is termed a cell-free FAMA, and it was examined in [88] for Rayleigh fading. Cell-free FAMA reduces the burden of BSs in terms of both antenna costs and CSI estimation overhead, thus improving the scalability of the network.

A recent tutorial [89] highlights cell-free systems empowered by FAS as a highly promising approach for future real-world implementation. To contribute to this research direction, Chapter 5 of this thesis investigates cell-free FAMA networks under Nakagami-m fading channels, a widely recognized fading distribution, and a suitable model for assessing the performance of existing and next-generation systems, offering greater flexibility than Rayleigh.

2.4 CHANNEL MODELS FOR FAS

This section introduces several channel models employed in the analysis of FAS, with the aim of providing a deeper understanding of the FAS applications discussed in Section 2.3. Given that FAS exhibits a strong inter-port correlation, the communication channel plays a critical role in accurately evaluating its performance.

The channel models used in this thesis are suitable for a rich scattering scenario, for a finite scattering scenario other models should be considered.

2.4.1 Simplified Model

For an Rx-SISO-FAS configuration, as shown in Figure 2.2, the signal received by the UE, in downlink, at the n-th port of the 1D-FA, with N ports uniformly spaced along a liner dimension $W\lambda$, in which W is the normalized length of the fluid antenna and λ is the carrier wavelength, is given by

$$r_n = h_n s + \eta_n, \tag{2.1}$$

where s denotes the transmitted symbol, h_n represents the complex channel coefficient at the n-th port and $\eta_n \sim \mathcal{CN}(0, \sigma_\eta^2)$ is the complex additive white Gaussian noise (AWGN) with zero mean and variance σ_η^2. The average power of the transmitted symbol is $\sigma_s^2 = \mathbb{E}[|s|^2]$, where $\mathbb{E}[\cdot]$ denotes the expectation operator. In work [36], h_n is modeled as $\mathcal{CN}(0, \sigma^2)$, which implies that $|h_n|$ is Rayleigh distributed. In the remaining chapters of this thesis, $|h_n|$ is modeled by a Nakagami-m distribution.

To achieve optimal performance, FAS selects the port that maximizes SNR, which is given by

$$\mathrm{SNR} = \max_n \frac{\sigma_s^2 |h_n|^2}{\sigma_\eta^2}, \tag{2.2}$$

or, equivalently, the port associated with the channel exhibiting the highest strength is activated, i.e.,

$$|h_{\mathrm{FAS}}| = \max_n \{|h_n|\}. \tag{2.3}$$

Therefore, the OP is given by

$$P_{\mathrm{out}} = \mathrm{Prob}\left(\frac{\sigma_s^2}{\sigma_\eta^2} |h_{\mathrm{FAS}}|^2 < \gamma\right), \tag{2.4}$$

where γ is a given SNR threshold. And the rate is given by

$$R = \log\left(1 + \frac{\sigma_s^2}{\sigma_\eta^2} |h_{\mathrm{FAS}}|^2\right). \tag{2.5}$$

Up to this point, FAS appears to be closely related to the conventional SC receiver. Nevertheless, maximization of channel response introduces a substantial distinction, particularly because channels exhibit statistical correlation, as detailed below.

In previous works [36] and [37], the channel at port 1, considered a reference port, is modeled as $h_1 = \sigma\, x_1 + j\sigma y_1$, and the remaining channels are modeled as

$$h_n = \sigma\left(\sqrt{1-\mu_n^2}\; x_n + \mu_n\; x_0\right) + j\sigma\left(\sqrt{1-\mu_n^2}\; y_n + \mu_n\; y_0\right), \qquad \text{for } n = 2,\ldots,N, \tag{2.6}$$

where $x_0, x_1, \ldots, x_N$ and $y_0, y_1, \ldots, y_N$ are independent and identically distributed (i.i.d.) real Gaussian random variables (RVs) with zero mean and variance 1/2, that is, $\mathcal{N}(0, \frac{1}{2})$. Based on the spatial correlation between ports 1 and n, μ_n was chosen as [36, Eq. (8)]

$$\mu_n = \mathrm{J}_0\left(\frac{2\pi(n-1)}{N-1}W\right), \qquad \text{for } n = 2,\ldots,N, \tag{2.7}$$

where $\mathrm{J}_0(\cdot)$ is the zero-order Bessel function of the first kind.

This model, however, has a limitation, if two ports are independent of the reference port (port 1), then they will be uncorrelated with each other, which overestimates the performance. To overcome this issue, a simple solution was proposed, as follows.

Based on Jakes' model [56], the correlation coefficient between channels in two ports n and m is given by

$$\mu_n \mu_m = \mathrm{J}_0\left(\frac{2\pi(n-m)}{N-1}W\right), \tag{2.8}$$

which results in $N(N-1)/2$ equations, but only N parameters, then no solution for $\{\mu_n\}$ is possible. Therefore, in [41] a common correlation parameter μ^2 was proposed as the absolute average of the correlation coefficients[1], i.e.

$$\mu^2 = \delta = \left| \frac{2}{N(N-1)} \sum_{n=1}^{N-1} (N-n)\, \mathrm{J}_0\left(\frac{2\pi\, n\, W}{N-1}\right) \right|. \tag{2.9}$$

However, [42] reported that the channel model in (2.6), when using the spatial correlation parameter in (2.7) does not accurately represent the spatial correlation between different ports, leading to an overly optimistic performance assessment. In [45] it was shown that even the correlation in (2.9) may still not capture a realistic correlation for a large number of ports.

2.4.2 Fully Correlated Model

To more precisely characterize the spatial correlation between distinct ports under two-dimensional isotropic scattering with an isotropic receiver port—i.e., according to Jakes' model

[1] In [36] the correlation parameter μ was used, but in this thesis the power correlation δ, and $\delta = \mu^2$.

[56]—a novel correlation model was introduced by Khamassi *et al.* [42]. In this model, the channels are modeled as a linear combination of the N i.i.d. complex Gaussian RVs.

For the channel vector $\boldsymbol{h} = [h_1, \ldots, h_N]^T$, with $h_n \sim \mathcal{CN}(0, \sigma^2)$, the covariance matrix, based on Jakes' model, is $\boldsymbol{J} = \sigma^2 \boldsymbol{\Sigma}$ and each element of the spatial correlation matrix is

$$(\boldsymbol{\Sigma})_{n,m} = \frac{1}{\sigma^2}\mathrm{Cov}\left[h_n, h_m\right] = \mathrm{J}_0\left(\frac{2\pi(n-m)}{N-1}W\right), \tag{2.10}$$

Let the eigenvalue decomposition of $\boldsymbol{\Sigma}$ be denoted by $\boldsymbol{\Sigma} = \boldsymbol{U}\boldsymbol{\Lambda}\boldsymbol{U}^H$, where $\boldsymbol{U}$ is the eigenvector matrix of $\boldsymbol{\Sigma}$, $\boldsymbol{\Lambda} = \mathrm{diag}(\rho_1, \ldots, \rho_N)$ is the diagonal matrix of its eigenvalues, ordered such that $\rho_1 \geq \cdots \geq \rho_N$ and H represents the Hermitian operator (transpose and conjugate). In [42], it was demonstrated that the channel vector $\boldsymbol{h}$ admits the representation

$$\boldsymbol{h} = \sigma \boldsymbol{U}\boldsymbol{\Lambda}^{\frac{1}{2}}\boldsymbol{g}, \tag{2.11}$$

where $\boldsymbol{g} = [g_1, \ldots, g_N]^T$ and $g_n \sim \mathcal{CN}(0, 1), \forall n$.

Alternatively, the n-th element of $\boldsymbol{h}$ can be rewritten as

$$\begin{aligned} h_n &= \sigma \sum_{m=1}^{N} \sqrt{\rho_m}\, u_{n,m}\, g_m \\ &= \sigma \sum_{m=1}^{N} \sqrt{\rho_m}\, u_{n,m}\left(a_m + j b_m\right), \end{aligned} \tag{2.12}$$

where $u_{n,m}$ is the (n,m)-th element of $\boldsymbol{U}$, and a_m, b_m are $\mathcal{N}(0, \frac{1}{2}), \forall m$.

This model provides a high degree of theoretical accuracy; however, its mathematical tractability is limited due to the presence of nested integrals in the performance analysis. Even with an approximation of the covariance matrix, complexity remains and performance has been analyzed to date for up to two users [42, 44].

2.4.3 Spatial Block-Correlation Model

To alleviate the analytical intractability associated with the fully correlated model, while still capturing the correlation effects along the FA, the spatial block-correlation model was introduced in [45] as a more mathematically manageable alternative.

This model approximates the spatial correlation matrix $\boldsymbol{\Sigma}$ in (2.10) by a block-diagonal matrix denoted by $\widehat{\boldsymbol{\Sigma}}$

$$\widehat{\boldsymbol{\Sigma}} \in \mathbb{R}^{N\times N} = \begin{pmatrix} \mathbf{A}_1 & \mathbf{0} & \cdots & \mathbf{0} \\ \mathbf{0} & \mathbf{A}_2 & \cdots & \mathbf{0} \\ \vdots & & \ddots & \vdots \\ \mathbf{0} & \mathbf{0} & \mathbf{0} & \mathbf{A}_B \end{pmatrix}, \tag{2.13}$$

where each sub-matrix $\mathbf{A}_b$ is a constant correlation matrix of size $L_b \times L_b$ and power correlation coefficient δ_b, that is,

$$\mathbf{A}_b \in \mathbb{R}^{L_b\times L_b} = \begin{pmatrix} 1 & \delta_b & \cdots & \delta_b \\ \delta_b & 1 & \cdots & \delta_b \\ \vdots & & \ddots & \vdots \\ \delta_b & \cdots & \delta_b & 1 \end{pmatrix}, \quad b = 1, \ldots, B. \tag{2.14}$$

Observe that the N ports of an FA are partitioned into B distinct blocks, where the b-th block comprises L_b ports, with $b \in \{1, \ldots, B\}$, and the total number of ports satisfies $\sum_{b=1}^{B} L_b = N$. Owing to its block-diagonal structure, the proposed approximation preserves the analytical and computational tractability characteristic of the constant correlation model [41].

The sizes L_b of the blocks and the number of blocks B are determined from the dominant eigenvalues $\{\rho_b\}$ of the reference spatial correlation matrix $\boldsymbol{\Sigma}$. For simplicity in the approximation, all blocks are assumed to have the same power correlation coefficient ($\delta_b = \delta\,\forall b$) and using the condition $\delta \to 1$, each block has a single dominant eigenvalue $\rho_b = (L_b - 1)/\delta + 1$. Therefore, the size of each block is set from the dominant eigenvalues of the true correlation matrix $\boldsymbol{\Sigma}$, that is,

$$L_b = \left\lfloor \frac{\rho_b - 1}{\delta} + 1 \right\rfloor \tag{2.15}$$

where, for a given threshold ρ_{th}, the eigenvalue ρ_b is such as $\rho_b \geq \rho_{\text{th}}$ and $\lfloor x \rfloor$ denotes the floor function, defined as the largest integer $\leq x$.

To prevent the construction of an approximation matrix with a larger number of ports than the original, the block sizes L_b are iteratively increased in accordance with the procedure described in [45, Algorithm 1].

2.4.4 Channel Model for 2D-FAS

To extend the fully correlation channel model in (2.11) from 1D-FAS to 2D-FAS, some adjustments in port indices should be made. Consider a 2D-FAS of size $W_1\lambda \times W_1\lambda$, which has a uniform grid structure with $N = N_1 \times N_2$ ports. To simplify the notation, the 2D indices of ports from left to right and from top to bottom are assigned to new port indices by

$$n = (n_2 - 1)N_1 + n_1. \tag{2.16}$$

The element $(\boldsymbol{\Sigma})_{n,m}$ describing the correlation between the ports $(n_1, n_2) \to n$ and $(m_1, m_2) \to m$. In [72] it was shown that the covariance matrix is given by $\boldsymbol{J} = \sigma^2 \boldsymbol{\Sigma} \in \mathbb{C}^{N \times N}$ and the spatial correlation elements are given by

$$(\boldsymbol{\Sigma})_{n,m} = j_0\left(2\pi\sqrt{\left(\frac{n_1 - m_1}{N_1 - 1}W_1\right)^2 + \left(\frac{n_2 - m_2}{N_2 - 1}W_2\right)^2}\right), \tag{2.17}$$

where $j_0(\cdot)$ is the spherical Bessel function of the first kind.

Following this 2D model, in [72] the SISO-FAS model was extended to MIMO-FAS where transmitter, indicated by tx and receiver, indicated by rx, use an FAS, and for easy notation $s \in \{\mathrm{tx}, \mathrm{rx}\}$. The complex channel becomes

$$\boldsymbol{H} = \boldsymbol{U}_{\mathrm{rx}}\sqrt{\boldsymbol{\Lambda}_{\mathrm{rx}}}\,\boldsymbol{G}\,\sqrt{\boldsymbol{\Lambda}_{\mathrm{tx}}^H}\,\boldsymbol{U}_{\mathrm{tx}}^H, \tag{2.18}$$

where $\boldsymbol{G} \in \mathbb{C}^{N_{\mathrm{rx}} \times N_{\mathrm{tx}}}$ with each element of the matrix is i.i.d. as $\mathcal{CN}(0{,}1)$, $\boldsymbol{U}_{\mathrm{s}}$ is an $N_{\mathrm{s}} \times N_{\mathrm{s}}$ matrix of eigenvectors of $\boldsymbol{J}_{\mathrm{s}}$ and $\boldsymbol{\Lambda}_{\mathrm{s}} = \mathrm{diag}(\rho_1^{\mathrm{s}}, \ldots, \rho_{N_s}^{\mathrm{s}})$ is an $N_{\mathrm{s}} \times N_{\mathrm{s}}$ diagonal matrix of the corresponding eigenvalues.

Denoting: the transmitting symbol vector as $\boldsymbol{s}$; the activation port matrix as $\boldsymbol{A}_s = [\boldsymbol{a}_1^s, \ldots, \boldsymbol{a}_{n_s}^s]$, where a_l^s is the N_s-dimensional standard basis vector for $l \in \{1{,}2, \ldots, n_s\}$; the beamforming matrix as $\boldsymbol{W}_s$ with the constraint $\|\boldsymbol{W}_s\|_2 = 1$; the AWGN with zero mean and identity covariance as $\boldsymbol{\eta}$, then the received signal for MIMO-FAS is written as

$$\boldsymbol{W}_{\mathrm{rx}}\boldsymbol{A}_{\mathrm{rx}}\boldsymbol{Y} = \boldsymbol{W}_{\mathrm{rx}}\boldsymbol{A}_{\mathrm{rx}}\boldsymbol{H}\boldsymbol{A}_{\mathrm{tx}}\boldsymbol{W}_{\mathrm{tx}}\,\boldsymbol{s} + \boldsymbol{W}_{\mathrm{rx}}\boldsymbol{A}_{\mathrm{rx}}\boldsymbol{\eta} \tag{2.19}$$

$$\tilde{\boldsymbol{Y}} = \tilde{\boldsymbol{H}}\,\boldsymbol{s} + \tilde{\boldsymbol{\eta}}, \tag{2.20}$$

where $\tilde{\boldsymbol{Y}} = \boldsymbol{W}_{\mathrm{rx}}\boldsymbol{A}_{\mathrm{rx}}\boldsymbol{Y}$, $\tilde{\boldsymbol{H}} = \boldsymbol{W}_{\mathrm{rx}}\boldsymbol{A}_{\mathrm{rx}}\boldsymbol{H}\boldsymbol{A}_{\mathrm{tx}}\boldsymbol{W}_{\mathrm{tx}}$ and and $\boldsymbol{\eta} = \boldsymbol{W}_{\mathrm{rx}}\boldsymbol{A}_{\mathrm{rx}}\boldsymbol{\eta}$.

Denoting the power allocation matrix as $\boldsymbol{P} = \mathbb{E}[\boldsymbol{s}\,\boldsymbol{s}^H]$ and the input covariance matrix as $\boldsymbol{K} = \boldsymbol{W}_{\mathrm{tx}}\boldsymbol{P}\boldsymbol{W}_{\mathrm{rx}}$ and defining $\bar{\boldsymbol{H}} = \boldsymbol{A}_{\mathrm{rx}}\boldsymbol{H}\boldsymbol{A}_{\mathrm{tx}}$, the MIMO-FAS rate is given by

$$R = \log\det\left(\boldsymbol{I} + \bar{\boldsymbol{H}}\boldsymbol{K}\bar{\boldsymbol{H}}^H\right), \tag{2.21}$$

where the value of trace($\boldsymbol{K}$) does not exceed the transmit SNR.

In [72] the maximization of the MIMO-FAS rate was studied through joint optimization of port selection, transmit and receive beamforming, and power allocation.

2.5 CHANNEL ESTIMATION FOR FAS

Channel estimation constitutes a fundamental component of mobile communication networks, as it provides the essential basis for advanced signal processing and resource management tasks, including beamforming, user scheduling, and interference mitigation.

In this section, the specific characteristics and challenges of channel estimation are discussed in the context of FAS, together with a concise overview of representative research contributions in this area. The aim is not to offer a complete survey, but rather to highlight the critical role and distinctive importance of channel estimation for the effective design and operation of FAS.

Traditional channel estimation schemes originally designed for TAS are inadequate for FAS, as they would incur in pilot overhead due to the possibility of positioning the radiating in all port locations. To reduce pilot overhead, suitable methods for FAS only estimate channels at a few locations and reconstruct the FAS channel over a finite space on these initial estimates, considering the spatial correlation between ports, using interpolation, statistical models, or learning-based methods. In other words, the channel is estimated by processing a sequence of pilot signals that are repeatedly transmitted at a subset of ports, thereby enabling channel estimation at those locations. Channel reconstruction refers to the procedure of inferring the complex channel coefficients at unobserved ports from the estimated coefficients at the observed ports. The techniques for CSI acquisition in FAS perform processes of estimation and reconstruction in sequence.

Reconstruction accuracy primarily depends on the number of estimated channels and the spacing between them: more estimates improve interpolation and capture fast spatial variations but increase complexity and latency, while too few reduce accuracy. Likewise, too small spacing yields redundant, highly correlated data, and too large spacing leads to uncorrelated samples and poor interpolation, so an optimal spacing is needed to maintain moderate correlation and capture spatial variations. Additional factors such as estimation errors, fading conditions, and the choice of interpolation method also affect the reconstruction performance. The study [90] revealed that half-wavelength sampling is insufficient for perfect reconstruction and oversampling is essential to improve accuracy.

After the CSI for all ports, or subset of ports, has been obtained or reconstructed, the system must decide which specific port or group of ports to activate in order to meet the target performance goal, such as maximizing SNR, enhancing reliability, or reducing interference. A natural approach is to use ML techniques to learn the correlation structure between ports. Therefore in [91], the Long Short-Term Memory (LSTM) recurrent neural network was used, thus channel gains over the ports were considered as space series and the unobserved ports were estimated for 1D-FAS. The paper also used other approaches: the "smart, predict and optimize" technique and analytical approximation. The results illustrated that with only a few ports observed, a near-optimal performance was achieved. In [92], a conditional generative adversarial network (cGAN) was employed for FAMA, yielding highly accurate results even when only a limited subset of ports was available. In [93], an online learning-based port selection framework was proposed, wherein a bandit learning algorithm dynamically learns the optimal port without relying on full instantaneous CSI.

For rich-scattering environments, in [94] and [95], the authors analyzed channel estimation methods and outage behavior in large-scale cellular networks with FAS. In their work, they introduced a skipped-enabled linear minimum mean square error (LMMSE) channel estimation scheme, termed skipped-enabled channel estimation (SeCE). This approach mitigates signaling overhead by performing CSI acquisition only for a carefully chosen subset of antenna ports, rather than for all available ports. However, this selective estimation inevitably leads to a reduction in the effectively observed SINR, thereby introducing a fundamental trade-off: while the scheme achieves substantial overhead savings, it simultaneously incurs performance loss in terms of SINR, which must be balanced according to system design requirements.

In propagation environments characterized by a finite number of scatterers, the channel exhibits sparsity; that is, it can be represented by a small set of dominant parameters associated with only a few main propagation paths. The authors of [96] exploit this sparsity within their low-sample-size sparse channel estimation and reconstruction (L3SCR) framework. Due to the presence of only a limited number of dominant paths, the channel is initially coarsely estimated at a predefined set of estimation points using orthogonal pilot signals and a least-squares estimator, thereby yielding a reduced-dimension channel matrix. Subsequently, a compressed-sensing algorithm is employed at the base station to extract the sparse channel parameters, namely the number of spatial paths, angles of arrival (AoAs), angles of departure (AoDs), and complex path gains. Based on a planar-wave geometric channel model and the recovered parameters, the full channel matrix between all ports and the base station is then reconstructed. Numerical simulations demonstrate that this method can provide accurate CSI while requiring only low hardware switching complexity and reduced pilot overhead.

In [97] was presented the Sparse Bayesian Learning (SBL), as well as an advanced variant designed to explicitly maximize the increase in mutual information between successive time slots. By exploiting this information-theoretic criterion, the enhanced SBL algorithm achieves more reliable extraction of channel state information (CSI), yielding substantially lower normalized mean squared error (MSE) than competing approaches, including orthogonal matching pursuit (OMP), maximum likelihood estimation (MLE), and the basic SBL scheme. In addition to its estimation accuracy, the improved SBL method is characterized by notably low computational complexity. This renders it particularly attractive for deployment in environments with constrained processing capabilities—such as mobile user terminals or lightweight edge devices—where stringent complexity and power limitations must be satisfied without compromising the fidelity of channel reconstruction. Consequently, the method offers a practical trade-off between performance and resource usage and stands out as a strong candidate for real-time, high-precision CSI estimation in FAS-based systems.

As explained in Section 2.3.5, FAMA is an application that does not require CSI in BS, as interference mitigation is handled in UE, however, the channel still needs to be known in UE. In practical channel acquisition procedures, the estimate CSI is generally imperfect, which leads to performance degradation. However, since this work focuses on fundamental performance limits, the subsequent chapters assume perfect CSI at the UE for the analysis of FAMA.

2.6 OVERVIEW OF FAMA

Consider the downlink scenario, as shown in Figure 2.9, where a BS with N_t FPAs transmits to U FAS-equipped UEs on the same channel and $N_t \geq U$. The FPAs are distributed sufficiently far apart to be spatially independent.

The received signal at the n-th port of the u user, with $u \in \{u = 1, 2, \dots, U\}$, is written as [38]

$$r_n^{(u)} = s_u h_n^{(u,u)} + \sum_{\substack{\tilde{u}=1 \\ \tilde{u} \neq u}}^{U} s_{\tilde{u}} h_n^{(\tilde{u},u)} + \eta_n^{(u)}, \tag{2.22}$$

in which s_u denotes the transmitted symbol to the u-th user, $h_n^{(u,u)}$ is the corresponding fading channel coefficient experienced at n-th port, $h_n^{(\tilde{u},u)}$ and $s_{\tilde{u}}$ represents, respectively, the interfering fading channel coefficient and signals, with $u \neq \tilde{u}$. The average power of the transmitted symbol is $\sigma_s^2 = \mathbb{E}[|s_u|^2]$, $\forall u$, and $\eta_n^{(u)}$ is the complex AWGN, at the n-th port for the user u, with zero mean and variance σ_η^2. As the BS antennas are distributed far apart, the channels between the users are i.i.d. RVs. Furthermore, in this work, the perfect knowledge of the CSI is assumed for the receiver ports, and the switching delay between ports is neglected.

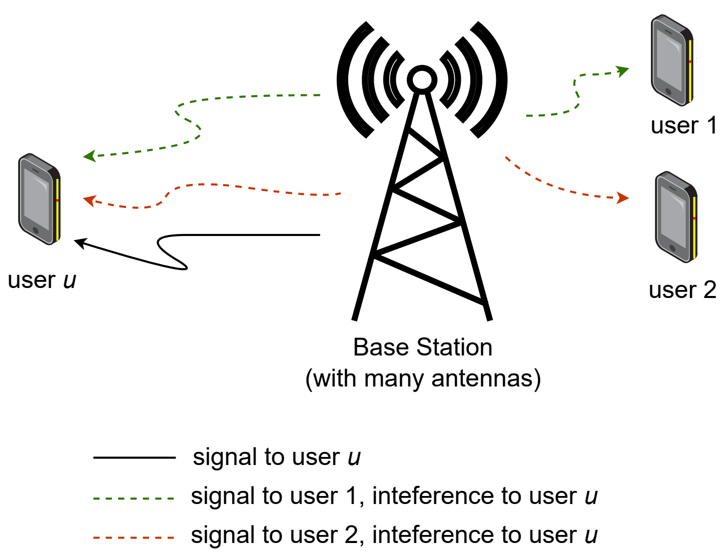

Figure 2.9. FAMA system model with U users in the downlink scenario.

2.6.1 Theoretical Interference Benchmark

With the aim of highlighting the fundamental role of fluid antennas in interference management, the study presented in [98] investigates FAMA in terms of capacity efficiency, as briefly described below.

It is well established that the Han–Kobayashi (HK) scheme constitutes the best achievable strategy currently known for the two-user Gaussian interference channel [99]. This configuration consists of two transmitter–receiver pairs. Each transmitter is intended to convey its information signal to the corresponding receiver; however, it simultaneously generates interference at the non-intended receiver. The analytical characterization and practical evaluation of the HK scheme are highly intricate [100, 101]. To address this, the authors of [98] introduced an information-theoretic benchmark termed HK-FAMA, which is constructed by combining HK rate splitting, power splitting, and joint decoding with the reconfigurability capabilities of FAS to manipulate the effective channel.

A comparison of FAMA with this benchmark demonstrated that the basic FAMA architecture, despite its relative simplicity, can achieve performance close to optimal.

2.6.2 Fast FAMA

Fast FAMA (f-FAMA) was first the version of FAMA, proposed by Wong and Tong [37], but the term "fast" was only given in [38] and [102]. The underlying rationale of f-FAMA is to perform, on a per-symbol basis, the selection of the optimal port, i.e., the port is chosen with the objective of maximizing the *instantaneous* SINR. Considering the received signal defined in (2.22), the port $n^\star$ is selected as

$$n^\star = \arg \max_{n\in\{1,\dots,N\}} \frac{|s_u h_n^{(u,u)}|^2}{|\sum_{\substack{\tilde{u}=1\\ \tilde{u}\neq u}}^{U} s_{\tilde{u}} h_n^{(\tilde{u},u)} + \eta_n^{(u)}|^2}. \tag{2.23}$$

The aggregated interference is made of the sum of user information symbols, which help to create nulls on the received signal. Therefore, data from interference users mix signals and create opportunities for a port to be in a deep fade, thus many users can be accommodated on the same time-frequency radio channel.

However, the high capacity of f-FAMA comes with drawbacks. First, each UE must access the received signals from all N FAS ports on a single RF chain, forcing the switching rate to be N times faster than the symbol rate. With symbol durations on the order of microseconds, this implies nanosecond-scale switching, which is beyond mechanical capabilities and highly challenging even for electronic switches due to settling and transient effects. A possible solution to reduce the switching rate is to use a learning-based method to extrapolate the unobserved port signals from the observed ones.

Additionally, f-FAMA also demands full CSI over all ports to estimate instantaneous SINR, which becomes prohibitive in terms of pilot overhead when N is large, potentially consuming the entire coherence block and leaving no time for data transmission. Additionally, tightly synchronizing fast port switching with symbol boundaries is a major hardware challenge, as small timing jitters can cause inter-symbol interference (ISI).

Beyond these implementation issues, there is a deeper unresolved problem: even with perfect knowledge of all received port signals, accurate instantaneous SINR estimation is not known to be achievable. Existing estimation methods, such as those in [102], suffer substantial performance loss.

Consequently, while some practical challenges may be mitigated, implementing ideal f-FAMA with acceptable pilot overhead and reliable instantaneous SINR estimation remains an open research problem, and it is currently best viewed as a theoretical performance bound rather than a deployment-ready technique.

In this thesis, the f-FAMA framework is analyzed in the context of this theoretically bound formulation and compared to s-FAMA.

2.6.3 Slow FAMA

Slow FAMA (s-FAMA) is the variant of FAMA introduced in [38] and [103], designed as an alternative to f-FAMA with enhanced practical feasibility and broader deployment potential. In s-FAMA the port of an FAS is switched only if the fading channel changes, that is, the receiver remains on the same port as long as the CSI does not change. Therefore, the port is chosen with the objective of maximizing the *average* SINR. Considering the received signal defined in (2.22), the port $n^\star$ is selected as

$$n^\star = \arg \max_{n\in\{1,\dots,N\}} \frac{\sigma_s^2 |h_n^{(u,u)}|^2}{\sigma_s^2 \sum_{\substack{\tilde{u}=1 \\ \tilde{u}\neq u}}^{U} |h_n^{(\tilde{u},u)}|^2 + \sigma_n^{(u)}}. \tag{2.24}$$

As the change of a port depends only on the channel, the port switching occurs at a rate much lower than the symbol rate. As a result, the FAS at each UE adapts solely to channel conditions while still suppressing inter-user interference, without the need for sophisticated techniques such as precoding at the BS or SIC at the receiver. However, when U is large, the average interference power at all ports can become significant. Consequently, the multiplexing gain of s-FAMA is, in principle, substantially lower than that of f-FAMA.

For a conventional N-antenna MIMO system, the power scales linearly with the number of RF chains. In contrast, a FAMA system with N ports has only one RF chain; therefore, it is suitable for massive connectivity, where battery life is a critical constraint.

The energy efficiency (EE) of FAMA is characterized by a balance between the diversity gain achieved through port selection and switching power consumption. In s-FAMA systems, increasing the transmit power of BS for a particular user increases the throughput of that user, but also leads to higher energy consumption and increased interference for the other users. This trade-off can be described by the EE, which is defined as the ratio between the system throughput and the overall power consumption. The study presented in [104] focused on optimizing the EE of s-FAMA. The results demonstrated that s-FAMA can achieve an EE performance comparable to that of MIMO space-division multiple access, while simultaneously offering substantial cost advantages due to its requirement for significantly fewer RF chains.

We now turn to the examination of studies related to OP of s-FAMA, which constitutes the main focus of this thesis. In [103] performance was analyzed, using computer simulations, in mmWave, which has a strong specular component. To synthetically generate rich scattering channels, the channel realizations were randomized through the application of a beamforming vector. In the seminal work [38], the authors derived a closed-form expression for OP in rich-scattering environments without a line-of-sight component, under the assumption of negligible noise, and also presented a compact upper-bound expression. An approximation for the expression of OP was presented more recently in [105]. In [106], noise was incorporated into the performance analysis. The authors used a Gaussian approximation to overcome the mathematical complexity of the joint PDF of the SINR at all ports; however, this assumption is valid only if the number of users is high. In this thesis, a more accurate approach is used to deal with noise in the analysis, as shown in Chapter 3.

However, the mentioned works were based on a simplified FAS channel model from [40], which does not accurately capture the spatial correlation among FAS ports. To overcome this issue, in [44] and [107] the performance of s-FAMA was analyzed using the more accurate and realistic fully correlated FAS model [42]. The authors derived approximate highly precise outage probability expressions, but restricted to two-users.

In the recent review of FAMA [108], the authors identified the development of tractable approximation methodologies for performance evaluation—under more realistic and widely applicable FAS and system models—as an open research problem. To contribute to this research direction, Chapter 4 of this thesis investigates FAMA under Nakagami-m fading channels by employing a more accurate yet analytically tractable spatial block-correlation model.

2.6.4 Opportunistic FAMA

Multiple access can be achieved by exploiting the spatial diversity inherent in deep fading events through the use of FAs. However, ensuring strong interference resilience in FAMA typically requires equipping each UE with a large number of antenna ports. To mitigate this hardware and complexity burden, a promising approach is to combine FAMA with opportunistic user scheduling, which was proposed in [39] and termed O-FAMA. By maintaining a sufficiently large pool of candidate users, the transmitter can select those users whose channel conditions are particularly well suited for FAMA operation, thereby both enhancing performance and reducing the outage probability experienced by each scheduled user.

Consider that the U users selected for communications on the same time-frequency resource unit are based on their SIRs, as in Figure 2.10.

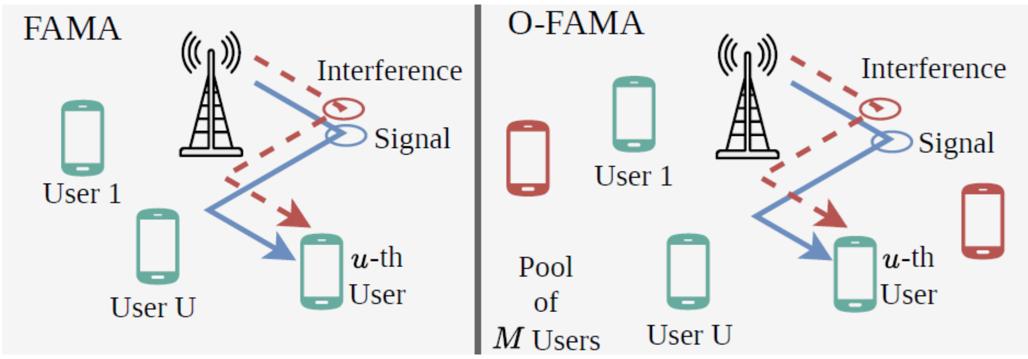

Figure 2.10. Comparison of the FAMA and O-FAMA systems in a downlink communication scenario.

In particular, it is assumed that there are $M(> U)$ UEs in the pool and their SIRs are ranked

$$\mathrm{SIR}^{(1)} \leq \mathrm{SIR}^{(2)} \leq \cdots \leq \mathrm{SIR}^{(M)}, \tag{2.25}$$

in which $\mathrm{SIR}^{(u)}$ represents the SIR of the best port of the u-th UE.

Opportunistic scheduling is motivated by maximizing network capacity by selecting the strongest $U(< M)$ UEs to communicate at any given time. In general, the SIR of an UE is influenced by the other chosen users, which theoretically implies that all $\binom{M}{U}$ possible user sets would need to be examined to accurately identify the U strongest UEs. This is, however, practically infeasible. Conveniently, in FAMA, the BS does not require any user-specific pre-processing for the selected set, so the outage probability of a given selected UE is independent of which other UEs are selected. Consequently, each UE can, based on its SIR, determine a confidence level for being among the top-U UEs in the pool. This enables the BS to iteratively activate and deactivate UEs until the strongest ones are found. The paper [109] proposed a resilient decentralized reinforcement learning scheme for O-FAMA that jointly selects robust users and their FAS ports to maximize network sum-rate.

The Chapter 4 investigates O-FAMA under Nakagami-m fading channels.

2.6.5 Other Variants of FAMA

In the literature, additional variants of FAMA have been proposed. Although these variants are not the primary focus of this thesis, it is useful to briefly acknowledge them.

Slow FAMA (s-FAMA) operates by choosing the best single port for each UE, which is only effective when every UE has at least one port with sufficiently low interference. However, this condition quickly becomes unlikely as the number of interfering sources increases, since all ports at an UE can then be heavily contaminated by interference. A natural way to address this limitation is to activate several ports at the same time and combine their received signals, thereby leveraging additional spatial diversity and potentially improving performance. This intuition underpinned the development of Compact Ultra-Massive Antenna Array (CUMA) [110, 111].

The core principle of CUMA is to activate many "good" ports at the same time and combine their received signals in the analog domain, thus leveraging the natural randomness of channel gains to mitigate interference. For this strategy to work, the desired signal components must add up constructively rather than cancel each other out during the summation. This is ensured by selecting only those ports whose channel coefficients have the same sign in their real or imaginary components.

The paper [112] proposed a coded FAMA system that integrates FAMA with coded modulation schemes and employs a soft-decision-based receiver, which outperforms the hard-decision method presented in [102]. The system used a time scale at the codeword level, making it compatible with 5G-NR (5G New Radio) physical layer designs.

The recently proposed turbo FAMA uses joint source-channel coding (JSCC), which jointly designs the transmitted signals taking into account source characteristics (for compression) and channel conditions (for error correction) [113]. On the receiver side, the system shortlists a small number of promising ports and coherently combines the signals of the selected ports using MRC, then after a diffusion denoiser and a JSCC decoder reconstruct the data symbols are reconstructed.

2.7 STANDARDIZATION STEPS FOR FAS UNDER 6G NETWORKS

An important step for a technology to succeed is its inclusion in a standard. This section encourages the academic community to work together to overcome standardization barriers and achieve the successful implementation of FAS.

2.7.1 Benefits and Challenges of FAS for 6G Networks

FAS technology has disruptive potential due to its adaptability to dynamic wireless conditions. It could address many challenges in densely populated urban areas and highly mobile environments, such as high-speed trains or autonomous vehicles. The reconfigurability of FAS enables flexible beamforming, spatial diversity, and the ability to optimize SNRs under varying propagation scenarios, potentially reducing signal interference and improving spectral efficiency. However, the complexity of implementing FAs introduces new challenges, including the need for advanced materials that can maintain antenna performance under shape-shifting conditions and integrated circuit designs that support dynamic reconfiguration. Mutual coupling is a notable challenge, especially for FAS based on pixels. The switching time or response time of the fluid antenna is critical in assessing the performance of FAS. Additionally, the safety of the fluid for users, such as in scenarios involving fluid leakage, may pose a concern regarding the liquid-base antenna hardware implementation.

2.7.2 The Role of Standardization in Accelerating FAS Deployment

Standardization plays a pivotal role in the rapid adoption and interoperability of emerging technologies, as it establishes common frameworks, protocols, and performance benchmarks that ensure compatibility across different devices and networks. In the context of FAS, standardization could streamline the integration of fluid antennas in commercial 6G devices, enabling faster deployment and reducing the risks associated with proprietary solutions that may hinder widespread adoption. Furthermore, standardized FAS solutions could support more seamless international deployments, as common guidelines would facilitate the regulatory approvals required for FAS-enabled devices in different countries. Standardization efforts could also drive innovation by encouraging industry-wide collaboration, leading to improvements in fluid antenna designs, materials, and associated algorithms.

2.7.3 Opportunities for FAS under Advanced 6G Use Cases

The unique capabilities of FAS align well with several anticipated 6G use cases, such as immersive communication, hyper-reliable and low-latency communication (HRLLC), massive communication, AI, ubiquitous connectivity, and ISAC. In immersive communication scenarios, where high data rates and large user densities are expected, FAS can dynamically adjust to optimize signal quality and maintain connectivity in high-interference environments. In HRLLC applications, where reliability and latency are critical, the ability of FAS to reconfigure quickly could help maintain robust links even in complex urban and industrial environments. Concerning ISAC, FAS can be used to jointly optimize both the ports and the precoder, thereby creating effective communication and sensing channels that allow simultaneous sensing and communication operations [84]. Additionally, in massive communication contexts, FAS could support the efficient handling of large-scale internet of things (IoT) deployments, adjusting signal reception patterns based on the density and mobility of connected devices. However, realizing these use cases with FAS will require close collaboration between industry, academia, and standards development organizations (SDOs) to refine and validate FAS technology for each application context.

2.7.4 Encouraging Collaboration

To overcome the current gap between FAS technology and its inclusion in international standards, collaborative initiatives involving academic researchers, industry stakeholders, and SDOs are essential. For instance, forming specialized working groups within organizations such as the ITU and the Third Generation Partnership Project (3GPP) could facilitate focused discussions on FAS requirements, technical challenges, and performance metrics. Workshops and joint research programs could also be platforms for exchanging insights and addressing implementation issues. By engaging in such activities, the FAS research community can help accelerate the development of standards that will make FAS a practical component of 6G networks. In turn, these standards could help de-risk FAS investments for manufacturers and network providers, enabling faster and broader deployment.

Although FAS technology is in the early stages, there is a good momentum to start discussing it in international standardization organizations. It can be treated as a separate technology or in conjunction with other antenna technologies, such as MIMO, or new materials for telecommunications, such as RIS. The academic community should actively participate in standardization study groups to achieve this goal, especially in ITU and 3GPP.

2.7.5 Model for OFDM-FAMA in 5G-NR

A more substantial advancement toward the standardization of FAS within the academic community was recently achieved through the publication of [114], which formulates a FAMA model based on 3GPP-compliant parameterization. In [114] the integration of orthogonal frequency-division multiplexing (OFDM) with FAMA was investigated as a means to facilitate broadband communication. Figure 2.11 presents the proposed transmitter and receiver block diagrams. On the transmitter side, the block follows the 5G-NR physical layer procedures, including channel coding and OFDM modulation. On the receiver side, a port selection mechanism was proposed based on subframe average SINR, that is, depending on the OFDM symbol and the subcarrier.

Link-level simulations were conducted considering the 3GPP tapped delay line (TDL) channel model [115] to assess the physical layer performance of OFDM-FAMA. The results of the block error rate (BLER) confirm the superior multiplexing gain offered by OFDM-FAMA, particularly in cases with robust channel coding and low spectrum efficiency.

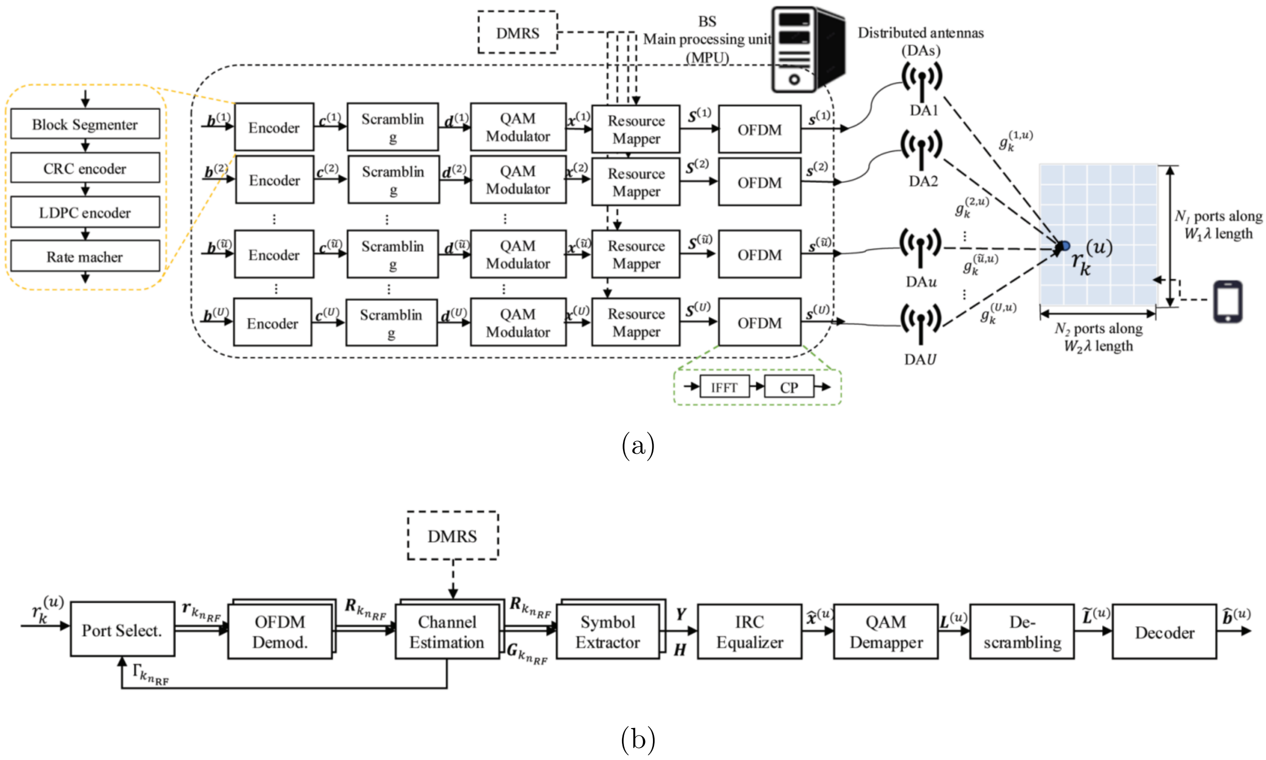

Figure 2.11. Model for OFDM-FAMA in 5G-NR: (a) transmitter block, (b) receiver block.
Source: [114] ©2025 IEEE.

CHAPTER 3

SLOW FAMA UNDER NAKAGAMI-m FADING CHANNELS

In this chapter, the performance of s-FAMA under Nakagami-m fading channels is studied, considering the constant correlation model [41].

3.1 RECEIVED SIGNAL MODEL FOR SLOW FAMA

The downlink FAMA system considered in this work is illustrated in Figure 3.1 and consists of a BS equipped with U distributed antennas, in which each antenna of this BS transmits a signal destined to a specific user of the network, thus constituting a network with U users. Each UE contains an 1D-FAS with N ports uniformly spaced along a linear array of dimension $W\lambda$, in which W is the normalized length of the FA and λ is the wavelength. The ports of a given UE are indexed by n, in which $n \in \{1, 2, \ldots, N\}$.

The received signal at the n-th port of the u user, with $u \in \{u = 1, 2, \ldots, U\}$, is written as [38]

$$r_n^{(u)} = s_u h_n^{(u,u)} + \sum_{\substack{\tilde{u}=1 \\ \tilde{u}\neq u}}^{U} s_{\tilde{u}} h_n^{(\tilde{u},u)} + \eta_n^{(u)}, \tag{3.1}$$

in which s_u denotes the transmitted symbol to the u-th user, $h_n^{(u,u)}$ is the corresponding fading channel coefficient experienced at the n-th port, $h_n^{(\tilde{u},u)}$ and $s_{\tilde{u}}$ represent, respectively, the interfering fading channel coefficient and the interfering symbol. Furthermore, $\eta_n^{(u)}$ is the complex AWGN, at the n-th port for the user u, with zero mean and variance σ_η^2. The average power of the transmitted symbol is $\sigma_s^2 = \mathbb{E}[|s_u|^2]$, $\forall u$. In this study, it is assumed that the switching delay between ports does not affect the system performance and can be neglected. Furthermore, it is assumed that the network has perfect knowledge of the CSI.

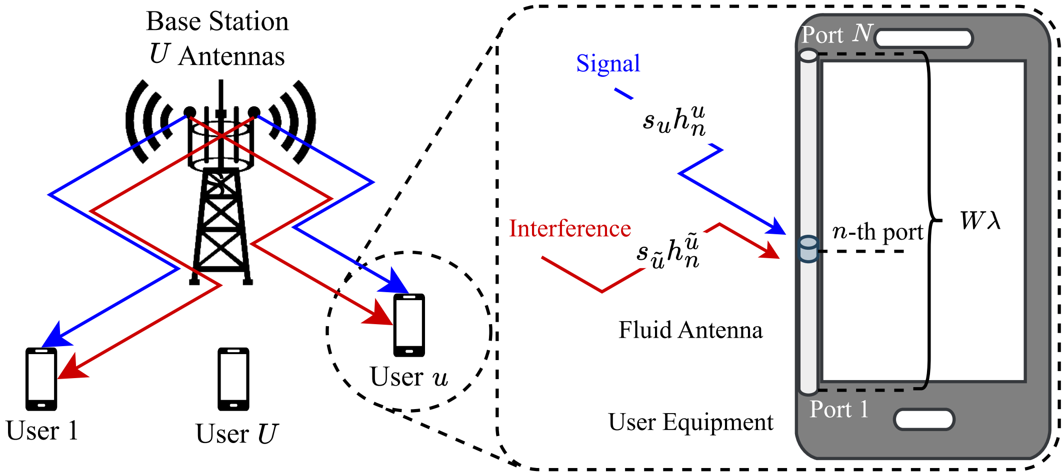

Figure 3.1. Downlink scenario for a FAMA network.

3.2 CHANNEL MODEL

The channel envelope at the n-th port for the u-th UE, denoted by $|h_n^{(u,u)}|$, is assumed Nakagami-m distributed with probability density function (PDF) given by [46]

$$p_{|h_n^{(u,u)}|}(r) = \frac{2\, m^m}{\Gamma(m)\, \Omega^m} r^{2m-1} e^{-\frac{mr^2}{\Omega}},\ r \geq 0, \tag{3.2}$$

with $m > 1/2$ being the fading parameter (also known as fading severity, fading factor, fading intensity or shape parameter), $\Omega = \mathbb{E}[|h_n^{(u,u)}|^2]$ (also known as scale parameter), and $\Gamma(\cdot)$ denoting the gamma function. A set of correlated Nakagami-m random variables (RVs) can be modeled as [40]

$$|h_n^{(u,u)}| = \sqrt{\sum_{l=1}^{m} |g_{nl}^{(u,u)}|^2}, \qquad n = 1, \ldots, N, \tag{3.3}$$

in which $\{g_{nl}^{(u,u)}\}$ is a set of complex Gaussian RVs with zero mean and variance $2\sigma_u^2$, defined as

$$g_{nl}^{(u,u)} = \sigma_u \left(\sqrt{1-\delta}\, x_{nl}^{(u,u)} + \sqrt{\delta}\, x_{0l}^{(u,u)}\right) + j\sigma_u \left(\sqrt{1-\delta}\, y_{nl}^{(u,u)} + \sqrt{\delta}\, y_{0l}^{(u,u)}\right), \tag{3.4}$$

where $x_{0l}^{(u,u)}, x_{1l}^{(u,u)}, \ldots, x_{Nl}^{(u,u)}$ and $y_{0l}^{(u,u)}, y_{1l}^{(u,u)}, \ldots, y_{Nl}^{(u,u)}$, with $l = 1, \ldots, m$, are all independent Gaussian RVs with zero mean and unity variance. It is modeled $\sigma_u = \sigma\ \forall u$. In (3.4), δ is the common power correlation coefficient between any pair of ports, which is modeled as the absolute average of the individual pairs of correlation coefficients, as described in Section 2.4.1

and repeated below

$$\delta = \left| \frac{2}{N(N-1)} \sum_{n=1}^{N-1} (N-n)\, \mathrm{J}_0\left(\frac{2\pi\, n\, W}{N-1}\right) \right|. \tag{3.5}$$

Note that the expressions (3.3) and (3.4) are also suitable for interfering users. In this case, the distribution parameters are denoted by $m_{\tilde{u}}$, $\sigma_{\tilde{u}} = \sigma$ and the set of independent Gaussian RVs, with zero mean and unity variance, are denoted by $x_{0l}^{(\tilde{u},u)}, x_{1l}^{(\tilde{u},u)}, \ldots, x_{Nl}^{(\tilde{u},u)}$ and $y_{0l}^{(\tilde{u},u)}, y_{1l}^{(\tilde{u},u)}, \ldots, y_{Nl}^{(\tilde{u},u)}$ with $l \in \{1, \ldots, m_{\tilde{u}}\}$.

3.3 SIR AND SINR MODELS

In the system evaluated in this work, it is assumed that the UE selects the port that maximizes the SINR of the communication link [38]. In this case, the SIR experienced by the u-th user can be determined based on the model in (3.1) and is expressed by

$$\mathrm{SIR} = \max_n \frac{\sigma_s^2 |h_n^{(u,u)}|^2}{\sigma_s^2 \sum_{\substack{\tilde{u}=1 \\ \tilde{u}\neq u}}^{U} |h_n^{(\tilde{u},u)}|^2} = \max_n \frac{X_n}{Y_n}, \tag{3.6}$$

in which

$$X_n = \sum_{l=1}^{m} \left[\left(x_{nl}^{(u,u)} + \sqrt{\frac{\delta}{1-\delta}}\, x_{0l}^{(u,u)} \right)^2 + \left(y_{nl}^{(u,u)} + \sqrt{\frac{\delta}{1-\delta}}\, y_{0l}^{(u,u)} \right)^2 \right] \tag{3.7}$$

and

$$Y_n = \sum_{\substack{\tilde{u}=1 \\ \tilde{u}\neq u}}^{U} \sum_{l=1}^{m_{\tilde{u}}} \left[\left(x_{nl}^{(\tilde{u},u)} + \sqrt{\frac{\delta}{1-\delta}}\, x_{0l}^{(\tilde{u},u)} \right)^2 + \left(y_{nl}^{(\tilde{u},u)} + \sqrt{\frac{\delta}{1-\delta}}\, y_{0l}^{(\tilde{u},u)} \right)^2 \right]. \tag{3.8}$$

Note that X_n and Y_n are obtained by dividing the numerator and denominator of SIR_n by $\sigma^2\sigma_s^2(1-\delta)$.

Including the noise power in (3.6), the SINR is given by

$$\mathrm{SINR} = \max_n \frac{\sigma_s^2 |h_n^{(u,u)}|^2}{\sigma_s^2 \sum_{\substack{\tilde{u}=1 \\ \tilde{u}\neq u}}^{U} |h_n^{(\tilde{u},u)}|^2 + \sigma_\eta^2} = \max_n \frac{X_n}{Y_n + \sigma_\eta^2/[\sigma^2\sigma_s^2(1-\delta)]}. \tag{3.9}$$

3.4 SLOW FAMA UNDER NAKAGAMI-m CHANNELS

This section presents the derivations of the performance metrics for slow FAMA under Nakagami-m fading. The key metrics examined are the OP and the multiplexing gain. The OP quantifies the probability that the SIR or SINR experienced by users falls below a specified target threshold. In turn, multiplexing gain measures the enhancement in data transmission capacity achieved by the use of FAs for multiple access.

3.4.1 Statistics for X_n and Y_n

To deduce performance metrics related to the slow FAMA under Nakagami-m channels, some statistics on X_n, given by (3.7), and Y_k, given by (3.8), must be found. To obtain the multivariate PDF of X_k in (3.7), it is first conditioned to the RV

$$r_0 = \sum_{l=1}^{m} (x_{0l}^{(u,u)})^2 + (y_{0l}^{(u,u)})^2. \tag{3.10}$$

Note that $X_n|r_0$ can be characterized by a noncentral Chi-squared distribution with $2m$ DoFs, whose PDF is given by [116, Eq. (2.3-29)]

$$p_{X_n|r_0}(x_n) = \frac{1}{2}\left(\frac{x_n}{\frac{\delta}{1-\delta}r_0}\right)^{\frac{m-1}{2}} e^{-\frac{x_n+\frac{\delta}{1-\delta}r_0}{2}}\, \mathrm{I}_{m-1}\left(\sqrt{\frac{\delta\, r_0\, x_n}{1-\delta}}\right), \tag{3.11}$$

in which $\mathrm{I}_\nu(\cdot)$ is the ν-order modified Bessel function of the first kind. As all $X_n|r_0$ are independent for any n, it follows that the multivariate PDF is the product of individual PDFs

$$p_{X_1,\ldots,X_N|r_0}(x_1,\ldots,x_N) = \prod_{n=1}^{N}\frac{1}{2}\left(\frac{x_n}{\frac{\delta}{1-\delta}r_0}\right)^{\frac{m-1}{2}} e^{-\frac{x_n+\frac{\delta}{1-\delta}r_0}{2}}\, \mathrm{I}_{m-1}\left(\sqrt{\frac{\delta\, r_0\, x_n}{1-\delta}}\right). \tag{3.12}$$

The unconditional PDF can be derived by applying

$$p_{X_1,\ldots,X_N}(x_1,\ldots,x_N) = \int_0^\infty p_{X_1,\ldots,X_N|r_0}(x_1,\ldots,x_N)\, p_{r_0}(r)dr. \tag{3.13}$$

Note that r_0 is a central Chi-squared distribution with $2m$ degrees of freedom with PDF given by [116, Eq. (2.3-21)]

$$p_{r_0}(r) = \frac{r^{m-1}e^{-\frac{r}{2}}}{2^m\Gamma(m)}. \tag{3.14}$$

By using (3.13), the multivariate cumulative distribution function (CDF) can be calculated as

$$
\begin{aligned}
F_{X_1,\dots,X_N}(t_1,\dots,t_N) &\overset{(a)}{=} \int_0^{t_1}\cdots\int_0^{t_N} p_{X_1,\dots,X_N}(x_1,\dots,x_N)\mathrm{d}x_1,\dots,\mathrm{d}x_N \\
&\overset{(b)}{=} \int_0^{t_1}\cdots\int_0^{t_N}\int_{r=0}^{\infty} \frac{r^{m-1}e^{-\frac{r}{2}}}{2^m\Gamma(m)} \prod_{n=1}^{N} \left(\frac{x_n}{\frac{\delta}{1-\delta}r}\right)^{\frac{m-1}{2}} \frac{e^{-\frac{x_n+\frac{\delta}{1-\delta}r_0}{2}}}{2} \mathrm{I}_{m-1}\left(\sqrt{\frac{\delta\, r\, x_n}{1-\delta}}\right)\mathrm{d}r\,\mathrm{d}x_1,\dots,\mathrm{d}x_N \\
&\overset{(c)}{=} \int_{r=0}^{\infty} \frac{r^{m-1}e^{-\frac{r}{2}}}{2^m\Gamma(m)} \prod_{n=1}^{N}\int_0^{t_n} \left(\frac{x_n}{\frac{\delta}{1-\delta}r}\right)^{\frac{m-1}{2}} \frac{e^{-\frac{x_n+\frac{\delta}{1-\delta}r}{2}}}{2} \mathrm{I}_{m-1}\left(\sqrt{\frac{\delta\, r\, x_n}{1-\delta}}\right)\mathrm{d}x_n\,\mathrm{d}r \\
&\overset{(d)}{=} \int_0^{\infty} \frac{r^{m-1}e^{-\frac{r}{2}}}{2^m\Gamma(m)} \prod_{n=1}^{N}\left[1-\mathrm{Q}_m\left(\sqrt{\frac{\delta\, r}{1-\delta}},\sqrt{t_n}\right)\right]\mathrm{d}r,
\end{aligned}
\tag{3.15}
$$

in which (a) uses the definition of a multivariate CDF; (b) replaces the expressions of $p_{r_0}(r)$ and $p_{X_1,\dots,X_N|r_0}(x_1,\dots,x_N)$ in (3.13) to obtain the multivariate PDF; (c) changes the order of integration of the variables $x_1,\dots,x_N$ and r, and writes the multivariate integral as a product of N single integrals in the variable x_n; and (d) uses the fact that the integration over x_n is the CDF of a non-central Chi-squared distribution with $2m$ DoFs [116, Eq. (2.3-35)], where $\mathrm{Q}_m(\cdot\,,\,\cdot)$ is the Marcum-Q function of order m.

In turn, the multivariate PDF of Y_n in (3.8) can be obtained by conditioning Y_n to the RV

$$
\widetilde{r}_0 = \sum_{\substack{\tilde{u}=1\\ \tilde{u}\neq u}}^{U}\sum_{l=1}^{m_{\tilde{u}}} (x_{0l}^{(\tilde{u},u)})^2 + (y_{0l}^{(\tilde{u},u)})^2. \tag{3.16}
$$

Thus, $Y_n|\widetilde{r}_0$ is a noncentral Chi-squared distribution with $2\,\widetilde{U}$ DoFs, in which

$$
\widetilde{U} = \sum_{\substack{\tilde{u}=1\\ \tilde{u}\neq u}}^{U} m_{\tilde{u}}, \tag{3.17}
$$

resulting in a PDF described by

$$
p_{Y_n|\widetilde{r}_0}(y_n) = \frac{1}{2}\left(\frac{y_n}{\frac{\delta}{1-\delta}\widetilde{r}_0}\right)^{\frac{\widetilde{U}-1}{2}} e^{-\frac{y_n+\frac{\delta}{1-\delta}\widetilde{r}_0}{2}}\ \mathrm{I}_{\widetilde{U}-1}\left(\sqrt{\frac{\delta}{1-\delta}}\sqrt{\widetilde{r}_0 y_n}\right). \tag{3.18}
$$

As all $Y_n|\widetilde{r}_0$ are independent for any n, the conditional multivariate PDF is the product of individual PDFs as

$$
p_{Y_1,\dots,Y_N|\widetilde{r}_0}(y_1,\dots,y_N) = \prod_{n=1}^{N} p_{Y_n|\widetilde{r}_0}(y_n). \tag{3.19}
$$

Similarly to X_n, and knowing that $\widetilde{r}_0$ in a central Chi-squared distribution with $2\,\widetilde{U}$ DoFs, it follows that

$$
\begin{aligned}
p_{Y_1,\ldots,Y_N}(y_1,\ldots,y_N) = & \int_{\widetilde{r}=0}^{\infty} \frac{\widetilde{r}^{\widetilde{U}-1} e^{-\frac{\widetilde{r}}{2}}}{2^{\widetilde{U}}\Gamma(\widetilde{U})} \\
& \times \prod_{n=1}^{N} \frac{1}{2}\left(\frac{y_n}{\frac{\delta}{1-\delta}\widetilde{r}}\right)^{\frac{\widetilde{U}-1}{2}} e^{-\frac{y_n+\frac{\delta}{1-\delta}\widetilde{r}}{2}} \mathrm{I}_{\widetilde{U}-1}\left(\sqrt{\frac{\delta}{1-\delta}}\sqrt{\widetilde{r} y_n}\right) \mathrm{d}\widetilde{r}. \qquad (3.20)
\end{aligned}
$$

3.4.2 The OP Based on the SIR

In this subsection, an expression for the OP based on SIR is derived. This OP is denoted by $P_{\text{out}} = \text{Prob}(\text{SIR} < \gamma)$, in which γ is a given SIR threshold, and can be developed as follows:

$$
\begin{aligned}
P_{\text{out}} & \overset{(a)}{=} \text{Prob}\left(\frac{X_1}{Y_1} < \gamma, \ldots, \frac{X_N}{Y_N} < \gamma\right) = \text{Prob}\left(X_1 < \gamma Y_1, \ldots, X_N < \gamma Y_N\right) \\
& \overset{(b)}{=} \int_0^{\infty} \cdots \int_0^{\infty} F_{X_1,\ldots,X_N|Y_1,\ldots,Y_N}(\gamma\, y_1,\ldots,\gamma\, y_N)\, p_{Y_1,\ldots,Y_N}(y_1,\ldots,y_N)\, \mathrm{d}y_1,\ldots,\mathrm{d}y_N \\
& \overset{(c)}{=} \underbrace{\int_0^{\infty} \cdots \int_0^{\infty}}_{y_1 \cdots y_N} \int_{r=0}^{\infty} \frac{r^{m-1}}{2^m \Gamma(m)} e^{-\frac{r}{2}} \prod_{n=1}^{N} \left[1 - \mathrm{Q}_m\left(\sqrt{\frac{\delta\, r}{1-\delta}}, \sqrt{\gamma\, y_n}\right)\right] \mathrm{d}r \\
& \times \int_{\widetilde{r}=0}^{\infty} \frac{\widetilde{r}^{\widetilde{U}-1} e^{-\frac{\widetilde{r}}{2}}}{2^{\widetilde{U}}\Gamma(\widetilde{U})} \prod_{n=1}^{N} \frac{1}{2}\left(\frac{y_n}{\frac{\delta}{1-\delta}\widetilde{r}}\right)^{\frac{\widetilde{U}-1}{2}} e^{-\frac{y_n+\frac{\delta}{1-\delta}\widetilde{r}}{2}} \mathrm{I}_{\widetilde{U}-1}\left(\sqrt{\frac{\delta}{1-\delta}}\sqrt{\widetilde{r} y_n}\right) \mathrm{d}\widetilde{r}\, \mathrm{d}y_1,\ldots,\mathrm{d}y_N \\
& \overset{(d)}{=} \int_0^{\infty}\int_0^{\infty} \frac{r^{m-1}\widetilde{r}^{\widetilde{U}-1}}{2^{(m+\widetilde{U})}\Gamma(m)\Gamma(\widetilde{U})} e^{-\frac{r+\widetilde{r}}{2}} \prod_{n=1}^{N} \int_{y_n=0}^{\infty} \left[1 - \mathrm{Q}_m\left(\sqrt{\frac{\delta\, r}{1-\delta}}, \sqrt{\gamma\, y_n}\right)\right] \\
& \times \frac{1}{2}\left(\frac{y_n}{\frac{\delta}{1-\delta}\widetilde{r}}\right)^{\frac{\widetilde{U}-1}{2}} e^{-\frac{y_n+\frac{\delta}{1-\delta}\widetilde{r}}{2}} \mathrm{I}_{\widetilde{U}-1}\left(\sqrt{\frac{\delta}{1-\delta}}\sqrt{\widetilde{r} y_n}\right) \mathrm{d}y_n\, \mathrm{d}r\, \mathrm{d}\widetilde{r} \\
& \overset{(e)}{=} \int_0^{\infty}\int_0^{\infty} \frac{r^{m-1}\widetilde{r}^{\widetilde{U}-1}}{2^{(m+\widetilde{U})}\Gamma(m)\Gamma(\widetilde{U})} e^{-\frac{r+\widetilde{r}}{2}} \prod_{n=1}^{N} \Bigg[1 - \int_{y_n=0}^{\infty} \mathrm{Q}_m\left(\sqrt{\frac{\delta\, r}{1-\delta}}, \sqrt{\gamma\, y_n}\right) \\
& \times \frac{1}{2}\left(\frac{y_n}{\frac{\delta}{1-\delta}\widetilde{r}}\right)^{\frac{\widetilde{U}-1}{2}} e^{-\frac{y_n+\frac{\delta}{1-\delta}\widetilde{r}}{2}} \mathrm{I}_{\widetilde{U}-1}\left(\sqrt{\frac{\delta}{1-\delta}}\sqrt{\widetilde{r} y_n}\right) \mathrm{d}y_n \Bigg] \mathrm{d}r\, \mathrm{d}\widetilde{r}, \qquad (3.21)
\end{aligned}
$$

in which (a) follows from (3.6); (b) calculates the unconditional CDF by averaging the conditional CDF over the PDF of Y_n; (c) is valid since $X_1,\ldots,X_N$ and $Y_1,\ldots,Y_N$ are independent, and based on (3.15) and (3.20); (d) changes the order of integration and writes the multivariate integral as a product of N single integrals in the variable y_n; and (e) derives from the fact that the first integral over y_n is one, as it is the total probability of a noncentral Chi-squared distribution with $2\,\widetilde{U}$ DoFs.

The inner integral over y_n in step (e) in (3.21) is rewritten as

$$\mathcal{I} = \frac{1}{2}\left(\frac{1}{\frac{\delta}{1-\delta}\widetilde{r}}\right)^{\frac{\widetilde{U}-1}{2}} e^{-\frac{\frac{\delta}{1-\delta}\widetilde{r}}{2}} \int_{y_n=0}^{\infty} \mathrm{Q}_m\left(\sqrt{\frac{\delta\, r}{1-\delta}}, \sqrt{\gamma\, y_n}\right) y_n^{\frac{\widetilde{U}-1}{2}} e^{-\frac{y_n}{2}} \mathrm{I}_{\widetilde{U}-1}\left(\sqrt{\frac{\delta}{1-\delta}}\sqrt{\widetilde{r} y_n}\right) \mathrm{d}y_n. \tag{3.22}$$

This integral can be recognized as the Laplace Transform involving the product of generalized Marcum-Q, modified Bessel and power functions, with closed-form solution presented by Ermolova and Tirkkonen [117]. Using [117, Corollary 3, Eq.(25)], with $a = \sqrt{\gamma}$, $b = \sqrt{\delta\, r/(1-\delta)}$, $c = \sqrt{\delta\, \widetilde{r}/(1-\delta)}$ and [117, Proposition 1] it follows that

$$\begin{aligned}
&\int_0^{\infty} \mathrm{Q}_m(b, a\sqrt{y_n}) y_n^{\frac{\widetilde{U}-1}{2}} e^{-\frac{y_n}{2}} \mathrm{I}_{\widetilde{U}-1}(c\, y_n)\mathrm{d}y_n \\
&= 2c^{\widetilde{U}-1} e^{\frac{c^2}{2}} - 2c^{\widetilde{U}-1} e^{\frac{c^2}{2}} \mathrm{Q}_{\widetilde{U}}\left(\frac{ac}{\sqrt{a^2+1}}, \frac{b}{\sqrt{a^2+1}}\right) \\
&+ \frac{2}{c}\left(\frac{c}{a^2+1}\right)^{\widetilde{U}+m-1}\left(\frac{b}{a}\right)^{1-m} \exp\left(\frac{c^2-b^2}{2(a^2+1)}\right) \\
&\times \sum_{k=0}^{\widetilde{U}+m-2}\sum_{j=0}^{\widetilde{U}+m-k-2}\left(\frac{b}{c}\right)^{j+k}\left(\frac{a^2+1}{a}\right)^{n}(-a)^j \frac{(-\widetilde{U}-m+k+2)_j}{j!} \mathrm{I}_{1-m+k+j}\left(\frac{a\, b\, c}{a^2+1}\right)
\end{aligned} \tag{3.23}$$

is obtained, in which $(x)_j$ denotes the Pochhammer symbol.

Using Pochhammer symbol property $(-x)_j = (-1)^j(x-j+1)_n$, it follows that

$$\left(\frac{a^2+1}{a}\right)^{k}(-a)^j \frac{(-\widetilde{U}-m+k+2)_j}{j!} = (a^2+1)^k (a)^{j-k} \frac{(\widetilde{U}+m-k-j-1)_j}{j!}. \tag{3.24}$$

Thus, plugging (3.24) in (3.23) and the resulting expression into (3.22), the integral $\mathcal{I}$ is solved. Replacing the previous result in step (e) of (3.21) and proceeding with some algebric simplifications, the SIR-based OP of a slow FAMA user over Nakagami-m channels is given by

$$\begin{aligned}
P_{\text{out}} = &\int_{\widetilde{r}=0}^{\infty}\int_{r=0}^{\infty} \frac{r^{m-1}\widetilde{r}^{\widetilde{U}-1} e^{-\frac{r+\widetilde{r}}{2}}}{2^{m+\widetilde{U}}\Gamma(m)\Gamma(\widetilde{U})} \\
&\Bigg[\mathrm{Q}_{\widetilde{U}}\left(\sqrt{\frac{\delta\gamma\,\widetilde{r}}{(1-\delta)(\gamma+1)}}, \sqrt{\frac{\delta r}{(1-\delta)(\gamma+1)}}\right) - \left(\frac{1}{\gamma+1}\right)^{m+\widetilde{U}-1}\left(\frac{r}{\gamma\,\widetilde{r}}\right)^{\frac{1-m}{2}} e^{-\frac{\delta}{2(1-\delta)}\left(\frac{\gamma\widetilde{r}+r}{\gamma+1}\right)} \\
&\times \sum_{k=0}^{m+\widetilde{U}-2}\sum_{j=0}^{m+\widetilde{U}-k-2} \frac{(m+\widetilde{U}-(j+k)-1)_j}{j!}\left(\frac{r}{\widetilde{r}}\right)^{\frac{j+k}{2}} \frac{(\gamma+1)^n}{\gamma^{\frac{k-j}{2}}} \mathrm{I}_{1-m+j+k}\left(\frac{\delta\sqrt{\gamma\, r\,\widetilde{r}}}{(1-\delta)(\gamma+1)}\right)\Bigg]^N \mathrm{d}r\,\mathrm{d}\widetilde{r}.
\end{aligned} \tag{3.25}$$

As a sanity check, the SIR-based OP expression for a slow FAMA user over Rayleigh channels, given in [38, Eq. (21)] can be easily obtained from (3.25) by making $m = 1$ and $m_{\tilde{u}} = 1\ \forall\, \tilde{u}$, which results in $\widetilde{U} = U - 1$ and $\delta = \mu^2$.

3.4.3 Upper Bounds for the OP based on the SIR

Following the proof presented in Appendix A, it is found that the OP expressed in (3.25) is upper bounded, for large N and γ, by

$$P_{\text{out}} < \left[1 - \left(N\left(\frac{1-\delta}{\gamma}\right)^{\widetilde{U}} + N\left(\frac{\delta}{\gamma+1}\right)^{\widetilde{U}}\right) \sum_{i=0}^{m-1} \frac{(\widetilde{U})_{m-i-1}}{(m-i-1)!}\right]^{+}, \tag{3.26}$$

where $(a)^{+} = \max\{0, a\}$. For small δ and large γ, (3.26) can be simplified by

$$P_{\text{out}} < \left[1 - N\left(\frac{1-\delta}{\gamma}\right)^{\widetilde{U}} \sum_{i=0}^{m-1} \frac{(\widetilde{U})_{m-i-1}}{(m-i-1)!}\right]^{+}. \tag{3.27}$$

Furthermore, for $W \geq 1$, the upper bound can also be expressed as

$$P_{\text{out}} < \left[1 - N\left(\frac{1-\frac{1}{\pi W}}{\gamma}\right)^{\widetilde{U}} \sum_{i=0}^{m-1} \frac{(\widetilde{U})_{m-i-1}}{(m-i-1)!}\right]^{+}. \tag{3.28}$$

The approximations applied and the necessary conditions that ensure the accuracy of the bound are described in the Appendix A.

3.4.4 Multiplexing Gain

An important performance metric in the FAMA system is the evaluation of the number of users (and BS antennas) that maximize multiplexing gain. The multiplexing gain of the system, denoted as $\mathcal{G}_m$, can be defined as [38, Eq. (29)]

$$\mathcal{G}_m = U\,(1 - P_{\text{out}}). \tag{3.29}$$

The optimal number of users, represented as $U^{\star}$, is determined based on the bounds of the multiplexing gain. In a high SIR regime, where Prob(SIR $< \gamma) \to 0$, the multiplexing gain expressed in (3.29) is maximum at $\mathcal{G}_m = U$, that is $\mathcal{G}_m < U$. Applying the upper bound of the SIR-based OP described in (3.28), it is observed that the multiplexing gain is bounded in the range

$$\min\left\{N\,U\left(\frac{1-\frac{1}{\pi W}}{\gamma}\right)^{\widetilde{U}} \sum_{i=0}^{m-1} \frac{(m-1)!(\widetilde{U})_{m-i-1}}{(m-i-1)!},\, U\right\} \leq \mathcal{G}_m \leq U. \tag{3.30}$$

The optimal number of users, represented as $U^{\star}$, is the inflection point of the curve of $\mathcal{G}_m$ as a function of U. By equating the bounds in (3.30) and isolating the number of users, the optimal value $U^\star$ can be found by solving the equation

$$U^\star = \left\lfloor \frac{\ln\left(\sum_{n=0}^{m-1} \frac{m(U^\star-1)_{m-1-k}}{(m-1-k)!}\right) + \ln N}{m \ln\left(\frac{\gamma}{1-\frac{1}{\pi W}}\right)} + 1 \right\rfloor, \tag{3.31}$$

in which $m_{\widetilde{u}} = m, \forall u$. It should be noted that (3.31) in a transcendental equation for $m \geq 2$, but can be easily solved using well-known software packages such as Mathematica® or MATLAB®.

3.4.5 The OP Based on the SINR

The SINR-based OP, denoted by $P_{\text{out}} = \text{Prob}(\text{SINR} < \gamma)$ with γ being a given SINR threshold, is evaluated as

$$\begin{aligned} P_{\text{out}} &= \text{Prob}\left(\frac{X_1}{Y_1 + \frac{\sigma_\eta^2}{\sigma^2\sigma_s^2(1-\delta)}} < \gamma, \ldots, \frac{X_N}{Y_N + \frac{\sigma_\eta^2}{\sigma^2\sigma_s^2(1-\delta)}} < \gamma\right) \\ &= \text{Prob}\left(X_1 < \gamma\, Y_1 + \frac{\gamma\,\sigma_\eta^2}{\sigma^2\sigma_s^2(1-\delta)}, \ldots, X_N < \gamma\, Y_N + \frac{\gamma\,\sigma_\eta^2}{\sigma^2\sigma_s^2(1-\delta)}\right), \end{aligned} \tag{3.32}$$

which follows from (3.9). Note that the expressions in (3.32) and in step (a) of (3.21) are almost the same, except for the term $\gamma\, Y_n + \frac{\gamma\,\sigma_\eta^2}{\sigma^2\sigma_s^2(1-\delta)}$. So, following the same steps presented in (3.21), the OP considering a slow FAMA user over Nakagami-m channels based on SINR, is given by

$$\begin{aligned} P_{\text{out}} = \int_0^\infty \int_0^\infty & \frac{r^{m-1}\widetilde{r}^{\widetilde{U}-1} e^{-\frac{r+\widetilde{r}}{2}}}{2^{m+\widetilde{U}}\Gamma(m)\Gamma(\widetilde{U})} \left[1 - \prod_{n=1}^{N} \int_{y_n=0}^{\infty} \frac{1}{2} \mathrm{Q}_m\left(\sqrt{\frac{\delta\, r}{1-\delta}}, \sqrt{\gamma\, y_n + \frac{2\, m\, \gamma}{\Upsilon(1-\delta)}}\right)\right. \\ & \left. \times \left(\frac{y_n}{\frac{\delta}{1-\delta}\widetilde{r}}\right)^{\frac{\widetilde{U}-1}{2}} e^{-\frac{y_n + \frac{\delta}{1-\delta}\widetilde{r}}{2}} \mathrm{I}_{\widetilde{U}-1}\left(\sqrt{\frac{\delta}{1-\delta}}\sqrt{\widetilde{r} y_n}\right) \mathrm{d}y_n \right] \mathrm{d}r\, \mathrm{d}\widetilde{r}, \end{aligned} \tag{3.33}$$

where Υ is the average received SNR, calculated as

$$\Upsilon = \frac{2\, m\, \sigma^2\, \sigma_s^2}{\sigma_\eta^2}. \tag{3.34}$$

3.4.6 Approximation of the OP Based on the SINR

An approximation for the SINR-based OP presented in (3.33) can be found by using the Gauss-Laguerre quadrature (GLQ) method [118]. This technique enables a numerical approximation of integral expressions, significantly reducing the computational cost of evaluations. Following the demonstration presented in Appendix B, the SINR-based OP approximation is given by

$$P_{\text{out}} \approx \frac{1}{\Gamma(m)\,\Gamma(\widetilde{U})} \sum_{l=1}^{n} w_l\, {x_l}^{m-1} \sum_{j=1}^{n} w_j\, {x_j}^{\widetilde{U}-1} \Bigg[1 - \frac{1}{2}\sum_{i=1}^{n} w_i$$
$$\times\, \mathrm{Q}_m\left(\sqrt{\frac{2\,\delta\, x_l}{1-\delta}}, \sqrt{\gamma x_i + \frac{2\,m\,\gamma}{\Upsilon(1-\delta)}}\right)\left(\frac{x_i}{\frac{2\,\delta}{1-\delta}x_j}\right)^{\frac{\widetilde{U}-1}{2}} e^{\left(\frac{x_i}{2}-\frac{\delta}{1-\delta}x_j\right)}\, \mathrm{I}_{\widetilde{U}-1}\left(\sqrt{\frac{2\,\delta\, x_i\, x_j}{1-\delta}}\right)\Bigg]^N, \quad (3.35)$$

with x_i denoting the roots of the Laguerre polynomial $L_n(x)$ and w_i representing the quadrature weights, which depend on the number of roots n, where

$$w_i = \frac{x_i}{(n+1)^2[L_{n+1}(x_i)]^2}. \quad (3.36)$$

For a given number of roots, the computational complexity of the quadrature-based expression in (3.35) is on the order of $\mathcal{O}(n^3)$. Employing approximately 30 roots typically provides a favorable compromise between numerical accuracy and computational efficiency.

Alternatively, the generalized GLQ could be employed. In the following chapters, this approach is used for other OP approximations.

3.5 NUMERICAL RESULTS

This section presents the analytical and numerical results related to the performance metrics studied in this work[1]. In addition, Monte Carlo simulation results are presented in order to validate the derived expressions. These simulations replicate the system described in Section 3.1. Initially, the mutually correlated Gaussian RVs, denoted as $g_{nl}^{(u,u)}$ in (3.4), are generated numerically. These RVs are then used to construct the channel coefficients $h_n^{(u,u)}$, essential for computing the desired channel and interference terms. This process allows the determination of the RVs expressed in (3.6) and (3.9), representing the SIR and SINR experienced by a given user, respectively. The OP is calculated by determining the frequency at which the SIR and SINR numerical samples fall below a given threshold γ. To ensure that the simulation results closely match the theoretical curves, at least 5×10^5 SIR and SINR samples are generated for each system configuration considered. In the presented results, it is assumed that all users are subject to channels with the same fading parameter $m = m_{\tilde{u}}, \forall \tilde{u}$.

[1] The codes used are available at https://github.com/deMouraPaulo/FAMA

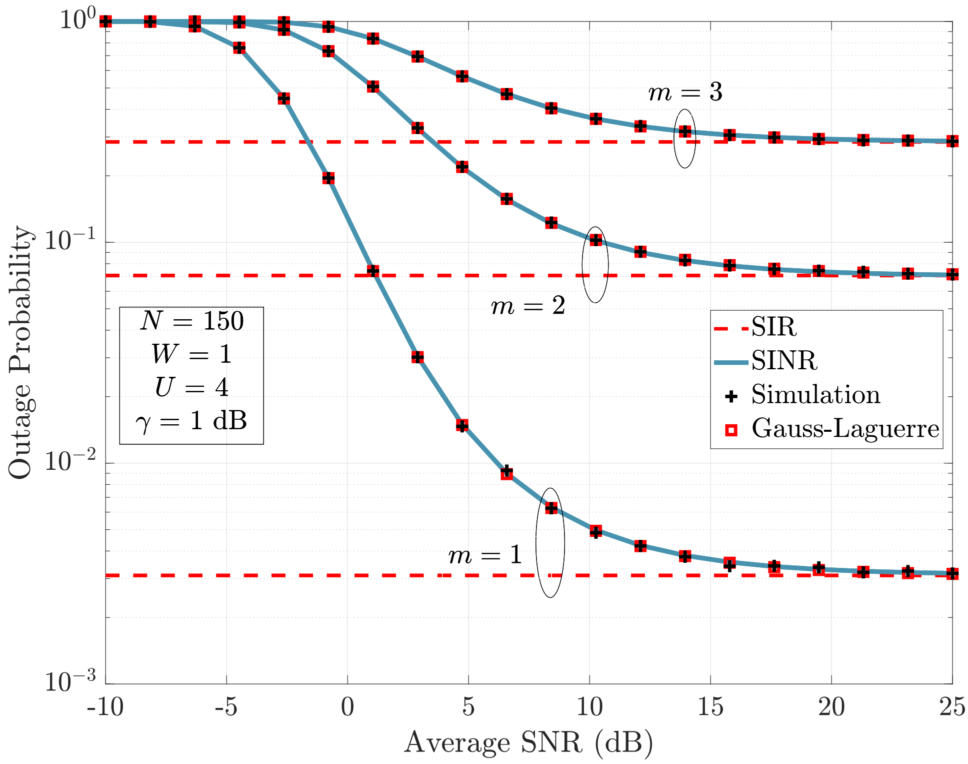

Figure 3.2. SIR-based and SINR-based OP curves as a function of the average SNR for channels with different fading parameters m, considering $U = 4$, $N = 150$, $W = 1$ and $\gamma = 1$ dB.

Figure 3.2 shows the OP curves of the FAMA system, based on SIR and SINR, expressed in (3.25) and (3.33), respectively, for different fading parameters m. In this analysis, the network is assumed to have $U = 4$ users, each equipped with FAs featuring $N = 150$ ports and a normalized length of $W = 1$. The results show that as the average SNR increases, the SINR-based OP curves converge toward the SIR-based OP curves. In a high SNR regime, interference becomes the dominant factor influencing the OP metric in the FAMA system, and noise can be effectively neglected. This is due to the significant interference contribution from the $U - 1$ other users. Additionally, an irreducible plateau in the OP is noted, resulting from the combined effects of fading and interference. Furthermore, it is observed that as the fading parameter m increases, the OP worsens, indicating degraded communication conditions. This occurs because higher values of m correspond to more line-of-sight-like behavior, reducing the fading effects. As a result, the FAMA system has fewer opportunities to exploit signal envelope variations and peaks, leading to increased interference and a higher OP. Note that in the case of non-FAMA systems, increasing the m values results in better performance as the system becomes more deterministic. In fact, in order to provide multiple access, the FAMA system utilizes the

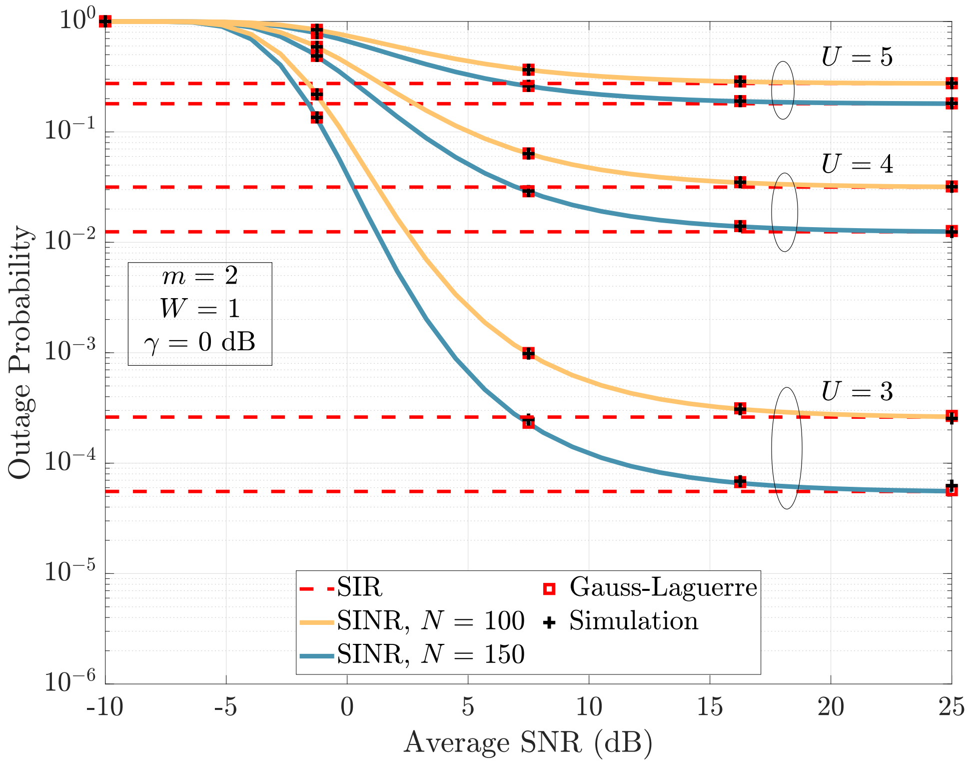

Figure 3.3. SIR-based and SINR-based OP curves as a function of the average SNR for different numbers of users, considering $m = 2$, $\gamma = 0$ dB, $W = 1$ and $N \in \{100{,}150\}$.

deep fades of interference, which occur more frequently in harsh environments such as those with lower m values. The derived analytical expressions strongly agree with the Monte Carlo simulation results, validating their applicability across different scenarios. Furthermore, the Gauss-Laguerre quadrature approximation of the SINR-based OP is accurate when employing 30 summation terms in the GLQ to approximate each integral.

Figure 3.3 presents the OP curves as a function of the average SNR for different numbers of users in the network. It is assumed that the channels are characterized by a fading factor equal to $m = 2$, and that $\gamma = 0$ dB, $W = 1$, and $N \in \{100, 150\}$. These results enable an assessment of the impact of interference on the FAMA system. A given user experiences interference from the other $U - 1$ users, significantly reducing its SINR and increasing the observed OP. For instance, in a network with $U = 3$ users, operating at an average SNR of 10 dB, with $N = 100$ ports, the OP is approximately 5.5×10^{-4}. Adding one more user to this network raises the OP to around 4.7×10^{-2}. Furthermore, increasing the number of ports enhances system performance. In the scenario of 3 users with an average SNR of 20 dB, expanding the number of ports from 100 to 150 results in an approximately 5.35-fold improvement in OP.

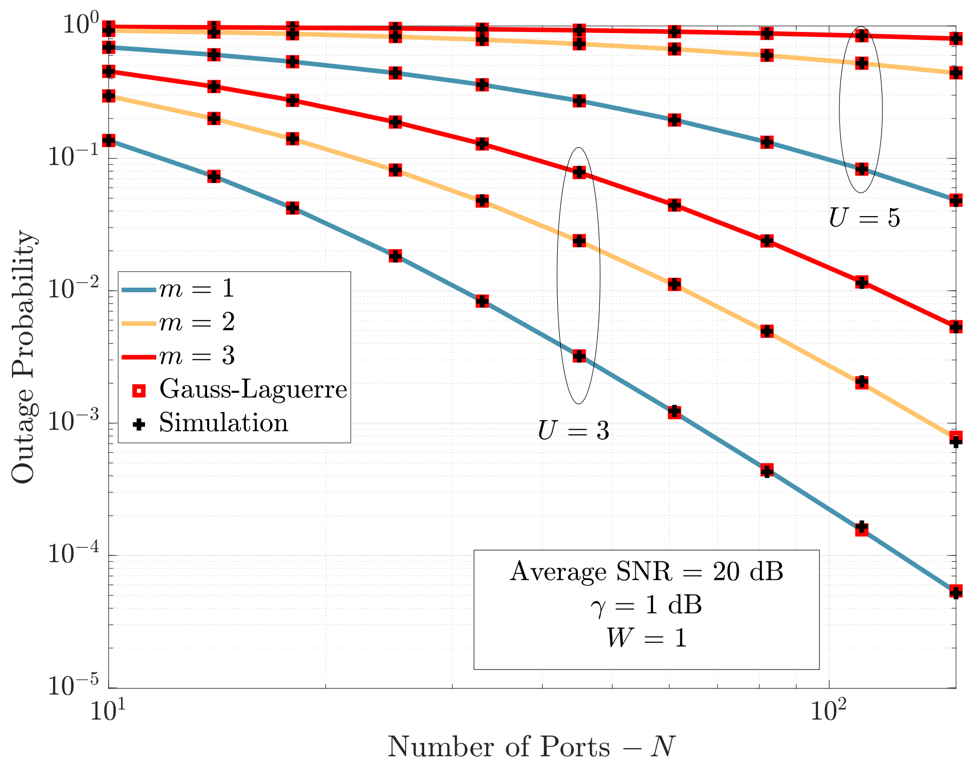

Figure 3.4. SINR-based OP curves as a function of the number of ports N for networks with $U = 3$ users and $U = 5$ users, considering an average SNR of 20 dB, $\gamma = 1$ dB and $W = 1$.

Figure 3.4 illustrates the OP curves, as expressed in (3.33), as a function of the number of ports N under different fading conditions, with an average SNR of 20 dB, $\gamma = 1$ dB and $W = 1$. These results indicate that increasing the number of ports in the UE effectively reduces OP levels. However, interference introduced by adding more users to the network poses a significant limitation for the FAMA system under Nakagami-m fading. For instance, in the scenario with $m = 2$ and $N = 100$, increasing the number of users from $U = 3$ to $U = 5$ results in a substantial rise in OP, from approximately 2.7×10^{-3} to approximately 0.55, due to the increase in interference. Due to the adoption of a constant correlation model, the saturation behavior of the OP as a function of N is not captured. However, in Chapter 4, where a more accurate correlation model is employed, the saturation of the OP with increasing N becomes evident.

In turn, Figure 3.5 evaluates the dependence of the OP on the physical size of the FA, represented by W. In this analysis, two SINR thresholds are considered, $\gamma = 2$ dB and $\gamma = 3$ dB, for networks with $U = 3$ and $U = 4$ users, with an average SNR of 20 dB, $N = 100$ and $m = 2$. As W increases, more space is available, and therefore, the OP values decrease

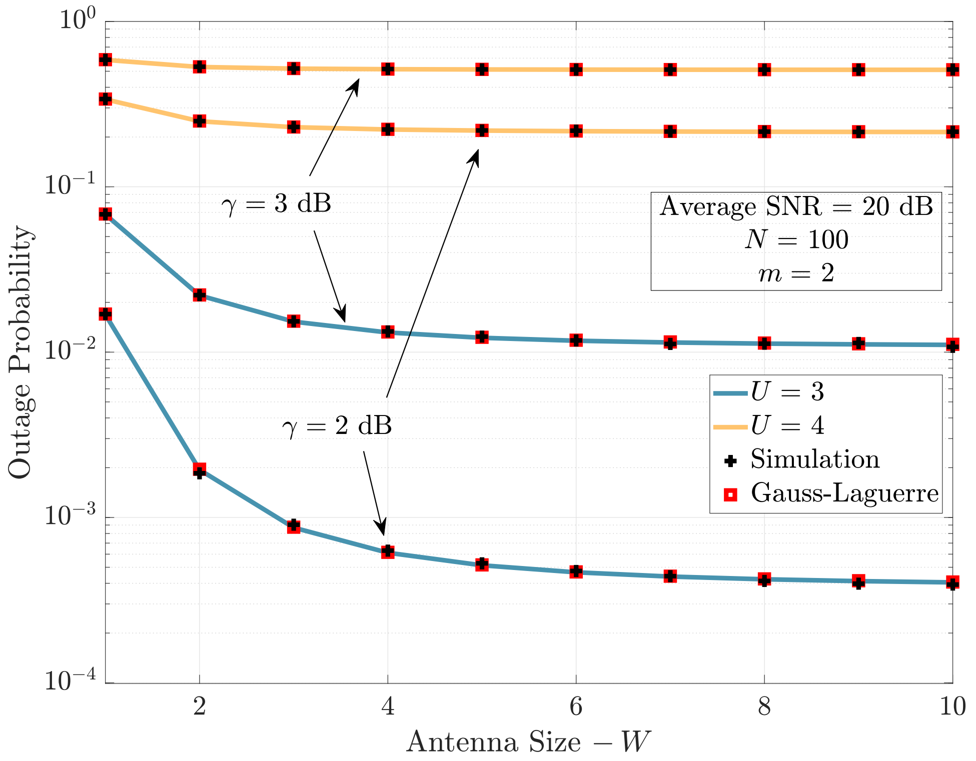

Figure 3.5. SINR-based OP curves as a function of W, considering $\gamma = 2$ dB and $\gamma = 3$ dB, for networks with $U = 3$ and $U = 4$ users, with an average SNR of 20 dB, $N = 100$ and $m = 2$.

towards an irreducible OP as the effect of correlation between the ports is smaller, leading to uncorrelated ports. As γ increases, the system quality requirements become more restrictive, worsening the OP performance. On the other hand, for the same configuration, increasing the number of users U promotes greater levels of interference, thus increasing the OP values.

Figure 3.6 evaluates the dependence of the multiplexing gain on the number of users in the network. The analysis considers a system with UE with different numbers of ports and subject to different fading conditions. In this evaluation, an SIR threshold of $\gamma = 6$ dB and an FA size of $W = 2$ are used. The results show that $\mathcal{G}_m$ tends to decrease as the fading parameter m increases, due to the more deterministic behavior that diminishes the effectiveness of FAMA, as previously discussed. Conversely, the multiplexing gain increases with the number of ports N in the UE, as higher values of N reduce the outage probability experienced by individual users. As discussed in Section 3.4.4, the multiplexing gain $\mathcal{G}_m$ exhibits a concave relationship with respect to the number of users U, meaning there exists an optimal number of users, denoted as $U^\star$, that maximizes the network performance. The maximum multiplexing gains $\mathcal{G}_m(U^\star)$ are highlighted in Figure 3.6, with $U^\star$ being determined by solving the equation expressed in (3.31).

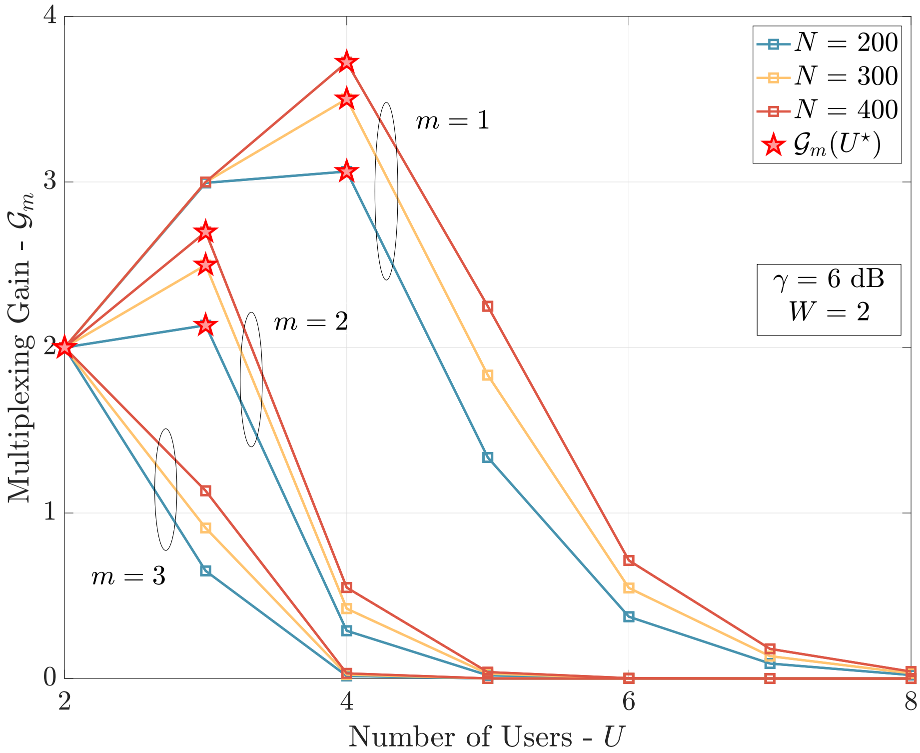

Figure 3.6. Multiplexing gain as a function of the number of users U for different fading conditions and number of ports.

3.6 CONCLUSION

New expressions, considering slow FAMA, based on SIR or SINR, have been derived for the OP over Nakagami-m fading channels. An upper bound for SIR-based OP has been derived. Bounds for the multiplexing gain have been derived. Closed-form and approximate OP expressions have been derived under Nakagami-m and noisy channels using the Gauss-Laguerre quadrature. However, the constant correlation model employed in this chapter exhibits several limitations. For example, increasing the number of ports N does not lead to saturation of OP. To address this issue, a more accurate correlation model is investigated in Chapter 4. Finally, and most importantly, it has been demonstrated that a slow FAMA system operating under harsh environmental conditions, characterized by lower fading intensity parameters, exhibits improved performance in terms of OP and achievable multiplexing gain.

CHAPTER 4

SLOW, FAST, AND OPPORTUNISTIC FAMA WITH SPATIAL BLOCK-CORRELATION MODEL

In this chapter, the performance of s-FAMA, f-FAMA and O-FAMA under Nakagami-m fading channels is studied, considering the spatial block-correlation model [45]. In Chapter 3, the performance of s-FAMA was investigated using the constant correlation model [41]. However, this model does not accurately represent the spatial correlation among ports, a limitation that is addressed by adopting the spatial block-correlation model. As explained in Chapter 2, the spatial block-correlation model accurately characterizes the correlation between ports, as predicted by classical realistic models such as Jakes', while maintaining analytical tractability and simplicity of the constant correlation model presented in [41].

4.1 SYSTEM MODEL

The downlink of an FAMA network is described in Section 3.1. The signal received at the n-th port of an FAS, for the u-th UE, is modeled in (3.1) and repeated below

$$r_n^{(u)} = s_u h_n^{(u,u)} + \sum_{\tilde{u}\neq u}^{U} s_{\tilde{u}} h_n^{(\tilde{u},u)} + \eta_n^{(u)}. \tag{4.1}$$

The channel envelope, assumed Nakagami-m distributed, is expressed, as in (3.3), by

$$|h_n^{(u,u)}| = \sqrt{\sum_{l=1}^{m} |g_{nl}^{(u,u)}|^2}, \tag{4.2}$$

where m is the fading severity, $g_{nl}^{(u,u)}$ is given in (3.4) and $\{g_{nl}^{(u,u)}\}$ is a set of mutually correlated complex Gaussian RVs with zero mean and $\mathbb{E}[|g_{nl}^{(u,u)}|^2] = 2\sigma_u^2$.

4.2 SPATIAL BLOCK-CORRELATION MODEL

The spatial block-correlation model was described in Section 2.4.3. In this section, a brief review is presented. This model approximates the correlation matrix $\boldsymbol{\Sigma}$ by a block-diagonal matrix, denoted by $\widehat{\boldsymbol{\Sigma}}$. In this approach, the N ports of a FA are partitioned into B blocks, where each block has length of L_b ports, with $b \in \{1, \cdots, B\}$ and $\sum_{b=1}^{B} L_b = N$. According to the algorithm in [45], both L_b and $\widehat{\boldsymbol{\Sigma}}$ are determined from the dominant eigenvalues of the reference spatial correlation matrix $\boldsymbol{\Sigma}$ with respect to a threshold ρ_{th}. Consequently, $\widehat{\boldsymbol{\Sigma}}$ is constructed as a block-diagonal matrix consisting of B equi-correlation ($\delta_b = \delta\, \forall b$) sub-matrices of size $L_b \times L_b$. Based on this representation, the OP of the FAMA system can be evaluated as B independent blocks, while approximately retaining the correlation properties. There is no closed-form solution for the best choice of δ and ρ_{th} to optimize $\widehat{\boldsymbol{\Sigma}}$, but in [45] it is suggested to choose $\delta \in (0.95{,}0.99)$ and $\rho_{\text{th}} = 1$.

4.3 SLOW FAMA UNDER NAKAGAMI-m CHANNELS WITH SPATIAL BLOCK-CORRELATION MODEL

4.3.1 Channel Model

Based on Sections 4.1 and 4.2, the channel coefficients are defined as

$$g_{nl}^{(u,u)} = \sigma_u \left(\sqrt{1-\delta}\, x_{nl}^{(u,u)} + \sqrt{\delta}\, \mathrm{x}_{b(n)l}^{(u,u)} \right) + j\sigma_u \left(\sqrt{1-\delta}\, y_{nl}^{(u,u)} + \sqrt{\delta}\, \mathrm{y}_{b(n)l}^{(u,u)} \right), \tag{4.3}$$

in which $\mathrm{x}_{b(n)l}^{(u,u)}$, $x_{1l}^{(u,u)}, \ldots, x_{Nl}^{(u,u)}$ and $\mathrm{y}_{b(n)l}^{(u,u)}$, $y_{1l}^{(u,u)}, \ldots, y_{Nl}^{(u,u)}$, with $l \in \{1, \ldots, m\}$, are independent Gaussian RVs with zero mean and unit variance and δ is the common power correlation coefficient between any two ports in a block. It is assumed that $\sigma_u = \sigma$, $\forall \tilde{u}$.

For RV and port separations per block, considering $N = \sum_{b=1}^{B} L_b$, the following notation is used. The RVs $\mathrm{x}_{b(n)l}^{(u,u)}$ and $\mathrm{y}_{b(n)l}^{(u,u)}$ are referenced to the block index $b(n)$, which is defined as $b(n) = 1$ for port indexes $n = 1, \ldots, L_1$, $b(n) = 2$ for port indexes $n = 1 + L_1, \ldots, L_1 + L_2$ and so on, until $b(n) = B$ for port indexes $n = 1 + L_1 + \cdots + L_{(B-1)}, \ldots, N$.

Note that the expressions (4.2) and (4.3) are also suitable for interfering users. In this case, the distribution parameters are indicated by $m_{\tilde{u}}$, with $l \in \{1, \ldots, m_{\tilde{u}}\}$, $\sigma_{\tilde{u}} = \sigma\ \forall u$, and the superscripts are denoted by $(\tilde{u}, u)$.

4.3.2 SIR Model

Assuming an interference-dominated scenario, where noise can be neglected in (4.1), an UE in a s-FAMA network selects the port where the SIR is maximized, such as

$$\mathrm{SIR} = \max_n \frac{\sigma_s^2 |h_n^{(u,u)}|^2}{\sigma_s^2 \sum_{\tilde{u}\neq u}^{U} |h_n^{(\tilde{u},u)}|^2} = \max_n \frac{\mathbb{X}_n}{\mathbb{Y}_n}, \tag{4.4}$$

in which

$$\mathbb{X}_n = \sum_{l=1}^{m} \left(x_{nl}^{(u,u)} + \sqrt{\frac{\delta}{1-\delta}}\, \mathrm{x}_{b(n)l}^{(u,u)} \right)^2 + \left(y_{nl}^{(u,u)} + \sqrt{\frac{\delta}{1-\delta}}\, \mathrm{y}_{b(n)l}^{(u,u)} \right)^2 \tag{4.5}$$

and

$$\mathbb{Y}_n = \sum_{\substack{\tilde{u}=1\\ \tilde{u}\neq u}}^{U} \sum_{l=1}^{m_{\tilde{u}}} \left(x_{nl}^{(\tilde{u},u)} + \sqrt{\frac{\delta}{1-\delta}}\, \mathrm{x}_{b(n)l}^{(\tilde{u},u)} \right)^2 + \left(y_{nl}^{(\tilde{u},u)} + \sqrt{\frac{\delta}{1-\delta}}\, \mathrm{y}_{b(n)l}^{(\tilde{u},u)} \right)^2. \tag{4.6}$$

4.3.3 Outage Probability Analysis

4.3.3.1 Exact Expression

As demonstrated in Appendix C, the OP, considering that the blocks are independent, is given by

$$P_{\mathrm{out}} = \mathrm{Prob}(\mathrm{SIR} < \gamma) = \prod_{b=1}^{B} P_{\mathrm{out};b}(\gamma), \tag{4.7}$$

in which $P_{\mathrm{out};b}(\gamma)$ is the OP of the b-th block and γ is the SIR threshold. It is noteworthy that the total OP, obtained as the product of the OP values for each block, directly follows from the approximation adopted in the block-correlation model. Replacing (3.25) into (4.7), the SIR-based OP results in

$$P_{\mathrm{out}} = \prod_{b=1}^{B} \int_0^\infty \int_0^\infty \frac{r_b^{m-1} \widetilde{r}_b^{\widetilde{U}-1} e^{-\frac{r_b + \widetilde{r}_b}{2}}}{2^{m+\widetilde{U}} \Gamma(m) \Gamma(\widetilde{U})} \left[G(\gamma; r_b, \widetilde{r}_b) \right]^{L_b} \mathrm{d}r_b \, \mathrm{d}\widetilde{r}_b, \tag{4.8}$$

where $G(\gamma; r_b, \widetilde{r}_b)$ is given by

$$\begin{aligned} G(\gamma; r_b, \widetilde{r}_b) = {} & \mathrm{Q}_{\widetilde{U}} \left(\sqrt{\frac{\delta\, \gamma\, \widetilde{r}_b}{(1-\delta)(\gamma+1)}}, \sqrt{\frac{\delta\, r_b}{(1-\delta)(\gamma+1)}} \right) - \left(\frac{1}{\gamma+1} \right)^{m+\widetilde{U}-1} \left(\frac{r_b}{\gamma\, \widetilde{r}_b} \right)^{\frac{1-m}{2}} \\ & \times \exp\left(-\frac{\delta}{2(1-\delta)} \frac{\gamma \widetilde{r}_b + r_b}{\gamma+1} \right) \sum_{k=0}^{m+\widetilde{U}-2} \sum_{j=0}^{m+\widetilde{U}-k-2} \frac{(m+\widetilde{U}-(j+k)-1)_j}{j!} \\ & \times \left(\frac{r_b}{\widetilde{r}_b} \right)^{\frac{j+k}{2}} (\gamma+1)^k \gamma^{\frac{j-k}{2}} \mathrm{I}_{1-m+j+k} \left(\frac{\delta \sqrt{\gamma\, r_b\, \widetilde{r}_b}}{(1-\delta)(\gamma+1)} \right). \end{aligned} \tag{4.9}$$

4.3.3.2 Approximation

Applying the generalized Gauss-Laguerre quadrature (GLQ) [119]

$$\int_0^\infty x^\beta e^{-x} f(x)\mathrm{d}x \approx \sum_{i=1}^{n_I} w_i f(x_i) \tag{4.10}$$

in (4.8), a simple approximation for the SIR-based OP is obtained

$$P_{\text{out}} \approx \prod_{b=1}^{B} \frac{1}{\Gamma(m)\Gamma(\widetilde{U})} \sum_{i=1}^{n_I}\sum_{j=1}^{n_J} w_i w_j \left[G(\gamma; 2\,x_i, 2\,x_j)\right]^{L_b}, \tag{4.11}$$

where x_i, for $i \in \{1,\ldots,n_I\}$, and x_j, for $j \in \{1,\ldots,n_J\}$, are, respectively, the roots of the generalized Laguerre polynomials $L_{n_I}^{m-1}(x_i)$ and $L_{n_J}^{\widetilde{U}-1}(x_j)$, with weights

$$w_i = \frac{\Gamma(n_I+m)x_i}{n_I!(n_I+1)^2[L_{n_I+1}^{m-1}(x_i)]^2} \tag{4.12}$$

and

$$w_j = \frac{\Gamma(n_J+\widetilde{U})x_j}{n_J!(n_J+1)^2[L_{n_J+1}^{\widetilde{U}-1}(x_j)]^2}. \tag{4.13}$$

Employing approximately 30 roots typically provides a favorable compromise between numerical accuracy and computational efficiency in the OP calculation.

4.3.3.3 Upper Bound

The upper bound for the OP can be derived using the fact that for $\delta \to 1$, the exponential in (5.21) tends to zero, and then the OP is approximated only by the term $\mathrm{Q}_{\tilde{U}}(\cdot)$. Furthermore, for very large N that results in large L_b for most dominant eigenvalues, it follows that $[\mathrm{Q}_{\tilde{U}}(\cdot)]^{L_p}$ tends to a Heaviside step function, shift by a threshold $f(\widetilde{r}_b)$. Thus, $[G(\gamma; r_b, \widetilde{r}_b)]^{L_b} = 1$ for $r_b < f(\widetilde{r}_b)$ and $[G(\gamma; r_b, \widetilde{r}_b)]^{L_b} = 0$ for $r_b > f(\widetilde{r}_b)$, so (4.8) is approximated by

$$P_{\text{out}} \approx \prod_{b=1}^{B} \int_0^\infty \frac{\widetilde{r}_b^{\widetilde{U}-1} e^{-\widetilde{r}_b/2}}{2^{m+\widetilde{U}}\Gamma(m)\Gamma(\widetilde{U})} \int_0^{f(\widetilde{r}_b)} r^{m-1} e^{-\frac{r_b}{2}} \mathrm{d}r_b\, \mathrm{d}\widetilde{r}_b. \tag{4.14}$$

Setting the threshold as $f(\widetilde{r}_b) = \gamma\, \widetilde{r}_b$ and using [120, Eqs. (3.351-1) and (3.351-3)], the integrals in (4.14) are solved, as detailed in Appendix D, which results in the upper bound

$$P_{\text{out}} < \left(1 - \sum_{i=0}^{m-1} \frac{\gamma^i (\widetilde{U})_i}{i!(\gamma+1)^{\widetilde{U}+i}}\right)^B. \tag{4.15}$$

It can be shown that the right rand side of (4.15) is also the OP of B independent antennas under Nakagami-m channels.

4.3.3.4 Multiplexing Gain

The multiplexing gain of the system is given by

$$\mathcal{G}_m = U\,(1 - P_{\rm out}), \tag{4.16}$$

which is the same as in (3.29).

4.4 FAST FAMA UNDER NAKAGAMI-m CHANNELS WITH SPATIAL BLOCK-CORRELATION MODEL

As discussed in Section 4.4, f-FAMA requires full CSI, rapid port switching and instantaneous SINR estimation, which pose significant challenges. Consequently, in view of these practical limitations, the f-FAMA framework, examined in this section, should be regarded as a theoretical performance bound, primarily intended for comparison with s-FAMA.

4.4.1 Channel Model

For f-FAMA, the total interference in the received signal is treated as a single RV $\widetilde{h}_n^{(u)} = \sum_{\substack{\tilde{u}=1\\ \tilde{u}\neq u}}^{U} s_{\tilde{u}} h_n^{(\tilde{u},u)}$. Considering the seminal work of Nakagami [46], the sum of the complex Nakagami-m interference RVs is approximated by another Nakagami-m RV, with average power $\widetilde{\Omega}$ and fading parameter $\widetilde{m}$ given by [46, Eq. (96)]

$$\widetilde{\Omega} = \sum_{\substack{\tilde{u}=1\\ \tilde{u}\neq u}}^{U} \Omega_{\tilde{u}} \sigma_s^2 = 2\sigma^2\sigma_s^2 \widetilde{U} \tag{4.17}$$

and

$$\widetilde{m} = \frac{\left(\sum_{\substack{\tilde{u}=1\\ \tilde{u}\neq u}}^{U} m_{\tilde{u}}\right)^2}{\sum_{\substack{\tilde{u}=1\\ \tilde{u}\neq u}}^{U} m_{\tilde{u}} + 2\sum_{\substack{i\neq\tilde{u}\\ \tilde{u}\neq u}}^{U} m_{\tilde{u}}\, m_i}, \tag{4.18}$$

in which $\Omega_{\tilde{u}} = \mathbb{E}[|h_n^{(\tilde{u},u)}|^2] = 2\,m_{\tilde{u}}\,\sigma^2$ and $\mathbb{E}[s_{\tilde{u}}^2] = \sigma_s^2$, $\forall\tilde{u}$. Therefore, the total interference power is modeled as $|\widetilde{h}_n^{(u)}|^2 = |\sum_{\substack{\tilde{u}=1\\ \tilde{u}\neq u}}^{U} s_{\tilde{u}} h_n^{(\tilde{u},u)}|^2 \approx \sum_{l=1}^{\widetilde{m}} |\widetilde{g}_{nl}^{(u)}|^2$ with $\widetilde{g}_{nl}^{(u)}$ being expressed similarly to (4.3), with Gaussian components denoted as $\widetilde{\mathrm{x}}_{b(n)l}^{(u)}, \widetilde{x}_{1l}^{(u)}, \ldots, \widetilde{x}_{Nl}^{(u)}$ and $\widetilde{\mathrm{y}}_{b(n)l}^{(u)}, \widetilde{y}_{1l}^{(u)}, \ldots, \widetilde{y}_{Nl}^{(u)}$, thus $\mathbb{E}[|\widetilde{g}_{nl}^{(u)}|^2] = 2\widetilde{\sigma}$ and $\widetilde{\Omega} = \mathbb{E}[|\widetilde{h}_n^{(u)}|^2] = 2\widetilde{m}\widetilde{\sigma}^2$.

4.4.2 SIR Model

The SIR for f-FAMA is given by

$$\mathrm{SIR} = \max_n \frac{\sigma_s^2 |h_n^{(u,u)}|^2}{|\widetilde{h}_n^{(u,u)}|^2} = \max_n \frac{\mathbb{X}_n}{\widehat{U}\mathbb{Z}_n}, \tag{4.19}$$

in which

$$\widehat{U} = \frac{\widetilde{U}}{\widetilde{m}} = \frac{\widetilde{\sigma}^2}{\sigma^2 \sigma_s^2}, \tag{4.20}$$

$\mathbb{X}_n$ is given by (4.5) and $\mathbb{Z}_n$ is defined as

$$\mathbb{Z}_n = \sum_{l=1}^{\widetilde{m}} \left(\widetilde{x}_{nl}^{(u)} + \sqrt{\frac{\delta}{1-\delta}} \widetilde{\mathrm{x}}_{b(n)l}^{(u)} \right)^2 + \left(\widetilde{y}_{nl}^{(u)} + \sqrt{\frac{\delta}{1-\delta}} \widetilde{\mathrm{y}}_{b(n)l}^{(u)} \right)^2. \tag{4.21}$$

Remark 1: Comparing the SIR for f-FAMA in (4.19) and the SIR for s-FAMA in (4.4), note that the expressions are similar, except for the constant $\widehat{U}$ and the upper limits of the sum of $\mathbb{Y}_k$ and $\mathbb{Z}_k$. As a consequence, the SIR-based OP for f-FAMA can be obtained from the SIR-based OP for s-FAMA in (4.8) substituting γ by $\widehat{U}\gamma$ and $\widetilde{U}$ by $\widetilde{m}$.

Remark 2: The multiplexing gain for f-FAMA is calculated as (4.16), but considering the OP particularities of f-FAMA.

4.5 OPPORTUNISTIC FAMA UNDER NAKAGAMI-m CHANNELS WITH SPATIAL BLOCK-CORRELATION MODEL

As described in Section 2.6.4, in O-FAMA the best U users are selected from a pool of $M(\geq U)$ users to maximize the network capacity. In this section, O-FAMA is studied operating in fast or slow modes. In FAMA, the BS does not perform pre-processing, and the user's OP is independent of the others. Consequently, in O-FAMA, the BS can identify the top users by sequentially activating and deactivating them until the best set is found. It is assumed that the strongest U UEs are selected as an ideal condition. In [109], it is shown that it is possible to select the best users and FAS ports to reach a network sum rate close to the ideal based on a reinforcement learning approach, which makes O-FAMA an interesting option for multiple access.

Based on the selection of the U users with better channel conditions from a pool M users, the multiplexing gain of an O-FAMA network is given by [39, Eq. (21-a)]

$$\mathcal{G}_m = \sum_{u=M-U+1}^{M} \mathcal{I}_{1-P_{\mathrm{out}}}(M-u+1,u), \tag{4.22}$$

where $\mathcal{I}_x(a,b)$ is the regularized incomplete beta function. Moreover, $\mathcal{G}_m$ can be accurately approximated by [39, Eq. (46)]

$$\mathcal{G}_m \approx \min\{U, M(1-P_{\mathrm{out}})\}. \tag{4.23}$$

The P_{out} used in (4.22) and (4.23), depends on whether O-FAMA is operated in the s-FAMA or f-FAMA modes.

The number of UEs in the scheduling selection pool, M, determines the degree of multiuser diversity that can be achieved. As M increases, the overall performance improves. The number of selected UEs, U, for communication at a given time denotes how many users are chosen to share the same time-frequency resource unit in each scheduling interval. As U increases, each selected UE experiences more interference; however, if the fluid antenna at each UE is sufficiently capable of mitigating this interference, the overall network capacity can potentially be higher. It can be optimized by balancing the interference experienced by each UE against the overall network capacity (or multiplexing gain).

4.6 NUMERICAL RESULTS

This section presents the numerical results for the performance metrics developed in this work. Monte Carlo simulations are also employed to validate the derived analytical expressions [1]. The Gauss–Laguerre quadrature approximations are evaluated with $n_I = n_J = 50$ roots. In addition, the block-correlation analysis is based on a reference correlation matrix derived from the Jakes' model. Our results compare the exact OP with the analytical approximation obtained via the Gauss-Laguerre quadrature and Monte Carlo simulations. All curves exhibit strong overlap, validating our analysis.

Before going into the numerical analysis, it is appropriate to discuss the parameters δ and ρ_{th} used for the spatial block-correlation model. As explained in [45], there is no closed form solution for the choice of δ and ρ_{th}. Ideally, δ should be as close to 1 as possible, but [45]

[1]The codes used are available at https://github.com/deMouraPaulo/FAMA

reported that, in practice, values of δ too close to 1 are detrimental for the analysis of FAMA and a good rule-of-thumb is to choose $\delta \in (0.95, 0.99)$, therefore the average of this range was chosen, that is, $\delta = 0.97$. For the choice of ρ_{th}, [45] reported that the eigenvalues of $\boldsymbol{\Sigma}$ decay rapidly and that $\rho_{\text{th}} = 1$ usually produces accurate results. It is adopted $\rho_{\text{th}} = N/100$ in the following numerical analysis. For the cases in which $N = 100$, then $\rho_{\text{th}} = 1$. For the analysis in which N varies in the range $N \in [10{,}200]$, the formula $\rho_{\text{th}} = N/100$ chooses ρ_{th} properly.

Figure 4.1 shows the OP curves as a function of the number of ports N for both s-FAMA and f-FAMA systems, considering different values of the normalized antenna length W. The system parameters are fixed at $U = 5$ users, $m = 2$ and $\gamma = -3$ dB, $\delta = 0.97$ and $\rho_{\text{th}} = N/100$. The Monte Carlo simulations were plotted for the SIR expression and for Jakes' correlation matrix. This result highlights the impact of different correlation models on OP, comparing spatial block-correlation with constant correlation models. The results indicate that, for equivalent systems, FAMA achieves considerably better performance in fast mode, owing to port selection optimization at the symbol time scale. Increasing the number of ports also improves performance by reducing the OP. However, this gain is significantly diminished under a more realistic block-correlation model. The constant correlation model reproduces a non-realistic scenario with rapid signal fluctuations across ports, offering more opportunities for SIR maximization and thus leading to an overestimation of performance. Conversely, with the block-correlation model, spatial fluctuations are slower, reflecting the practical characteristics of spatial correlation, where fewer opportunities for SIR maximization occurs and consequently limiting the OP improvement achievable with larger N. The block-correlation approach yields outage probabilities aligned with those obtained using the Jakes' model, especially for larger values of W. Finally, it is noted that for both the FAMA systems and the adopted correlation models, the OP improves with an increase of W as a larger W reduces the spatial correlation between ports.

Figure 4.2 presents the OP curves as a function of the SIR threshold for s-FAMA and f-FAMA under different values of the fading parameter m and the number of users U. The remaining parameters are fixed at $N = 100$, $W = 1$, $\delta = 0.97$ and $\rho_{\text{th}} = N/100$ and, as a consequence of [45, Algorithm 1], $B = 4$ and $L_b = \{40, 39, 19, 2\}$. As a benchmark, the Rayleigh case ($m = 1$) is included. As expected, the OP increases with higher SIR threshold

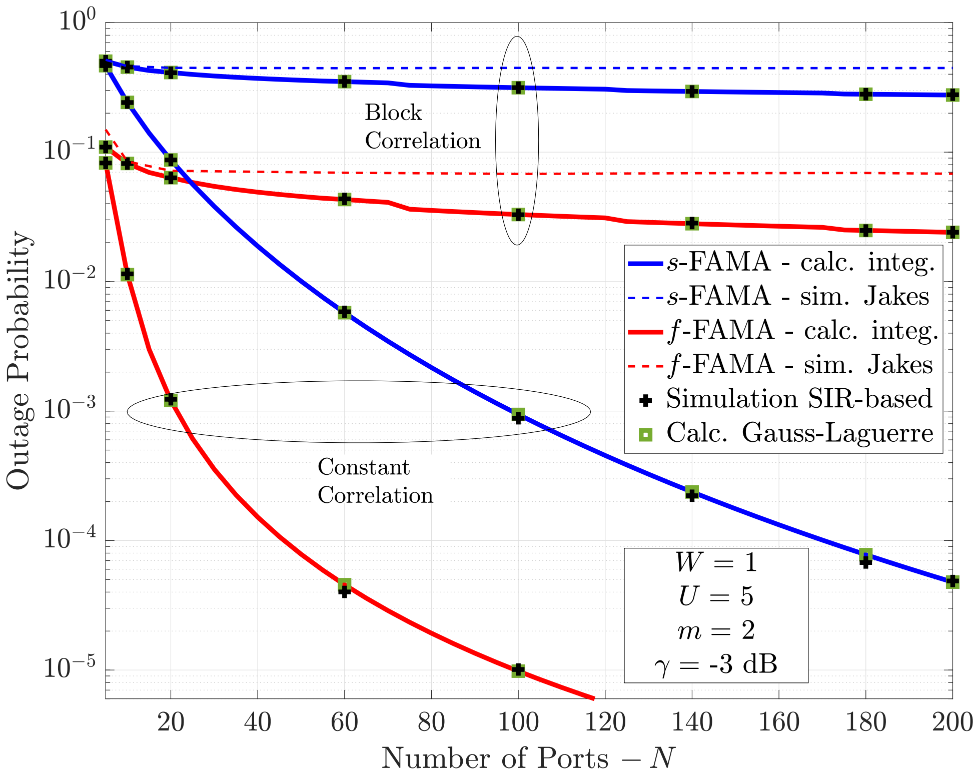

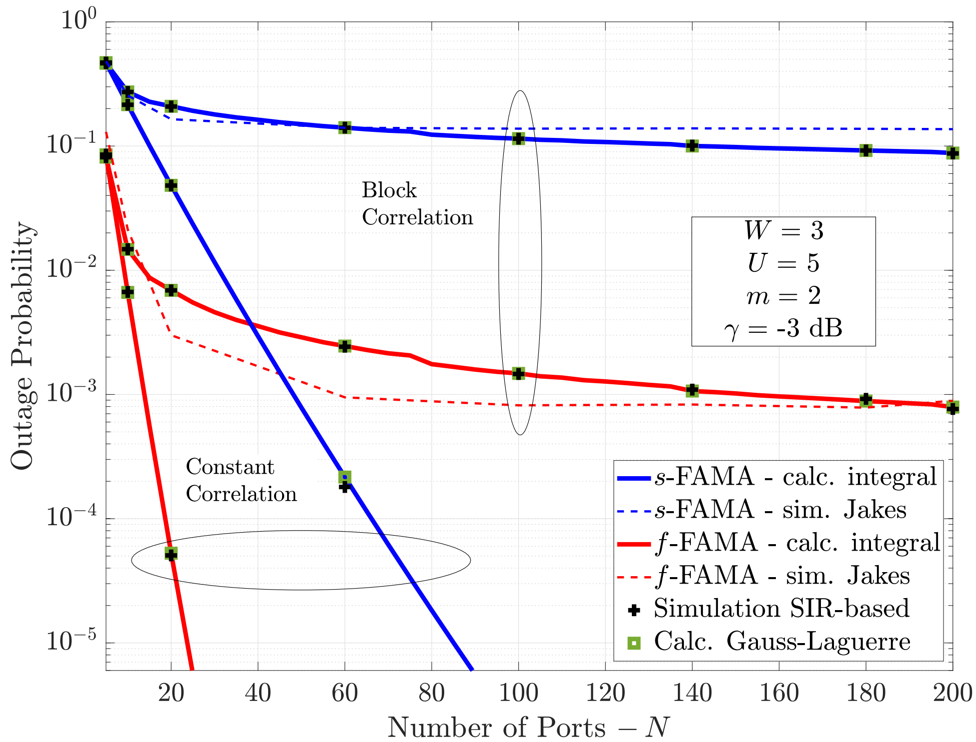

Figure 4.1. OP curves for s-FAMA and f-FAMA systems, for $W = 1$ and $W = 3$, considering constant correlation and spatial block-correlation models, for $U = 5$, $m = 2$, and $\gamma = -3$ dB.

requirements. Moreover, f-FAMA consistently outperforms s-FAMA under the same system configuration. The impact of m differs across the evaluated cases. For s-FAMA, under low SIR threshold requirements, the Rayleigh case ($m = 1$) represents the worst performance. However, at higher SIR thresholds, the case with $m = 3$ becomes the worst. For f-FAMA, the OP exhibits a general improvement as m increases. Furthermore, U worsens the OP since higher interference leads to higher outage levels.

Figure 4.3 depicts the multiplexing gain curves as a function of the number of users for s-FAMA, f-FAMA, and O-FAMA (in slow and fast modes). The system parameters are set to $N = 100$ ports, $m = 2$, $\gamma = -3$ dB, $W = 1$, $\delta = 0.97$ and $\rho_{\text{th}} = N/100$ and, as a consequence of [45, Algorithm 1], $B = 4$ and $L_b = \{40, 39, 19, 2\}$. The performance of O-FAMA is evaluated under different user pool sizes M. As observed, increasing M while keeping U fixed enhances the multiplexing gain, indicating that a larger number of users can be served without experiencing outage. Conversely, for FAMA in slow mode, an inflection point emerges, beyond which further increases in network size reduce the multiplexing gain. In contrast, in fast mode this effect does not occur, and the multiplexing gain exhibits a consistently increasing trend with network scaling. This notable performance advantage is attributed to the ability to maximize the SIR at symbol time, thereby offering more optimization opportunities compared to the slow mode.

4.7 CONCLUSION

This chapter studied slow, fast, and opportunistic FAMA under Nakagami-m fading channels, considering the spatial block-correlation model, where OP expressions and bounds for slow and fast FAMA were derived and applied to the study of O-FAMA. Multiplexing gain results for O-FAMA over fast and slow FAMA were obtained. The numerical and simulation results confirmed the accuracy of the proposed analytical framework. The analysis of FAMA was extended to more general fading and correlation conditions, providing practical insights.

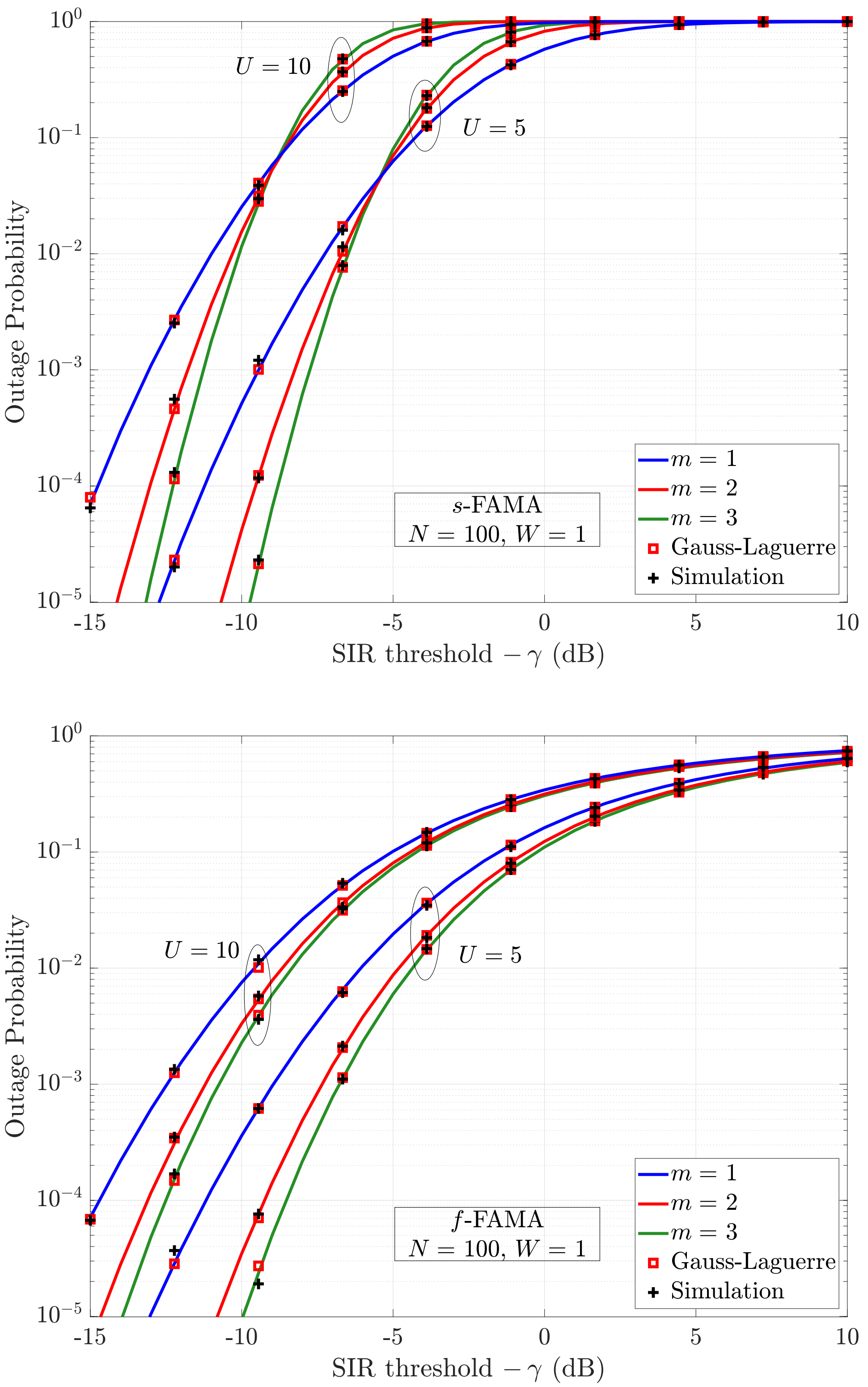

Figure 4.2. OP curves as a function of the SIR threshold for s-FAMA and f-FAMA considering different values of m and U, with $N = 100$ and $W = 1$.

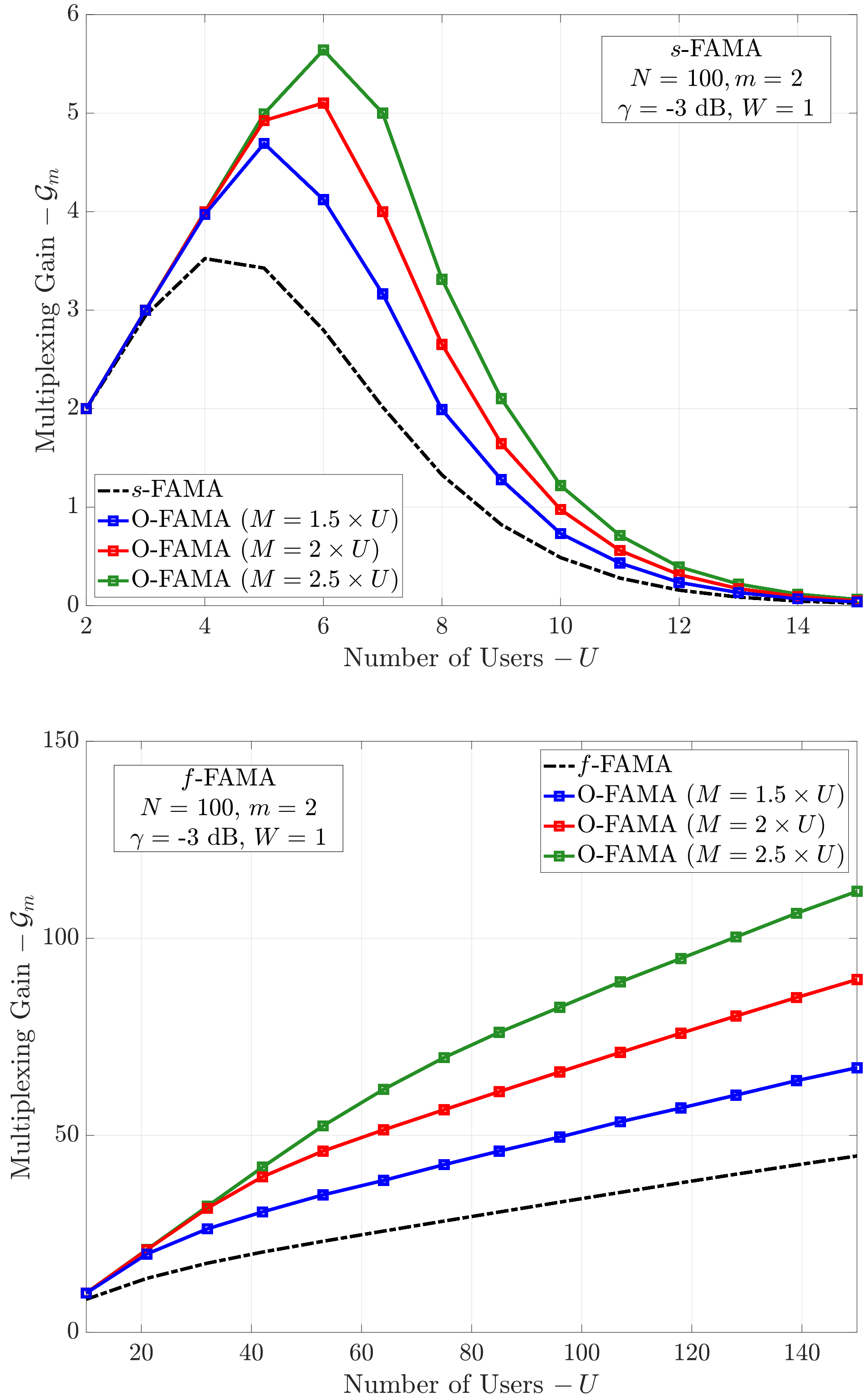

Figure 4.3. Multiplexing gain curves as a function of the number of users U for s-FAMA, f-FAMA and O-FAMA under different settings of M, considering $N = 100$, $W = 1$, $m = 2$, and $\gamma = -3$ dB.

CHAPTER 5

MRT-FAMA NETWORKS

The performance of an MRT-FAMA network under Nakagami-m fading channels is studied in this chapter. For ease of exposition, the constant correlation model is used, but is explained how to obtain the expressions using the spatial block-correlation model.

As described in Chapter 2, a cell-free FAMA network is made up of BSs (or cluster of APs) with multiple antennas that employ MRT precoding to beamforming toward their respective UEs. The nomenclature “cell-free FAMA” was introduced in [88] to describe the mentioned network setup; however, it does not represent the traditional setup of cell-free massive MIMO [121, 122], therefore the nomenclature “MRT-FAMA network” is adopted in this chapter. In traditional cell-free network, all BSs are required to obtain the CSI of all users to manage inter-user interference with techniques such as zero-forcing. However, the stringent CSI acquisition demands, combined with the requirement for intensive coordination and information exchange among multiple BSs, place substantial limitations on the overall scalability of the system, and these limitations become particularly pronounced in large-scale network deployments.

The MRT precoding is more scalable than other methods such as zero-forcing in terms of the CSI requirement at the BS, which alleviates its burden. It is further assumed that the BS has perfect CSI and applies MRT precoding only toward the intended user, disregarding the interference it generates for other users and relying on the FAS at each user to handle the interference.

This chapter investigates a multi-cell framework in which the “cell” concept is used solely to define the coverage region of each BS and its user association. All users operate on the same time–frequency physical channel, and both large-scale and small-scale fading effects are taken into account. Each BS serves a single user, and that user is equipped with a FAS employing FAMA to mitigate inter-user interference. Following the nomenclature of Chapter 2, this configuration corresponds to an Rx-MISO-FAS model.

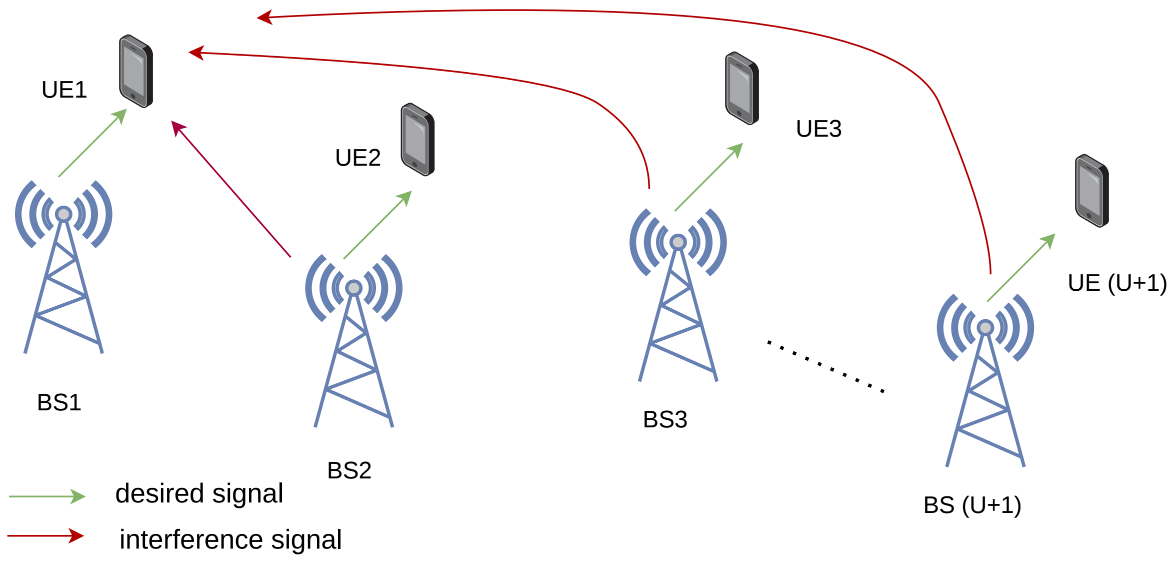

Figure 5.1. An MRT-FAMA network.

5.1 SYSTEM MODEL

Consider a downlink scenario of a network architecture operating under Nakagami-m fading channels, comprising $U+1$ BSs, each tasked with serving a distinct area centered at its respective location, as shown in Figure 5.1. Within the framework of a TDMA system, each BS, equipped with K fixed-position antennas (FPAs), serves a single UE located within its designated coverage area during any given time slot, while all BSs operate over the same time-frequency physical channel. Consequently, each user experiences interference originating from the remaining U BSs. Moreover, each BS is assumed to have CSI to perform MRT precoding, which co-phases the signals to serve its associated user, which is equipped with an 1D-FAS. This system was called MRT-FAMA network. In this chapter, U denotes the number of interfering BSs, and consequently the network comprises a total of $U+1$ BSs.

The signal received at the n-th port of an FAS in an MRT-FAMA network, for a given user, is modeled as

$$r_n = s\,\tilde{h}_n + \sum_{i=1}^{U} s_i \tilde{h}_n^{(i)} + \eta_n, \tag{5.1}$$

where s represents the symbol transmitted to the intended user, $\tilde{h}_n$ denotes the overall channel observed at the n-th port of the FAS user for the desired signal, and $\tilde{h}_n^{(i)}$ denotes the interference channel of the i-th BS, transmitting the signal s_i, which acts as interference at the n-th port of the FAS user. The average power of the transmitted symbol is $\sigma_s^2 = \mathbb{E}[|s_i|^2]$, $\forall i$, and $\eta_n \sim \mathcal{CN}(0, \sigma_\eta^2)$ represents the AWGN.

As BSs perform MRT precoding and taking into account the distance d_0 from the BS to the target user, the overall channel from BS to the n-th port of the target user is written as [88]

$$\tilde{h}_n = \sqrt{d_0^{-\alpha} \sum_{k=1}^{K} |h_{kn}|^2}, \tag{5.2}$$

where α is the path loss exponent, and h_{kn} is the small-scale Nakagami-m fading channel from the k-th fixed antenna of the BS to the n-th port of the target user. If the fading severity m is an integer, its magnitude can be written as

$$|h_{kn}| = \sqrt{\sum_{l=1}^{m} |g_{knl}|^2}, \tag{5.3}$$

where g_{knl} is a complex Gaussian RV, with zero mean and variance $2\sigma^2$ defined as

$$g_{knl} = \sigma \left(\sqrt{1-\delta}\, x_{knl} + \sqrt{\delta}\, x_{0knl} \right) + j\, \sigma \left(\sqrt{1-\delta}\, y_{knl} + \sqrt{\delta}\, y_{0knl} \right), \tag{5.4}$$

where x_{0knl}, x_{knl}, y_{0knl}, and y_{knl}, with $l \in \{1, \ldots, m\}, k \in \{1, \ldots, K\}, n \in \{1, \ldots, N\}$, are i.i.d. RVs with $\mathcal{N}(0,1)$, and δ is a common power correlation coefficient modeled as in (2.9).

The interference channel on the n-th port of the target user with MRT precoding can be modeled as [88]

$$\tilde{h}_n^{(i)} = d_i^{-\alpha/2}\, h_n^{(i)}, \tag{5.5}$$

where d_i is the distance between the i-th interfering BS and the target UE, and $h_n^{(i)}$ is the small-scale Nakagami-m fading channel from the i-th BS to the n-th FAS port of the target UE, characterized similarly to (5.3) and (5.4), with the same σ and m, but with Gaussian RVs named $g_{knl}^{(i)}$ $x_{0nl}^{(i)}$, $x_{nl}^{(i)}$, $y_{0nl}^{(i)}$, and $y_{nl}^{(i)}$.

5.2 MRT SLOW FAMA UNDER NAKAGAMI-m FADING CHANNELS

5.2.1 SIR Model

If noise is ignored in (5.1), in a MRT-s-FAMA network, an FAS enabled-UE selects the port where the SIR is maximized, such as

$$\mathrm{SIR} = \max_n \frac{\sigma_s^2 |\tilde{h}_n|^2}{\sigma_s^2 \sum_{i=1}^{U} |\tilde{h}_n^{(i)}|^2} = \max_n \frac{|\tilde{h}_n|^2}{|\tilde{h}_n^{(s)}|^2}, \tag{5.6}$$

in which

$$|\tilde{h}_n|^2 = d_0^{-\alpha} \sigma^2 (1-\delta) X_n, \tag{5.7}$$

with

$$X_n = \sum_{k=1}^{K} \sum_{l=1}^{m} (x_{knl} + \sqrt{\tfrac{\delta}{1-\delta}}\, x_{0kl})^2 + (y_{knl} + \sqrt{\tfrac{\delta}{1-\delta}}\, y_{0kl})^2, \tag{5.8}$$

and the total interference channel is

$$|\tilde{h}_n^{(s)}|^2 = \sum_{i=1}^{U} |\tilde{h}_n^{(i)}|^2 = \sum_{i=1}^{U} d_i^{-\alpha} |h_n^{(i)}|^2. \tag{5.9}$$

5.2.2 SIR-based Outage Probability - General Case

Note in (5.9) that if the distances d_i from interference BSs are the same, then $|\tilde{h}_n^{(s)}|^2$ is Chi-square distributed with $2mU$ DoFs. In this case, OP can be obtained following the steps presented in Chapter 3. However, the general case is considered before narrowing the focus to this specific scenario.

Theorem 5.1 *The SIR-based OP for an MRT-s-FAMA network under Nakagami-m fading channels is given by*

$$P_{\mathrm{out}} = \int_0^\infty \int_0^\infty \frac{r^{mK-1} \tilde{r}^{m_s-1} e^{-\frac{r+\tilde{r}}{2}}}{2^{mK+m_s} \Gamma(mK) \Gamma(m_s)} \prod_{n=1}^{N} \left[1 - \frac{1}{2} \int_0^\infty H\left(\tfrac{d_0^\alpha \gamma}{2\sigma^2 (m_s/\Omega_s)}, m_s; y_n, r, \tilde{r} \right) \mathrm{d}y_n \right] \mathrm{d}r\, \mathrm{d}\tilde{r}, \tag{5.10}$$

where $H(\gamma, m_s;\, y_n, r, \tilde{r})$ is given by

$$H(\gamma, m_s; y_n, r, \tilde{r}) = \mathrm{Q}_{mK}\left(\sqrt{\frac{\delta\, r}{1-\delta}}, \sqrt{\gamma\, y_n} \right) \left(\frac{y_n}{\frac{\delta}{(1-\delta)} \tilde{r}} \right)^{\frac{m_s-1}{2}} e^{-\frac{y_n + \frac{\delta}{1-\delta}\tilde{r}}{2}}\, \mathrm{I}_{m_s-1}\left(\sqrt{\frac{\delta\, y_n\, \tilde{r}}{1-\delta}} \right). \tag{5.11}$$

And Ω_s and m_s are the parameters (not restricted to integer values) of the Nakagami-m distributed RV $|\tilde{h}_n^{(s)}|$, given, respectively, by

$$\Omega_s = 2\, m\, \sigma^2 \sum_{i=1}^{U} d_i^{-\alpha}, \tag{5.12}$$

and

$$m_s = \frac{m(\sum_i^U d_i^{-\alpha})^2}{\sum_i^U d_i^{-2\alpha}}. \tag{5.13}$$

Proof: See Appendix E. ∎

Corolary 5.1 *An approximation for the SIR-based OP for an MRT-s-FAMA network under Nakagami-m fading channels is given by*

$$P_{\text{out}} \approx \frac{1}{\Gamma(mK)\Gamma(m_s)} \sum_{i=1}^{n_I} \sum_{j=1}^{n_J} w_i w_j \left[1 - \sum_{l=1}^{n_L} w_l H\left(\tfrac{d_0^\alpha\, \gamma}{2\,\sigma^2 (m_s/\Omega_s)}, m_s; 2x_l, 2x_i, 2x_j\right)\right]^N, \tag{5.14}$$

where x_i, for $i \in \{1, \ldots, n_I\}$, x_j, for $j \in \{1, \ldots, n_J\}$ and x_l, for $l \in \{1, \ldots, n_L\}$ are, respectively, the roots of generalized Laguerre polynomials $L_{n_I}^{mK-1}(x_i)$, $L_{n_J}^{m_s-1}(x_j)$ and $L_{n_L}(x_l)$, with weights

$$w_i = \frac{\Gamma(n_I + mK)x_l}{n_I!(n_I+1)^2[L_{n_I+1}^{mK-1}(x_i)]^2}, \tag{5.15}$$

$$w_j = \frac{\Gamma(n_J + m_s)x_j}{n_J!(n_J+1)^2[L_{n_J+1}^{m_s-1}(x_j)]^2}, \tag{5.16}$$

and

$$w_l = \frac{x_l}{(n_L+1)[L_{n_L+1}(x_l)]^2}. \tag{5.17}$$

Proof: The weights of the generalized Gauss-Laguerre quadrature (GLQ) are presented in [119]. Applying the generalized GLQ in (5.10) and (5.11), then (5.14) is obtained. ∎

Employing approximately 30 roots typically provides a favorable compromise between numerical accuracy and computational efficiency in the calculation of OP.

5.2.3 SIR-based Outage Probability - Special Case

In this section, we consider the case where the distances d_i from interference BSs are the same.

Corolary 5.2 *The SIR-based OP for an MRT-s-FAMA network under Nakagami-m fading channels for $d_i = d\,\forall i$, is given by*

$$P_{\text{out}} = \int_0^\infty \int_0^\infty \frac{r^{mK-1}\tilde{r}^{mU-1}e^{-\frac{r+\tilde{r}}{2}}}{2^{mK+mU}\Gamma(mK)\Gamma(mU)} \prod_{n=1}^{N}\left[1-\frac{1}{2}\int_0^\infty H\left((\tfrac{d_0}{d})^\alpha\gamma, mU; y_n, r, \tilde{r}\right)\,\mathrm{d}y_n\right]\mathrm{d}r\,\mathrm{d}\tilde{r}. \tag{5.18}$$

Proof: For $d_i = d\,\forall i$, the parameters of the Nakagami-m RV $|\tilde{h}_n^{(s)}|$, given in (5.12) and (5.13), are $\Omega_s = 2\,\sigma^2\,d^{-\alpha}\,m\,U$ and $m_s = mU$. Plugging these parameters into (5.10) the proof is complete. ▮

Corolary 5.3 *An approximation for the SIR-based OP for an MRT-s-FAMA network under Nakagami-m fading channels for $d_i = d\,\forall i$, is given by*

$$P_{\text{out}} \approx \frac{1}{\Gamma(mK)\Gamma(mU)}\sum_{i=1}^{n_I}\sum_{j=1}^{n_J} w_i w_j \left[1-\sum_{l=1}^{n_L} w_l H\left((\tfrac{d_0}{d})^\alpha\gamma, mU; 2x_l, 2x_i, 2x_j\right)\right]^N. \tag{5.19}$$

Proof: Applying the generalized GLQ in (5.18) completes the proof. ▮

Theorem 5.2 *The SIR-based OP for an MRT-s-FAMA network under Nakagami-m fading channels for $d_i = d\,\forall i$ and mU being an integer, is given by*

$$P_{\text{out}} = \int_0^\infty \int_0^\infty \frac{r^{mK-1}\tilde{r}^{mU-1}e^{-\frac{r+\tilde{r}}{2}}}{2^{mK+mU}\Gamma(mK)\Gamma(mU)} \left[G\left(\left(\tfrac{d_0}{d}\right)^\alpha\gamma; mU,\, r,\, \tilde{r}\right)\right]^N dr\, d\tilde{r}, \tag{5.20}$$

where $G(\gamma, mU;\, r,\, \tilde{r})$ is given by

$$\begin{aligned}G(\gamma, mU; r, \tilde{r}) = {}& Q_{mU}\left(\sqrt{\frac{\delta\,\gamma\,\tilde{r}}{(1-\delta)(\gamma+1)}}, \sqrt{\frac{\delta\, r}{(1-\delta)(\gamma+1)}}\right) - \left(\frac{1}{\gamma+1}\right)^{mK+mU-1}\left(\frac{r}{\gamma\,\tilde{r}}\right)^{\frac{1-mK}{2}} \\ &\times \exp\left(-\frac{\delta\,(\gamma\,\tilde{r}+r)}{2(1-\delta)(\gamma+1)}\right)\sum_{k=0}^{mK+mU-2}\sum_{j=0}^{mK+mU-k-2}\frac{(mK+mU-(j+k)-1)_j}{j!} \\ &\times \left(\frac{r}{\tilde{r}}\right)^{\frac{j+k}{2}}(\gamma+1)^k\gamma^{\frac{j-k}{2}}\, I_{1-mK+j+k}\left(\frac{\delta\sqrt{\gamma\, r\,\tilde{r}}}{(1-\delta)(\gamma+1)}\right).\end{aligned} \tag{5.21}$$

Proof: For m_s an integer, the integral in the variable y_n in (5.10) is solved using [117, Corollary 3]. Following the steps presented in Chapter 3, using $m_s = mU$ and $\Omega_s = 2\,\sigma^2\,d^{-\alpha}\,m\,U$, since $d_i = d\,\forall i$, completes the proof. ▮

Corolary 5.4 *An approximation for the SIR-based OP for an MRT-s-FAMA network under Nakagami-m fading channels, for $d_i = d\,\forall i$ and mU being an integer, is given by*

$$P_{\text{out}} \approx \frac{1}{\Gamma(mK)\Gamma(mU)} \sum_{i=1}^{n_I} \sum_{j=1}^{n_J} w_i w_j \ \left[G\left(\left(\tfrac{d_0}{d}\right)^{\alpha} \gamma, mU;\, 2\,x_i,\, 2\,x_j \right) \right]^{N}. \tag{5.22}$$

Proof: Applying the generalized GLQ in (5.20) and (5.21), then (5.22) is obtained. ▮

Expressions for SIR-based OP for an MRT-FAMA network in s-FAMA mode under Rayleigh fading channels were provided in [88, Eqs. (27) and (28)]. However, those expressions are restricted to the case in which Ω[1] is an integer, which may not always be the case. Additionally, due to the notation used in [88], the effect of the large-scale fading parameters d_i, d_0, α, is not clear in those expressions. To force m_s to be an integer and to clearly reveal the effect of the large-scale fading parameters, in this work the restriction $d_i = d\ \forall i$ is used.

Careful consideration is required when selecting the distances between the BS and the UEs in the simulations. In particular, the condition $d_0 < d_i\ \forall i$ must be satisfied. If $d_0 > d_i$ for any user i, the fundamental assumption of the MRT-FAMA network model — namely, that each BS serves its closest user — would be violated.

The OP expressions obtained in this section generalize the results of s-FAMA in Chapter 3, extending the scenario to multiple transmitter antennas and varying large-scale fading. However, it should be noted that this chapter deals with an MRT-FAMA network, while the work in Chapter 3 is an FAMA network with only one macro-cell.

5.3 MRT FAST FAMA UNDER NAKAGAMI-m FADING CHANNELS

5.3.1 SIR Model

In the case of the MRT-f-FAMA network, the total interference signal is treated as a single RV and from (5.1) and (5.5), it is given by

$$\tilde{h}_n^I = \sum_{i=1}^{U} s_i \tilde{h}_n^{(i)} = \sum_{i=1}^{U} s_i d_i^{-\alpha/2} h_n^{(i)}. \tag{5.23}$$

[1]The parameter Ω used in [88], corresponds to m_s, with $m = 1$, in the notation of this thesis.

Unlike s-FAMA, here we need the sum of complex Nakagami-m RVs instead of the real ones. Considering the seminal work of Nakagami [46], the sum of the complex Nakagami-m interference RVs is approximated by another Nakagami-m RV, with parameters Ω_f and m_f given by [46, Eq. (96)]

$$\Omega_f = \sum_{i=1}^{U} \sigma_s^2 d_i^{-\alpha}(2m\sigma^2) = 2m\sigma^2\sigma_s^2 \sum_{i=1}^{U} d_i^{-\alpha} \tag{5.24}$$

and

$$m_f = \frac{m\left(\sum_{i=1}^{U} d_i^{-\alpha}\right)^2}{\sum_{i=1}^{U} d_i^{-2\,\alpha} + 2\,m\sum_{i\neq j}^{U} d_i^{-\alpha} d_j^{-\alpha}}. \tag{5.25}$$

If noise is ignored in (5.1), in an MRT-f-FAMA network, an UE selects the port where the SIR is maximized, such as

$$\mathrm{SIR} = \max_n \frac{\sigma_s^2|\tilde{h}_n|^2}{|\tilde{h}_n^I|^2}. \tag{5.26}$$

5.3.2 SIR-based Outage Probability - General Case

Theorem 5.3 *The SIR-based OP for an MRT-f-FAMA network under Nakagami-m fading channels is given by*

$$P_{\mathrm{out}} = \int_0^\infty \int_0^\infty \frac{r^{mK-1}\tilde{r}^{m_f-1}e^{-\frac{r+\tilde{r}}{2}}}{2^{mK+m_f}\Gamma(mK)\Gamma(m_f)} \prod_{n=1}^{N}\left[1-\frac{1}{2}\int_0^\infty H\left(\tfrac{d_0^\alpha\,\gamma/\sigma_s^2}{2\,\sigma^2(m_f/\Omega_f)}, m_f; y_n, r, \tilde{r}\right)\,\mathrm{d}y_n\right]\mathrm{d}r\,\mathrm{d}\tilde{r}. \tag{5.27}$$

Proof: Comparing the SIR for MRT-f-FAMA in (5.26) and the SIR for MRT-s-FAMA in (5.6), note that the expressions are almost the same, except for the symbol power σ_s^2 and the parameters of interfering Nakagami-m RV, Ω_f and m_f. Therefore, following the same steps presented in the Appendix E, completes the proof. ∎

Corolary 5.5 *An approximation for the SIR-based OP for an MRT-f-FAMA network under Nakagami-m fading channels is given by*

$$P_{\mathrm{out}} \approx \frac{1}{\Gamma(mK)\Gamma(m_f)} \sum_{i=1}^{n_I}\sum_{j=1}^{n_J} w_i w_j \left[1-\sum_{l=1}^{n_L} w_l H\left(\tfrac{d_0^\alpha\,\gamma}{2\,\sigma^2(m_f/\Omega_f)}, m_f; 2x_l, 2x_i, 2x_j\right)\right]^N. \tag{5.28}$$

Proof: Applying the generalized GLQ in (5.27), then (5.28) is obtained and completes the proof. ∎

5.3.3 SIR-based Outage Probability - Special Case

In this section, we consider the case where the distances d_i from interference BSs are the same.

Corolary 5.6 *The SIR-based OP for an MRT-f-FAMA network under Nakagami-m fading channels for $d_i = d\,\forall i$, is given by*

$$
\begin{aligned}
P_{\text{out}} = &\int_0^\infty \int_0^\infty \frac{r^{mK-1}\tilde{r}^{\,m_f-1} e^{-\frac{r+\tilde{r}}{2}}}{2^{mK+m_f}\Gamma(mK)\Gamma(m_f)} \prod_{n=1}^{N} \Bigg[1 - \frac{1}{2} \\
&\times \int_0^\infty H\left((mU-m+1)(\tfrac{d_0}{d})^\alpha \gamma, m_f; y_n, r, \tilde{r}\right) \,\mathrm{d}y_n \Bigg] \mathrm{d}r\, \mathrm{d}\tilde{r}.
\end{aligned}
\tag{5.29}
$$

Proof: For equal distances from interfering BSs, i.e. $d_i = d\,\forall i$, the parameters in (5.24) and (5.25) become $\Omega_f = 2\,\sigma^2\,\sigma_s^2\,d^{-\alpha}\,m\,U$ and $m_f = \frac{mU}{mU-m+1}$. Substituting these into (5.27) completes the proof. ▮

Corolary 5.7 *An approximation for the SIR-based OP for an MRT-f-FAMA network under Nakagami-m fading channels for $d_i = d\,\forall i$, is given by*

$$
P_{\text{out}} \approx \frac{1}{\Gamma(mK)\Gamma(m_f)} \sum_{i=1}^{n_I} \sum_{j=1}^{n_J} w_i w_j \left[1 - \sum_{l=1}^{n_L} w_l H\left((mU-m+1)(\tfrac{d_0}{d})^\alpha \gamma,\, m_f;\, 2x_l,\, 2x_i,\, 2x_j\right)\right]^N .
\tag{5.30}
$$

Proof: Applying the generalized GLQ in (5.29) completes the proof. ▮

We now restrict the analysis to the regime of a large number of BS, for which the results coincide with those obtained in the Rayleigh fading case, i.e., for $m = 1$.

Theorem 5.4 *The SIR-based OP for an MRT-f-FAMA network under Nakagami-m fading channels, for large U or $m = 1$, and $d_i = d, \forall i$, is given by*

$$
P_{\text{out}} = \int_0^\infty \int_0^\infty \frac{r^{mK-1}\tilde{r}^{\,m_f-1} e^{-\frac{r+\tilde{r}}{2}}}{2^{mK+m_f}\Gamma(mK)\Gamma(m_f)} \left[G\left((mU-m+1)(\tfrac{d_0}{d})^\alpha \gamma, 1; r, \tilde{r}\right)\right]^N \mathrm{d}r\, \mathrm{d}\tilde{r}.
\tag{5.31}
$$

Proof: For integer values of m_f, the integral with respect to the variable y_n in (5.29) is evaluated applying [117, Corollary 3] and following the procedure detailed in Chapter 3. For large U, $m_f = \frac{mU}{mU-m+1} \approx 1$, and for $m = 1$, $m_f = 1$. The replacement of these parameters within (5.29) completes the proof. ▮

Corolary 5.8 *An approximation for the SIR-based OP for an MRT-f-FAMA network under Nakagami-m fading channels, for large U or $m = 1$, and $d_i = d, \forall i$, is given by*

$$P_{\text{out}} \approx \frac{1}{\Gamma(mK)\Gamma(m_f)} \sum_{i=1}^{n_I} \sum_{j=1}^{n_J} w_i w_j \left[G\left((mU - m + 1) \left(\tfrac{d_0}{d}\right)^{\alpha} \gamma, 1;\, 2\,x_i,\, 2\,x_j \right) \right]^N . \tag{5.32}$$

Proof: Applying the generalized GLQ in expression (5.31) completes the proof. ∎

The OP expressions for f-FAMA, obtained in this section, generalize the results of Chapter 4 and [37], extending the scenario to multiple transmitter antennas and varying large-scale fading. However, it should be noted that this work deals with an MRT-FAMA network, while the mentioned works are FAMA networks with only one macro-cell.

5.4 SUPPLEMENTARY INSIGHTS

5.4.1 Numerical Computation

For the numerical computation of OP for a FAMA system, the term containing the modified Bessel function of the first kind $\mathrm{I}_\nu(z)$ must be integrated from 0 to ∞, but when $z \to \infty$, results in $\mathrm{I}_\nu(z) \to \infty$, which can result in a numerical integration error. Some papers, such as [38] and [88], suggest a technique to deal with it. These articles suggest to write $\mathrm{I}_\nu(z) = \frac{1}{\pi}\int_0^\pi \cos(\nu\,\theta)\exp(z\cos\theta)\,\mathrm{d}\theta$ and insert it into the OP expression. However, it requires one more integral to be calculated, which increases the computation time and also has to deal with the oscillation of the cosine function.

Alternatively, a different approach can take advantage of special properties, such as the scaling property, of well known software packages. The codes[2] used in this thesis were implemented in MATLAB®, in which the function $\mathrm{I}_\nu(z)$ can be scaled, that is, multiplied by e^{-z}. Thus, for example, to code (5.10), $\mathrm{I}_\nu(z)$ is replaced by $e^z\, \mathrm{I}_\nu^{\text{scaled}}(z)$ and e^z is grouped with the other exponential term $e^{-(y_n + \frac{\delta}{1-\delta}\tilde{r})/2}$.

Consequently, all OP expressions can be evaluated numerically by applying the minor modifications outlined above to avoid numerical integration errors.

[2]The codes are available at https://github.com/deMouraPaulo/FAMA

5.4.2 Monte Carlo Simulation

The simulation curves presented in Section 5.5 are calculated by generating appropriate Gaussian RVs, depending on SIR expression, as described above.

Simulation for s-FAMA. This case deals with the sum of squared Nakagami-m RVs, which are modeled as the sum of Gaussian RVs as in (5.3). Therefore SIR in (5.6) is simulated by generating samples of Gaussian RVs and adding them appropriately.

Simulation for f-FAMA, with $m_f \approx 1$. This is the case where $m = 1$ or U is large, for $d_i = d, \forall i$. For this case, the interfering RV $|\tilde{h}_n^I = \sum_{i=1}^U s_i \tilde{h}_n^{(i)}|$ is Rayleigh distributed, and the simulation is easily performed by rewriting (5.26) as a sum of squared Gaussian RVs.

Simulation for f-FAMA, with $m_f \not\approx 1$. For this case, the interfering RV $|\tilde{h}_n^I = \sum_{i=1}^U s_i \tilde{h}_n^{(i)}|$ cannot be written as a sum of squared Gaussian RVs. Thus, the complex Nakagami-m RVs $s_i\,\tilde{h}_n^{(i)}$ of each interference signal must be added. For this simulation, we apply the method described in [123] to generate the correlated Nakagami-m fading samples, which are added within the complex domain.

5.4.3 Spatial Block-Correlation Model

The spatial block-correlation model for Nakagami-m fading channels studied in Chapter 4 offers more accurate results, compared to the constant correlation model, especially if the number of ports N in FAS is large. This model can be used for MRT-s-FAMA or MRT-f-FAMA, through the subsequent procedure.

First, consider that N ports of an FA will be divided into blocks B, each block b of size L_b, such as $N = \sum_{b=1}^B L_b$. Consider that the ports in a block are highly correlated, with a correlation coefficient in the range $\delta \in (0.95, 0.99)$. Then, use Algorithm 1 of [45] to obtain B and L_b. The OP derived in this chapter is considered the OP per block $P_{\text{out};b}$. Finally, calculate OP as $P_{\text{out}} = \prod_{b=1}^B P_{\text{out};b}(\gamma)$ as in (4.7).

5.4.4 Multiplexing Gain

Beyond OP, another important indicator is the multiplexing gain, which measures the capacity scaling of the network and is defined as [38, Eq. (29)]

$$\mathcal{G}_m = (U+1)(1-P_{\text{out}}), \tag{5.33}$$

where $U+1$ is the number of BSs in the network and we consider that each BS serves one user. Therefore the number of BSs and UEs are the same. This will be useful in numerical analysis.

5.4.5 SNR-based Outage Probability - MRT-FAS

In a noise-limited scenario, as in a non-dense frequency reuse system, the user of an MRT network is served by the closest BS but does not suffer interference from the remaining BSs, which can be called MRT-FAS network. For this scenario, SNR is given by

$$\text{SNR} = \max_n \frac{\sigma_s^2 |\tilde{h}_n|^2}{\sigma_\eta^2}. \tag{5.34}$$

Theorem 5.5 *The SNR-based OP for MRT-FAS is given by*

$$P_{\text{out}} = \int_0^\infty \frac{r^{mK-1} e^{-\frac{r}{2}}}{2^{mK}\Gamma(mK)} \left[1 - Q_{mK}\left(\sqrt{\frac{\delta\, r}{1-\delta}}, \sqrt{\frac{2\, mK\, \gamma}{\Upsilon\,(1-\delta)}}\right)\right]^N dr. \tag{5.35}$$

where γ is the received SNR threshold and Υ is the average received SNR, given by

$$\Upsilon = \frac{\sigma_s^2 \mathbb{E}[|\tilde{h}_n|^2]}{\sigma_\eta^2} = \frac{2\, m\, K\, \sigma^2\, \sigma_s^2\, d_0^{-\alpha}}{\sigma_\eta^2}. \tag{5.36}$$

Proof: The OP is calculated as

$$\begin{aligned} P_{\text{out}} &= \text{Prob}\left(\frac{\sigma_s^2|\tilde{h}_1|^2}{\sigma_\eta^2} < \gamma, \ldots, \frac{\sigma_s^2|\tilde{h}_N|^2}{\sigma_\eta^2} < \gamma\right) \\ &= F_{|\tilde{h}_1|,\ldots,|\tilde{h}_N|}\left(\sqrt{\sigma_\eta^2\,\gamma/\sigma_s^2}, \ldots, \sqrt{\sigma_\eta^2\,\gamma/\sigma_s^2}\right). \end{aligned} \tag{5.37}$$

Using the joint CDF of $|\tilde{h}_1|, \ldots, |\tilde{h}_N|$, given in (E.1) of Appendix E, completes the proof. ∎

The OP expressions for an MRT-FAS network, obtained in this section, generalize the results of FAS in [36], extending the scenario to multiple transmitter antennas for Nakagami-m fading channels fading and large-scale fading. However, it should be noted that this section deals with an MRT-FAS network, while the work [36] are the case of a single-user FAS served by one BS.

5.4.6 Single Antenna Case

All OP expressions derived in this work require that FAS have the number of ports $N \geq 2$. In the case of replacing FAS with a single antenna, OP is easily obtained. For UEs with a single antenna and BS performing MRT, the OP is calculated, similarly to Appendix E, but considering only one port, as

$$\begin{aligned} P_{\text{out}} &= \text{Prob}\left(\frac{|\tilde{h}_1|^2}{|\tilde{h}_1^{(s)}|^2} < \gamma\right) \\ &= \text{Prob}\left(|\tilde{h}_1| < \sqrt{\gamma\,|\tilde{h}_1^{(s)}|}\right) \\ &= \int_0^\infty F_{|\tilde{h}_1|}\left(\sqrt{\gamma\, t_1^2}\right) p_{|\tilde{h}_1^{(s)}|}(t_1)\,\mathrm{d}t_1. \end{aligned} \tag{5.38}$$

As there is only one port, the correlation parameter between ports does not make sense. In that case, substituting $\delta = 1$ in (5.4), results in a single Nakagami-m RV $|\tilde{h}_1|$ for the desired user with parameters mK and $2\sigma^2 d^{-\alpha} mK$, and a single Nakagami-m RV $|\tilde{h}_1^{(s)}|$ for the total interference with parameters m_s and Ω_s. Substituting PDF and CDF of RVs $|\tilde{h}_1^{(s)}|$ and $|\tilde{h}_1|$ in (5.38), after some mathematical manipulation, results in

$$P_{\text{out}} = \int_0^\infty \frac{r^{m_s-1}e^{-r}}{\Gamma(m_s)\Gamma(mK)}\,\Gamma\left(mK, \frac{\gamma\, r}{2\,\sigma^2\, d_0^{-\alpha}\,(m_s/\Omega_s)}\right)\mathrm{d}r, \tag{5.39}$$

where $\Gamma(\cdot\,,\cdot)$ is the lower incomplete Gamma function. For $d = d_i \forall i$, it reduces to

$$P_{\text{out}} = \int_0^\infty \frac{r^{mU-1}e^{-r}}{\Gamma(mU)\Gamma(mK)}\,\Gamma\left(mK,\ \left(\tfrac{d_0}{d}\right)^\alpha \gamma\, r\right)\mathrm{d}r. \tag{5.40}$$

For the case of f-FAMA, following similar steps results in

$$P_{\text{out}} = \int_0^\infty \frac{r^{m_f-1}e^{-r}}{\Gamma(m_f)\Gamma(mK)}\,\Gamma\left(mK, \frac{\gamma\, r}{2\,\sigma_s^2\,\sigma^2\, d_0^{-\alpha}(m_f/\Omega_f)}\right)\mathrm{d}r. \tag{5.41}$$

For $d = d_i \forall i$, it reduces to

$$P_{\text{out}} = \int_0^\infty \frac{e^{-r}}{\Gamma(mK)}\,\Gamma\left(mK,\ \left(\tfrac{d_0}{d}\right)^\alpha (m\,U - m + 1)\,\gamma\, r\right)\mathrm{d}r. \tag{5.42}$$

It should be noted that, if there is only one antenna, the concepts of s-FAMA and f-FAMA do not apply, and the OP for both cases should be similar, as will be demonstrated in the numerical results. Nevertheless, the OP expressions for a single-antenna are used for comparative analysis.

5.5 NUMERICAL RESULTS

Figure 5.2 presents the OP as a function of the number of ports N for s-FAMA, f-FAMA, and for the case where the UE is equipped with a single FPA, instead of an FAS antenna, for comparative analysis. The curves were plotted using the integral expressions (5.20) and (5.29) for s-FAMA and f-FAMA, respectively, and for the curves for FPA the expression (5.40) was used. The remaining parameters of the system are: $W = 5$, $\gamma = 0$ dB, $U = 3$ interference BS, $m = 2$, $d = 100$, $d_0 = 100$ and $\alpha = 3$. For the system to achieve an OP of 4×10^{-8}, BSs with 20 antennas are required if a single FPA is used in the receiver. But if the receiver is equipped with an FA, only four antennas are required in the BS, for an FAS receiver with about 14 ports. This alleviates the burden of BS, as fewer antennas are required using FAS to achieve the same OP. Additionally, it should be noted that with a larger number of antennas in BS, the performance of s-FAMA reaches f-FAMA, which is unusual behavior. The superior performance of s-FAMA is particularly advantageous, as it represents a more practically feasible deployment compared to f-FAMA, as discussed in Chapter 2. This unusual superior performance of s-FAMA depends on other system parameters and is detailed in the next analysis.

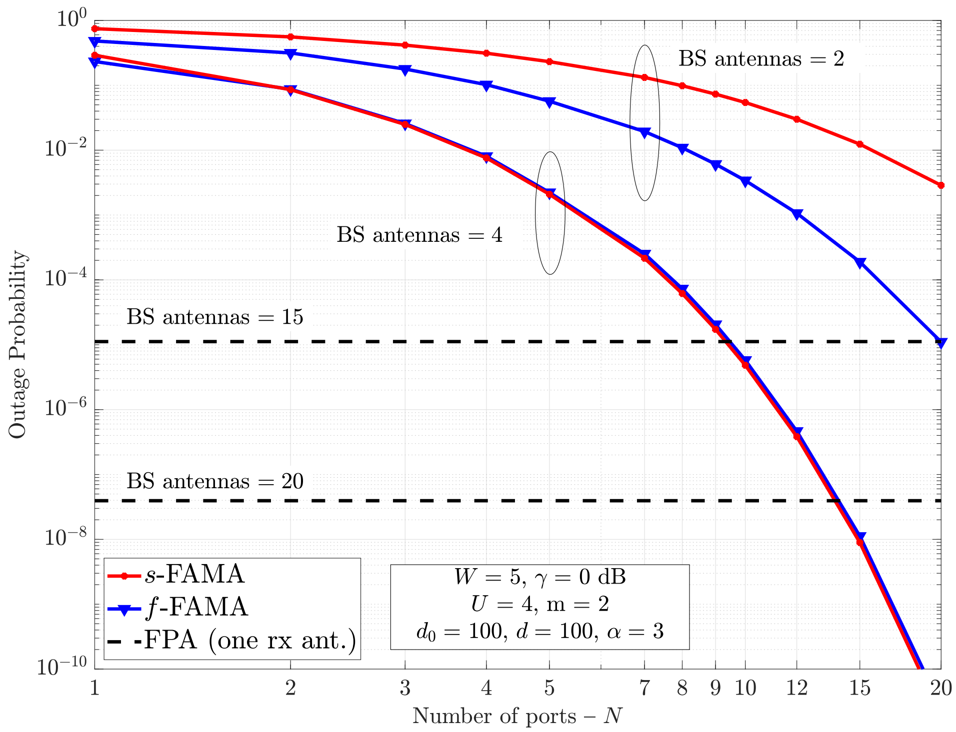

Figure 5.2. SIR-based OP curves as a function of the number of port N for s-FAMA, f-FAMA and 1 FPA. The remaining parameters of the system are: $W = 5$, $\gamma = 0$ dB, $U = 4$, $m = 2$, $d = 100$, $d_0 = 100$ and $\alpha = 3$.

Figure 5.3 presents SIR-based OP curves as a function of the SIR threshold, for s-FAMA and f-FAMA, with different numbers of antennas at the BSs $K = \{2,8\}$, and $N = 10$, $W = 1$, $U = 4, m = 2$, $d_0 = 200$, $d = 500$, $\alpha = 3$. For s-FAMA the curves were plotted for the SIR-based OP integral in (5.20), the SIR-based OP GLQ approximation in (5.22) and the Monte Carlo simulation based on SIR in (5.6). For f-FAMA the curves were plotted for the SIR-based OP integral in (5.29), the SIR-based OP GLQ approximation in (5.30) and the Monte Carlo simulation based on the SIR in (5.26). All curves exhibit strong overlap, validating our analysis. Performance improves as the number of antennas in BSs increases for s-FAMA and f-FAMA. For a low SIR threshold s-FAMA outperforms f-FAMA, which is unusual behavior, but this behavior reverses as the SIR threshold increases. When the number of antennas in BSs increases, the value of γ where the curves cross also increases.

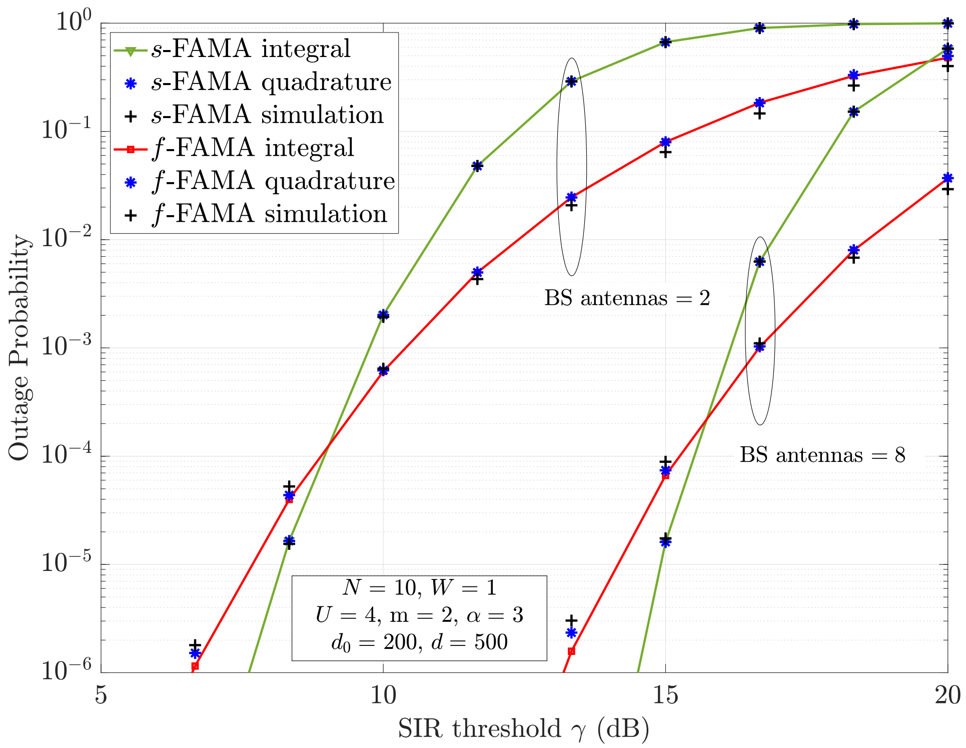

Figure 5.3. SIR-based OP curves as a function of the SIR threshold, for s-FAMA and f-FAMA, with different number of antennas at the BSs $K = \{2,8\}$. The remaining parameters are: $N = 10$, $W = 1$, $U = 4$, $m = 2$, $d_0 = 200$, $d = 500$ and $\alpha = 3$.

Now, we examine the behavior of the system, considering $\sigma = \sigma_s = 1$. The desired signal power $|\tilde{h}_n|^2$ is Chi-square distributed, with the mean and variance calculated as $\mathbb{E}[|\tilde{h}_n|^2] = 2mKd^{-\alpha}$ and $\mathbb{V}[|\tilde{h}_n|^2] = 4mKd^{-2\alpha}$ [116, (2.3-25)]. Therefore, the mean and variance of the desired signal power increase linearly with the number of BS antennas K. With a higher mean of the desired signal, FAS is more likely to find a port with SIR higher than a given threshold; in other words, increasing K, reduces the OP.

Now, we compare slow and fast FAMA using the mean and variance of Nakagami-m RVs, given in [116, (2.3-71)]. With the parameters m_s and Ω_s of s-FAMA, given (5.13) and (5.12), and the parameters of m_f and Ω_f of f-FAMA, given in (5.25) and (5.24), the following analysis is performed. The mean and variance ratios of the interference signals for fast and slow FAMA are calculated, respectively, as $\mathbb{E}[|\tilde{h}_n^I|]/\mathbb{E}[|\tilde{h}_n^{(s)}|] = 0.91318$ and $\mathbb{V}[|\tilde{h}_n^I|]/\mathbb{V}[|\tilde{h}_n^{(s)}|] = 6.236$. As interference of f-FAMA has a lower mean than s-FAMA, one could infer that its performance is always better. This is true for a high SIR threshold. However, since the interference variance for f-FAMA is greater than s-FAMA, for a low SIR threshold, the variance of f-FAMA degrades its performance. This explains the crossing of the curves of s-FAMA and f-FAMA.

Figure 5.4 presents SIR-based OP and multiplexing gain curves as a function of the number of interference BSs U, for s-FAMA and f-FAMA, with the system parameters: $N = 100$, $K = 2$, $m = 2$, $\gamma = 3\,\text{dB}$, $W = 1$, $d_0 = 40$, $d = 100$ and $\alpha = 3$. As the number of ports N is high, for better precision, the curves were plotted using the spatial block-correlation model, with parameters $\rho_{\text{th}} = N/100$ and $\delta = 0.97$, and the OPs per block given by (5.22) and (5.32). For a low number of interferences BSs, s-FAMA surpasses f-FAMA performance in terms of OP, but with similar multiplexing gain. However, for a high number of interferences BSs, f-FAMA performs better in terms of OP and multiplexing gain. Additionally, the multiplexing gain curve of s-FAMA has an inflection point. Therefore, f-FAMA always performs better for a large number of uses, which is an expected behavior.

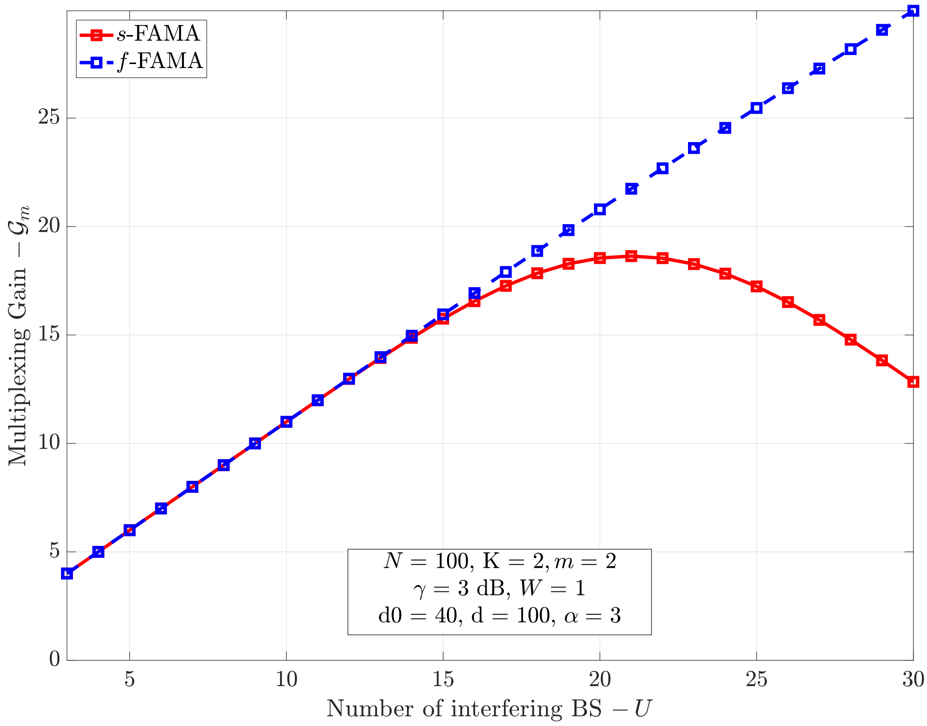

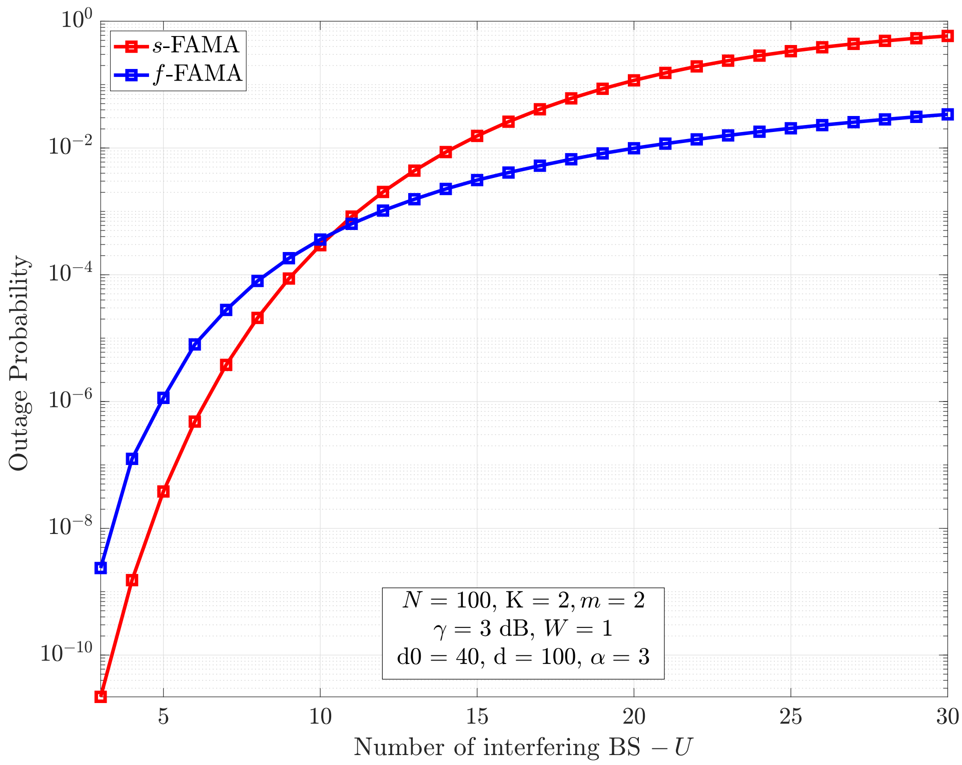

Figure 5.4. SIR-based OP and multiplexing gain curves as a function of the number of interfering BS – U, for s-FAMA and f-FAMA, with the system parameters: $N = 100$, $K = 2$, $m = 2$, $\gamma = 3$ dB, $W = 1$ $d_0 = 40$, $d = 100$, and $\alpha = 3$.

5.6 CONCLUSION

This chapter studied MRT-FAMA networks under Nakagami-m fading channels in fast and slow FAMA configurations. Analytical OP expressions were obtained for both setups. The numerical and simulation results confirmed the accuracy of the proposed analytical framework. This work extends the MRT-FAMA analysis to more general fading and presents OP expressions, from the more complex and precise to the simplest, to provide useful information about the behavior of the system. The use of FAS in UE can reduce the complexity of the network in terms of the number of BS antennas. The work also showed that, depending on the network parameters, s-FAMA can outperform f-FAMA, what is an unusual behavior in the literature.

CHAPTER 6

CONCLUSIONS AND FUTURE WORKS

6.1 SUGGESTIONS FOR FUTURE WORKS

Research in the field of FAS and FAMA is growing rapidly, with many publications, as exposed in Chapter 2, in just a few years. However, there is much to be done to turn FAS and FAMA into a feasible technology in the future 6G networks.

In terms of channel studies for FAMA, theoretical models can be improved to more sophisticated ones, concerning, for example, the α-μ distribution. Practical models using empirical data could also help to understand the behavior of FAS and FAMA systems.

Optimization of FAMA with aspects such as power control, port selection, spectral efficiency, and user scheduling, just to mention a few, is a great challenge. With so many variables, the optimization becomes a complex problem and algorithms should be proposed to deal with real-time conditions.

Furthermore, it would be of significant interest to conduct a comparative analysis of FAMA against alternative techniques, such as massive MIMO, with particular emphasis on performance under imperfect CSI conditions. In addition, an in-depth investigation of cell-free FAMA architectures involving a large number of BSs jointly serving a single FAS user represents a promising direction for future research.

As FAS is in an early stage of research, the hardware is not mature enough for large scale testing. Some prototypes exist, but they are restricted to some research centers and are not suitable for practical applications. In addition, some hardware design should be considered. The switching time is a major issue, mutual coupling should also be examined, and investigation on suitable fluids is of great importance.

Integration with emerging technologies and standards is of key importance. Simulations and modeling FAMA in actual (and future) standards of 3GPP and ITU can boost the adoption by industry as it can be viewed as more feasible solution and can gain greater attention. A step further is to integrate these studies with emerging technologies such as RIS or ISAC, as FAMA can take a *ride* in the on going development. The synergy of these technologies with FAMA can help improve existing networks.

The new paradigm of antenna design introduced by FAS can be explored in many creative ways. One possible example is to improve physical layer security. As the position of an antenna port can be chosen to optimize the strength of the desired signal, it can also be chosen to be null for potential eavesdroppers. Future works can use that and other strategies to improve security.

Studies should also advance the EE for FAS in scenarios where dynamic reconfiguration of FAS may lead to increased power demands, as current studies are based on more restricted scenarios.

To conclude, as the foundation idea of FAS is a conductive fluid, studies on fluid materials should advance to understand the fluid properties that better trade-off conductivity, non-toxicity, stability, and melting point.

6.2 CONCLUSIONS

This thesis examined FAMA under Nakagami-m fading channels for two network configurations: the first consists of a single BS and a set of UEs equipped with FAS, the second scenario investigates an MRT-FAMA architecture in which multiple BSs, each equipped with an antenna array, employ MRT precoding to serve a single UE equipped with FAS.

In Chapter 3, for a network with a single BS and a set of UEs equipped with FAS, new OP expressions for s-FAMA systems under Nakagami-m fading channels were derived using the constant correlation model, including an upper bound for SIR-based OP and bounds for the multiplexing gain. Closed-form and approximate SINR-based OP expressions were obtained. In general, s-FAMA systems under harsher conditions (lower fading severity m) have been shown to achieve better OP performance and higher multiplexing gain.

In Chapter 4, for the same network as in Chapter 3, but using the more accurate spatial block-correlation model, OP expressions and bounds for s-FAMAand f-FAMA, under

Nakagami-m fading channels, were derived and applied to the study of O-FAMA. Multiplexing gain expressions were also obtained. In particular, the results demonstrated better correspondence to realistic models such as Jakes' as the number of ports N increases, while maintaining the analytical tractability of the constant correlation model. The analytical framework was validated by Monte Carlo simulations.

Chapter 5 investigated MRT-FAMA networks under Nakagami-m fading channels for both s-FAMA and f-FAMA configurations. This architecture comprises multiple BSs, each equipped with an antenna array and employing MRT precoding, to serve a single UE equipped with FAS. Closed-form and approximate expressions for the OP were derived for each configuration. The numerical and simulation results validated the proposed analytical framework. Employing FAS at the UE side can lower the network complexity by reducing the required number of BS antennas. Furthermore, the study demonstrated that, depending on the network parameters, s-FAMA can outperform f-FAMA, which is an uncommon outcome in the existing literature.

Some limitations of the present study are as follows: it assumes perfect knowledge of the CSI at the UE; it relies on fast port switching, which is particularly challenging to realize for f-FAMA and thus poses nontrivial implementation issues; and, in the case of MRT-FAMA, it presupposes the availability of accurate CSI at the BS in order to perform MRT precoding.

Considering the prominence of FAMA technology and the importance of its study in environments aligned with empirical data, such as Nakagami-m fading channels, this thesis contributed to fill this gap.

In summary, this thesis provided an original analytical framework for the evaluation of FAMA under Nakagami-m fading and tractable correlation models, contributing to the development of FAS/FAMA as a candidate technology for 6G.

APPENDIX A

UPPER BOUNDS FOR OP UNDER SLOW FAMA NETWORKS: CONSTANT CORRELATION MODEL

The expression (3.25) can be rewritten as

$$P_{\text{out}} = \int_{\tilde{r}=0}^{\infty}\int_{r=0}^{\infty} \frac{r^{m-1}\tilde{r}^{\tilde{U}-1}}{2^{m+\tilde{U}}\Gamma(m)\Gamma(\tilde{U})} e^{-\frac{r+\tilde{r}}{2}} \Bigg[1 - \underbrace{\left(1 - \mathrm{Q}_{\tilde{U}}(\cdot, \cdot + \cdots)\right)}_{Z}\Bigg]^{N} \mathrm{d}r\, \mathrm{d}\tilde{r} \tag{A.1}$$

$$\approx \int_{\tilde{r}=0}^{\infty}\int_{r=0}^{\infty} \frac{r^{m-1}\tilde{r}^{\tilde{U}-1}}{2^{m+\tilde{U}}\Gamma(m)\Gamma(\tilde{U})} e^{-\frac{r+\tilde{r}}{2}} \Bigg[1 - N\underbrace{\left(1 - \mathrm{Q}_{\tilde{U}}(\cdot, \cdot + \cdots)\right)}_{Z}\Bigg] \mathrm{d}r\, \mathrm{d}\tilde{r}, \tag{A.2}$$

which can be approximated by (A.2) since Z is typically small and N is large.

Using the lower bound [38, Eq. (72)]

$$\mathrm{I}_{\nu}(z) > \frac{1}{\Gamma(\nu+1)}\left(\frac{z}{2}\right)^{\nu} \tag{A.3}$$

and the approximation $\gamma + 1 \approx \gamma$ in (A.2), the relationships

$$\begin{aligned}
&\left(\frac{1}{\gamma+1}\right)^{m+\tilde{U}-1}\left(\frac{r}{\gamma\,\tilde{r}}\right)^{\frac{1-m}{2}} e^{-\frac{\delta}{2(1-\delta)}\frac{\gamma\,\tilde{r}+r}{\gamma+1}} \\
&\quad\times \sum_{k,j} \frac{(m+\tilde{U}-k-j-1)_j}{j!}\left(\frac{r}{\tilde{r}}\right)^{\frac{j+k}{2}} \frac{(\gamma+1)^k}{\gamma^{\frac{k-j}{2}}}\mathrm{I}_{\substack{1-m\\+j+k}}\left(\frac{\delta\sqrt{\gamma\, r\,\tilde{r}}}{(1-\delta)(\gamma+1)}\right) && \text{(A.4)}\\
&> \left(\frac{r}{\gamma\,\tilde{r}}\right)^{\frac{1-m}{2}} e^{-\frac{\delta}{2(1-\delta)}\frac{\gamma\,\tilde{r}+r}{\gamma+1}} \\
&\quad\times \sum_{k,j} \frac{(m+\tilde{U}-k-j-1)_j}{j!}\left(\frac{r}{\tilde{r}}\right)^{\frac{j+k}{2}} \frac{\gamma^{-m-\tilde{U}+1+\frac{k+j}{2}}}{\Gamma(2-m+k+j)}\left[\frac{\delta\sqrt{\gamma\, r\,\tilde{r}}}{2(1-\delta)(\gamma+1)}\right]^{\substack{1-m\\+j+k}} && \text{(A.5)}\\
&= e^{-\left(\frac{\delta}{2(1-\delta)}\frac{\gamma}{\gamma+1}\right)\tilde{r}} \sum_{k,j} \frac{(m+\tilde{U}-k-j-1)_j}{j!(1-m+k+j)!}\frac{1}{\gamma^{\tilde{U}+\frac{m-1}{2}-\frac{k+j}{2}}} \\
&\quad\times \left[\frac{\delta\sqrt{\gamma}}{2(1-\delta)(\gamma+1)}\right]^{1-m+j+k} e^{-\left(\frac{\delta}{2(1-\delta)}\frac{1}{\gamma+1}\right)r}\, r^{(1-m+j+k)} && \text{(A.6)}
\end{aligned}$$

can be obtained after simplifications, in which $\sum_{k,j}$ represents $\sum_{k=0}^{m+\tilde{U}-2}\sum_{j=0}^{m+\tilde{U}-k-2}$.

Using (A.2) and (A.6), results in

$$P_{\text{out}} < (1-N)A + N\,B - N\,C, \tag{A.7}$$

in which A, B and C are given, respectively, by

$$A = \int_0^\infty \int_0^\infty \frac{r^{m-1}\tilde{r}^{\tilde{U}-1}}{2^{m+\tilde{U}}\Gamma(m)\Gamma(\tilde{U})} e^{-\frac{\tilde{r}+r}{2}}\,\mathrm{d}r\,\mathrm{d}\tilde{r}, \tag{A.8}$$

$$B = \int_0^\infty \int_0^\infty \frac{r^{m-1}\tilde{r}^{\tilde{U}-1}}{2^{m+\tilde{U}}\Gamma(m)\Gamma(\tilde{U})} e^{-\frac{\tilde{r}+r}{2}} \mathrm{Q}_{\tilde{U}}\left(\sqrt{\frac{\delta\,\gamma\,\tilde{r}}{(1-\delta)(\gamma+1)}}, \sqrt{\frac{\delta\,r}{(1-\delta)(\gamma+1)}}\right)\mathrm{d}r\,\mathrm{d}\tilde{r}, \tag{A.9}$$

and

$$\begin{aligned} C = &\int_0^\infty \int_0^\infty \frac{r^{m-1}\tilde{r}^{\tilde{U}-1}}{2^{m+\tilde{U}}\Gamma(m)\Gamma(\tilde{U})} e^{-\frac{\tilde{r}+r}{2}} e^{-\left(\frac{\delta}{2(1-\delta)}\frac{\gamma}{\gamma+1}\right)\tilde{r}} \\ &\times \sum_{k,j}\left(\frac{(m+\tilde{U}-k-j-1)_j}{j!(1-m+k+j)!}\left[\frac{\delta\sqrt{\gamma}}{2(1-\delta)(\gamma+1)}\right]^{\substack{1-m\\+j+k}} \frac{e^{-\left(\frac{\delta}{2(1-\delta)}\frac{1}{\gamma+1}\right)r}\,r^{1-m+k+j}}{\gamma^{\tilde{U}+\frac{m-1}{2}-\frac{k+j}{2}}}\right)\mathrm{d}r\,\mathrm{d}\tilde{r}. \end{aligned} \tag{A.10}$$

To evaluate A, [38, Eq.(66)] is used, which results in $A = 1$. To evaluate B, [124, Eq. (B-54)] is used, substituting $c = 0$ and $p^2/2 = s$, and proceeding with the change of variable $t = x^2$, which results in

$$\int_0^\infty e^{-s\,t}\,\mathrm{Q}_M(b,a\sqrt{t})\,\mathrm{d}t = \frac{1}{s}\left(1-\left(\frac{a^2}{a^2+2\,s}\right)^M e^{-\frac{b^2 s}{a^2+2\,s}}\right). \tag{A.11}$$

The integral in (A.11) can be identified as the Laplace transform of $Q_M(b,a\sqrt{t})$, i.e., $\mathcal{L}\{Q_M(b,a\sqrt{t})\}$. Therefore, B can be initially evaluated using

$$\int_0^\infty e^{-s\,r}\,r^{m-1}\,\mathrm{Q}_{\tilde{U}}(b,a\sqrt{r})\,\mathrm{d}r = \mathcal{L}\{r^{m-1}\mathrm{Q}_{\tilde{U}}(b,a\sqrt{r})\}, \tag{A.12}$$

with $b = \sqrt{\frac{\delta\,\gamma\,\tilde{r}}{(1-\delta)(\gamma+1)}}$ and $a = \sqrt{\frac{\delta}{(1-\delta)(\gamma+1)}}$. Note that b is a function of $\tilde{r}$.

The task now is to calculate (A.12) with $s = 1/2$. Using the Laplace Transform derivative property, $\mathcal{L}\{rf(r)\} = -\partial F(s)/\partial s$, $m-1$ times, results in $\mathcal{L}\{r^{m-1}f(r)\} = (-1)^{m-1}\frac{\partial^{m-1}}{\partial s}F(s)$, and (A.12) can be written with the help of (A.11) as

$$\mathcal{I}(\tilde{r}) = \int_0^\infty r^{m-1}\,e^{-\frac{r}{2}}\,\mathrm{Q}_{\tilde{U}}(b,a\sqrt{r})\,\mathrm{d}r = (-1)^{m-1}\frac{\partial^{m-1}}{\partial s}\left(\frac{1}{s}-\frac{1}{s}\left(\frac{a^2}{a^2+2\,s}\right)^{\tilde{U}} e^{-\frac{b^2 s}{a^2+2\,s}}\right). \tag{A.13}$$

Now, B is rewritten as

$$
\begin{aligned}
B &\overset{(a)}{=} \int_0^\infty \frac{\tilde{r}^{\tilde{U}-1}\, e^{-\frac{\tilde{r}}{2}}}{2^{\tilde{U}}\,\Gamma(\tilde{U})} \frac{\mathcal{I}(\tilde{r})}{2^m\,\Gamma(m)}\, \mathrm{d}\tilde{r} \\
&\overset{(b)}{=} \int_0^\infty \frac{\tilde{r}^{\tilde{U}-1}\, e^{-\frac{\tilde{r}}{2}}}{2^{\tilde{U}}\,\Gamma(\tilde{U})} \left(1 - \frac{(-1)^{m-1}}{2^m\,\Gamma(m)} \frac{\partial^{m-1}}{\partial s}\left(\frac{1}{s}\left(\frac{a^2}{a^2+2\,s}\right)^{\tilde{U}} e^{-\frac{b^2 s}{a^2+2\,s}}\right)\right) \mathrm{d}\tilde{r} \\
&\overset{(c)}{=} 1 - \frac{(-1)^{m-1}}{2^m\,\Gamma(m)} \frac{\partial^{m-1}}{\partial s} \int_0^\infty \frac{\tilde{r}^{\tilde{U}-1}\, e^{-\frac{\tilde{r}}{2}}}{2^{\tilde{U}}\,\Gamma(\tilde{U})} \left(\frac{1}{s}\left(\frac{\frac{\delta}{(1-\delta)(\gamma+1)}}{\frac{\delta}{(1-\delta)(\gamma+1)}+2\,s}\right)^{\tilde{U}} e^{-\left(\frac{\frac{\delta\,\gamma}{(1-\delta)(\gamma+1)}\,s}{\frac{\delta}{(1-\delta)(\gamma+1)}+2\,s}\right)\tilde{r}}\right) \mathrm{d}\tilde{r} \\
&\overset{(d)}{=} 1 - \frac{(-1)^{m-1}\,\delta^{\tilde{U}}}{2^m\,\Gamma(m)\,2^{\tilde{U}}} \frac{\partial^{m-1}}{\partial s}\left(\frac{(\delta/2 + s(\gamma+1-\delta))^{-\tilde{U}}}{s}\right) \\
&\overset{(e)}{=} 1 - \frac{(-1)^{m-1}\,\delta^{\tilde{U}}}{2^m\,\Gamma(m)\,2^{\tilde{U}}} \\
&\quad \times \sum_{i=0}^{m-1} (-1)^{m-1} \frac{(m-1)!}{(m-1-i)!} \frac{(\tilde{U})_{m-1-i}\,(2^{-1}\,\delta + s(\gamma+1-\delta))^{-\tilde{U}-m+1+i}\,(\gamma+1-\delta)^{m-1-i}}{s^{i+1}} \\
&\overset{(f)}{\approx} 1 - \left(\frac{\delta}{\gamma+1}\right)^{\tilde{U}} \sum_{i=0}^{m-1} \frac{(\tilde{U})_{m-1-i}}{(m-1-i)!},
\end{aligned}
\tag{A.14}
$$

in which (a) uses $\mathcal{I}(\tilde{r})$; (b) substitutes (A.13) and uses the fact that the first term of $\mathcal{I}(\tilde{r})$ is $(-1)^{2(m-1)}2^m\Gamma(m)$ for $s = 1/2$; (c) applies [38, Eq. (66)] to solve the first integral, whose result is one; the order of integration and derivative are changed and in sequence replacing a and b in the second term; and (d) is found applying [38, Eq. (66)] and some simplifications.

To evaluate the derivative in (d), the recurrence formula

$$
\frac{\partial^{m-1}}{\partial s}\frac{F(s)}{s} = \sum_{i=0}^{m-1} \frac{(m-1)!}{(m-1-i)!} \frac{(-1)^i}{s^{i+1}} \frac{\partial^{m-1-i}}{\partial s} F(s), \tag{A.15}
$$

is used, and for $F(s) = (2^{-1}\,\delta + s(\gamma+1-\delta))^{-\tilde{U}}$ it follows that

$$
\frac{\partial^n}{\partial s} F(s) = (-1)^n (\tilde{U})_n (2^{-1}\,\delta + s(\gamma+1-\delta))^{-\tilde{U}-n} (\gamma+1-\delta)^n. \tag{A.16}
$$

Using $n = m-1-i$ in (A.16), replacing the mentioned expression in (A.15) and substituting the resulting expression in step (d) of (A.14), then step (e) is obtained. The final result for B is obtained in step (f) of (A.14) by making $s = 1/2$, $\gamma + 1 \approx \gamma$, $\gamma + 1 - \delta \approx \gamma$ in terms within the summation, and after some simplifications.

A simplified form of C is evaluated as

$$
\begin{aligned}
C &\overset{(a)}{=} \sum_{k=0}^{m+\tilde{U}-2} \sum_{j=0}^{m+\tilde{U}-k-2} \frac{(\tilde{U}+m-k-j-1)_j}{j!(1-m+k+j)!} \frac{1}{\gamma^{\tilde{U}+\frac{m-1}{2}-\frac{k+j}{2}}} \left[\frac{\delta\sqrt{\gamma}}{2(1-\delta)(\gamma+1)}\right]^{\substack{1-m\\+j+k}} \\
&\quad \times \int_0^\infty \frac{\tilde{r}^{\tilde{U}-1}}{2^{\tilde{U}}\Gamma(\tilde{U})} e^{-\frac{1}{2}\left(1+\frac{\delta}{(1-\delta)}\frac{\gamma}{(\gamma+1)}\right)\tilde{r}} \mathrm{d}\tilde{r} \times \int_0^\infty \frac{r^{k+j}}{2^m\Gamma(m)} e^{-\frac{1}{2}\left(1+\frac{\delta}{(1-\delta)}\frac{1}{(\gamma+1)}\right)r} \mathrm{d}r \\
&\overset{(b)}{=} \frac{1}{\Gamma(m)} \sum_{k=0}^{\substack{m+\tilde{U}\\-2}} \sum_{j=0}^{\substack{m+\tilde{U}\\-k-2}} \frac{(\tilde{U}+m-k-j-1)_j}{j!(1-m+k+j)!} \frac{(k+j)!}{\gamma^{\tilde{U}+m-(k+j)}} \frac{\delta^{1-m+k+j}}{[(1+(1-\delta)\gamma)]^{k+j+1}} \frac{[(1-\delta)(\gamma+1)]^{\tilde{U}+m}}{(\gamma+1-\delta)^{\tilde{U}}} \\
&\overset{(c)}{=} \frac{1}{\Gamma(m)} \left(\frac{1-\delta}{\gamma}\right)^{\tilde{U}} \sum_{k=0}^{\substack{m+\tilde{U}\\-2}} \sum_{j=0}^{\substack{m+\tilde{U}\\-k-2}} \frac{(\tilde{U}+m-k-j-1)_j}{j!} \frac{(k+j)!}{(1-m+k+j)!} \left(\frac{\delta}{1-\delta}\right)^{1-m+k+j} \\
&\overset{(d)}{\approx} \left(\frac{1-\delta}{\gamma}\right)^{\tilde{U}} \Gamma(m) \sum_{k=0}^{m-1} \frac{(\tilde{U})_{m-1-k}}{(m-1-k)!},
\end{aligned} \tag{A.17}
$$

where: (a) follows from the fact that the double integral is expressed as the product of two integrals over r and $\tilde{r}$; (b) uses [38, Eq. (66)] to solve the integrals with som simplifications; (c) considers that: $1+(1-\delta))\gamma \approx (1-\delta))\gamma$, $\gamma+1 \approx \gamma$ and $\gamma+1-\delta \approx \gamma$; and (d) simplifies the summation and ignores the higher order terms.

Finally, the upper bound (A.7) is rewritten as

$$
P_{\text{out}} < \left[1 - \left(\frac{\delta}{\gamma+1}\right)^{\tilde{U}} \sum_{i=0}^{m-1} \frac{(\tilde{U})_{m-1-i}}{(m-1-i)!} - N\left(\frac{1-\delta}{\gamma}\right)^{\tilde{U}} \sum_{i=0}^{m-1} \frac{(\tilde{U})_{m-1-i}}{(m-1-i)!}\right]. \tag{A.18}
$$

To avoid negative values for very large N, due to the use of the approximation $(1-Z)^N \approx 1 - N\,Z$, the operation $(\cdot)^+$ is adopted, resulting in (3.26). For small δ and $\gamma \approx \gamma+1$, it follows that $\delta^{\tilde{U}} \ll (1-\delta)^{\tilde{U}}$ and thus (3.27) is obtained since the term $(\delta/(\gamma+1))^{\tilde{U}}$ is removed.

Finally, if $W \geq 1$, then according to [41, Eq. 7], $\delta = 1/(\pi W)$ is substituted in (3.27), and (3.28) is obtained. This completes the proof.

APPENDIX B

AN APPROXIMATION FOR OP UNDER SLOW FAMA NETWORKS: CONSTANT CORRELATION MODEL

To obtain an approximation for the OP in (3.33), the change of variables $r_1 = \tilde{r}/2$ and $r_2 = r/2$ is used. The resulting integral is divided into three integrals, namely $\mathcal{I}_1$, $\mathcal{I}_2$ and $\mathcal{I}_3$, such as

$$\mathcal{I}_1(r_2,r_1) = \int_{y_k=0}^{\infty} \mathrm{Q}_m\left(\sqrt{\frac{2\,\delta\,r_2}{1-\delta}}, \sqrt{\gamma\,y_k + \frac{2\,m\,\gamma}{\Upsilon(1-\delta)}}\right) \times \left(\frac{y_k}{\frac{2\,\delta}{1-\delta}r_1}\right)^{\frac{\tilde{U}-1}{2}} e^{-\frac{y_k+\frac{2\,\delta}{1-\delta}r_1}{2}} \mathrm{I}_{\tilde{U}-1}\left(\sqrt{\frac{2\,\delta}{1-\delta}}\sqrt{r_1 y_k}\right) \mathrm{d}y_k, \tag{B.1}$$

$$\mathcal{I}_2(r_2) = \int_{r_1=0}^{\infty} e^{-r_1}\, r_1^{\tilde{U}-1}\left[1 - \frac{\mathcal{I}_1(r_2,r_1)}{2}\right]^N \mathrm{d}r_1 \tag{B.2}$$

and

$$\mathcal{I}_3 = \int_{r_2=0}^{\infty} e^{-r_2}\, r_2^{m-1}\, \mathcal{I}_2(r_2)\ \mathrm{d}r_2. \tag{B.3}$$

Using (B.3), the OP is given by

$$P_{\text{out}} = \frac{\mathcal{I}_3}{\Gamma(m)\,\Gamma(\tilde{U})}. \tag{B.4}$$

To evaluate $\mathcal{I}_2$ and $\mathcal{I}_3$ the Gauss-Laguerre quadrature method [125, Eq. (25.4.45)] is employed to approximate an integral by a sum, which is given by

$$\int_0^{\infty} e^{-x} f(x)\mathrm{d}x \approx \sum_{i=1}^{n} w_i\, f(x_i), \tag{B.5}$$

where x_i is the i-th root of Laguerre polynomial $L_n(x)$ in which $i \in \{1,\ldots,n\}$, with n denoting the number of Laguerre polynomial roots and the weight $w_i = \frac{x_i}{(n+1)^2[L_{n+1}(x_i)]^2}$.

For the evaluation of $\mathcal{I}_1(r_2,r_1)$, an alternative expression for (B.5) is used, given by

$$\int_0^{\infty} f(x)\mathrm{d}x \approx \sum_{i=1}^{n} w_i\, e^{x_i} f(x_i), \tag{B.6}$$

Finally, (3.35) is obtained after some simplifications.

APPENDIX C

OP FOR A FAMA NETWORK: SPATIAL BLOCK-CORRELATION MODEL

To deduce the OP per block for FAMA under the Nakagami-m channels, using spatial block-correlation, some statistics for $\mathbb{X}_n$ in (4.5) and $\mathbb{Y}_n$ in (4.6) need to be found, similarly to Section 3.4.1.

To obtain the multivariate PDF of $\mathbb{X}_n$ (4.5), it is first conditioned to the RV

$$r_b = \sum_{l=1}^{m} (\mathrm{x}_{b(n)l}^{(u,u)})^2 + (\mathrm{y}_{b(n)l}^{(u,u)})^2. \tag{C.1}$$

Therefore, $\mathbb{X}_n|r_b$ can be identified as a noncentral Chi-squared distribution with $2m$ DoFs, and from [116, Eq. (2.3-29)] its PDF is given by

$$p_{\mathbb{X}_n|r_b}(x_n) = \frac{1}{2}\left(\frac{x_n}{\frac{\delta}{1-\delta}r_b}\right)^{\frac{m-1}{2}} e^{-\frac{x_n+\frac{\delta}{1-\delta}r_b}{2}} \mathrm{I}_{m-1}\left(\sqrt{\frac{\delta}{1-\delta}}\sqrt{r_b x_n}\right). \tag{C.2}$$

As RVs $\{\mathbb{X}_n\}$ are all linked by $\{r_b\}$ they are conditionally independent and the multivariate PDF is the product of individual PDFs

$$p_{\mathbb{X}_1,\ldots,\mathbb{X}_N|r_b}(x_1,\ldots,x_N) = \prod_{b=1}^{B}\prod_{n\in\mathcal{N}_b}\frac{1}{2}\left(\frac{x_n}{\frac{\delta}{1-\delta}r_b}\right)^{\frac{m-1}{2}} e^{-\frac{x_n+\frac{\delta}{1-\delta}r_b}{2}} \mathrm{I}_{m-1}\left(\sqrt{\frac{\delta}{1-\delta}}\sqrt{r_b x_n}\right), \tag{C.3}$$

where $\mathcal{N}_b$ is the set of n indices corresponding to block b, and the size $\mathcal{N}_b$ is L_b.

Note that r_b, for $b = \{1,\ldots,B\}$, is a central Chi-squared distribution with $2m$ DoFs with PDF given by [116, Eq. (2.3-29)]

$$p_{r_b}(r_b) = \frac{r_b^{m-1}e^{-\frac{r_b}{2}}}{2^m\Gamma(m)}, \tag{C.4}$$

and, due to the independence of the RVs $r_1,\ldots,r_B$, then

$$p_{r_1,\ldots,r_B}(r_1,\ldots,r_B) = \prod_{b=1}^{B} p_{r_b}(r_b) = \prod_{b=1}^{B}\frac{r_b^{m-1}e^{-\frac{r_b}{2}}}{2^m\Gamma(m)}. \tag{C.5}$$

The joint unconditional PDF of $\mathbb{X}_1,\ldots,\mathbb{X}_N$ can be derived by

$$p_{\mathbb{X}_1,\ldots,\mathbb{X}_N}(x_1,\ldots,x_N) = \int_0^\infty \cdots \int_0^\infty p_{\mathbb{X}_1,\ldots,\mathbb{X}_N|r_1,\ldots,r_B}(x_1,\ldots,x_N)\, p_{r_1,\ldots,r_B}(r_1,\ldots,r_B)\mathrm{d}r_1,\ldots,r_B$$
$$= \int_0^\infty \cdots \int_0^\infty \prod_{b=1}^{B}\prod_{n\in\mathcal{N}_b} \frac{1}{2}\left(\frac{x_n}{\frac{\delta}{1-\delta}r_b}\right)^{\frac{m-1}{2}} e^{-\frac{x_n+\frac{\delta}{1-\delta}r_b}{2}} \mathrm{I}_{m-1}\left(\sqrt{\frac{\delta r_b x_n}{1-\delta}}\right) \times \prod_{b=1}^{B} \frac{r_b^{m-1}e^{-\frac{r_b}{2}}}{2^m\Gamma(m)}\,\mathrm{d}r_1,\ldots,\mathrm{d}r_B$$
$$= \int_0^\infty \cdots \int_0^\infty \prod_{b=1}^{B}\prod_{n\in\mathcal{N}_b} \frac{r_b^{m-1}e^{-\frac{r_b}{2}}}{2^m\Gamma(m)} \frac{1}{2}\left(\frac{x_n}{\frac{\delta}{1-\delta}r_b}\right)^{\frac{m-1}{2}} e^{-\frac{x_n+\frac{\delta}{1-\delta}r_b}{2}} \mathrm{I}_{m-1}\left(\sqrt{\frac{\delta r_b x_n}{1-\delta}}\right) \mathrm{d}r_1,\ldots,\mathrm{d}r_B. \quad \text{(C.6)}$$

By using (C.6), the multivariate CDF can be calculated as

$$F_{X_1,\ldots,X_N}(t_1,\ldots,t_N) \overset{(a)}{=} \int_0^{t_1}\cdots\int_0^{t_N} p_{\mathbb{X}_1,\ldots,\mathbb{X}_N}(x_1,\ldots,x_N)\mathrm{d}x_1,\ldots,\mathrm{d}x_N$$
$$\overset{(b)}{=} \int_0^{t_1}\cdots\int_0^{t_N}\int_{r_1=0}^\infty\cdots\int_{r_B=0}^\infty \prod_{b=1}^{B}\prod_{n\in\mathcal{N}_b} \frac{r_b^{m-1}e^{-\frac{r_b}{2}}}{2^m\Gamma(m)}$$
$$\times \frac{1}{2}\left(\frac{x_n}{\frac{\delta}{1-\delta}r_b}\right)^{\frac{m-1}{2}} e^{-\frac{x_n+\frac{\delta}{1-\delta}r_b}{2}} \mathrm{I}_{m-1}\left(\sqrt{\frac{\delta r_b x_n}{1-\delta}}\right) \mathrm{d}r_1,\ldots,\mathrm{d}r_B\,\mathrm{d}x_1,\ldots,\mathrm{d}x_N$$
$$\overset{(c)}{=} \prod_{b=1}^{B}\int_0^\infty \frac{r_b^{m-1}e^{-\frac{r_b}{2}}}{2^m\Gamma(m)} \prod_{n\in\mathcal{N}_b}\int_0^{t_n} \frac{1}{2}\left(\frac{x_n}{\frac{\delta}{1-\delta}r_b}\right)^{\frac{m-1}{2}} e^{-\frac{x_n+\frac{\delta}{1-\delta}r_b}{2}} \mathrm{I}_{m-1}\left(\sqrt{\frac{\delta r_b x_n}{1-\delta}}\right) \mathrm{d}x_n\,\mathrm{d}r_b$$
$$\overset{(d)}{=} \prod_{b=1}^{B}\int_0^\infty \frac{r_b^{m-1}e^{-\frac{r_b}{2}}}{2^m\Gamma(m)} \prod_{n\in\mathcal{N}_b}\left[1-\mathrm{Q}_m\left(\sqrt{\frac{\delta\, r_b}{1-\delta}},\sqrt{t_n}\right)\right]\mathrm{d}r_b, \quad \text{(C.7)}$$

where (a) uses the definition of a multivariate CDF; (b) follows from (C.6); (c) changes the order of integration and writes the multifold integrals as a product of single integrals in the variables x_n and r_b; and in (d) it is recognized that the integration over x_n is the CDF of a non-central Chi-squared distribution with $2m$ DoFs [116, Eq. (2.3-35)].

In turn, the multivariate PDF of Y_k in (4.6) can be obtained by conditioning $\mathbb{Y}_n$ to the RV

$$\tilde{r}_b = \sum_{\substack{\tilde{u}=1\\ \tilde{u}\neq u}}^{U}\sum_{l=1}^{m_{\tilde{u}}}(\mathrm{x}_{b(n)l}^{(\tilde{u},u)})^2 + (\mathrm{y}_{b(n)l}^{(\tilde{u},u)})^2. \quad \text{(C.8)}$$

Thus, $Y_n|\tilde{r}_b$ is a noncentral Chi-squared distribution with $2\,\tilde{U}$ DoFs, and from [116, Eq. (2.3-29)] its PDF is given by

$$p_{\mathbb{Y}_n|\tilde{r}_b}(y_n) = \frac{1}{2}\left(\frac{y_n}{\frac{\delta}{1-\delta}\tilde{r}_b}\right)^{\frac{\tilde{U}-1}{2}} e^{-\frac{y_n+\frac{\delta}{1-\delta}\tilde{r}_b}{2}} \times \mathrm{I}_{\tilde{U}-1}\left(\sqrt{\frac{\delta}{1-\delta}}\sqrt{\tilde{r}_b y_n}\right). \quad \text{(C.9)}$$

As all $Y_n|\tilde{r}_0$ are independent for any n, the conditional multivariate PDF is the product of individual PDFs. Similarly to X_n, and knowing that $\tilde{r}_b$ in a central Chi-square RV with $2\,\tilde{U}$

DoFs, it follows that the multivariate PDF of Y_n is given by

$$p_{\mathbb{Y}_1,\ldots,\mathbb{Y}_N}(y_1,\ldots,y_N) = \prod_{b=1}^{B}\int_0^\infty \frac{\tilde{r_b}^{\tilde{U}-1}e^{-\frac{\tilde{r_b}}{2}}}{2^{\tilde{U}}\Gamma(\tilde{U})} \times \prod_{n\in\mathcal{N}_b}\frac{1}{2}\left(\frac{y_n}{\frac{\delta}{1-\delta}\tilde{r_b}}\right)^{\frac{\tilde{U}-1}{2}} e^{-\frac{y_n+\frac{\delta}{1-\delta}\tilde{r_b}}{2}}\mathrm{I}_{\tilde{U}-1}\left(\sqrt{\frac{\delta\,\tilde{r_b}\,y_n}{1-\delta}}\right)\mathrm{d}\tilde{r_b}, \tag{C.10}$$

where the multivariate integral is expressed as a product of B single integrals.

The OP is calculated as

$$\begin{aligned}
P_{\text{out}} &\overset{(a)}{=} P\left(\frac{\mathbb{X}_1}{\mathbb{Y}_1}<\gamma,\ldots,\frac{\mathbb{X}_N}{\mathbb{Y}_N}<\gamma\right) = P\left(\mathbb{X}_1<\gamma\mathbb{Y}_1,\ldots,\mathbb{X}_N<\gamma\mathbb{Y}_N\right)\\
&\overset{(b)}{=} \int_0^\infty\cdots\int_0^\infty F_{\mathbb{X}_1,\ldots,\mathbb{X}_N|\mathbb{Y}_1,\ldots,\mathbb{Y}_N}(\gamma y_1,\ldots,\gamma y_N)\; p_{\mathbb{Y}_1,\ldots,\mathbb{Y}_N}(y_1,\ldots,y_N)\mathrm{d}y_1,\ldots\mathrm{d}y_N\\
&\overset{(c)}{=} \underbrace{\int_0^\infty\cdots\int_0^\infty}_{y_1,\ldots,y_N}\int_{r_b=0}^\infty\prod_{b=1}^{B}\frac{r_b^{m-1}e^{-\frac{r_b}{2}}}{2^m\Gamma(m)}\prod_{n\in\mathcal{N}_b}\left[1-\mathrm{Q}_m\left(\sqrt{\frac{\delta\,r_b}{1-\delta}},\sqrt{\gamma\,y_n}\right)\right]\mathrm{d}r_b\\
&\quad\times\prod_{b=1}^{B}\int_{\tilde{r_b}=0}^\infty\frac{\tilde{r_b}^{\tilde{U}-1}e^{-\frac{\tilde{r_b}}{2}}}{2^{\tilde{U}}\Gamma(\tilde{U})}\prod_{n\in\mathcal{N}_b}\frac{1}{2}\left(\frac{y_n}{\frac{\delta}{1-\delta}\tilde{r_b}}\right)^{\frac{\tilde{U}-1}{2}} e^{-\frac{y_n+\frac{\delta}{1-\delta}\tilde{r_b}}{2}}\mathrm{I}_{\tilde{U}-1}\left(\sqrt{\frac{\delta\,\tilde{r_b}\,y_n}{1-\delta}}\right)\mathrm{d}\tilde{r_b}\;\mathrm{d}y_1,\ldots\mathrm{d}y_N\\
&\overset{(d)}{=} \prod_{b=1}^{B}\int_0^\infty\int_0^\infty\frac{r_b^{m-1}e^{-\frac{r_b}{2}}}{2^m\Gamma(m)}\frac{\tilde{r_b}^{\tilde{U}-1}e^{-\frac{\tilde{r_b}}{2}}}{2^{\tilde{U}}\Gamma(\tilde{U})}\prod_{n\in\mathcal{N}_b}\Bigg[1-\int_{y_n=0}^\infty\mathrm{Q}_m\left(\sqrt{\frac{\delta\,r_b}{1-\delta}},\sqrt{\gamma\,y_n}\right)\\
&\quad\times\frac{1}{2}\left(\frac{y_n}{\frac{\delta}{1-\delta}\tilde{r_b}}\right)^{\frac{\tilde{U}-1}{2}} e^{-\frac{y_n+\frac{\delta}{1-\delta}\,\mathrm{d}r_b\,\tilde{r_b}}{2}}\mathrm{I}_{\tilde{U}-1}\left(\sqrt{\frac{\delta\,\tilde{r_b}\,y_n}{1-\delta}}\right)\mathrm{d}y_n\Bigg]\mathrm{d}r_b\;\mathrm{d}\tilde{r_b}\\
&\overset{(e)}{=} \prod_{b=1}^{B}P_{\text{out};b}(\gamma),
\end{aligned} \tag{C.11}$$

where: (a) follows from (4.4); (b) calculates the unconditional CDF by averaging the conditional CDF over the PDF of $\mathbb{Y}_n$; (c) follows from (C.7) and (C.10); (d) changes the order of integration, writes the multifold integrals as a product of single integrals on the variables y_n, r_b and $\tilde{r}_b$, and recognizes that the first integral over y_n is unit, as it is the total probability of a noncentral Chi-squared distribution; (e) rewrites the previous expression as the OP per block.

Therefore, the expression (4.7) is obtained and the proof is complete.

APPENDIX D

UPPER BOUND FOR OP UNDER SLOW FAMA NETWORKS: SPATIAL BLOCK-CORRELATION MODEL

From the approximation for the OP shown in (4.14) and using [120, Eqs. (3.351-1)], it follows that

$$\int_0^{f(\widetilde{r}_b)} r^{m-1} e^{-\frac{r_b}{2}} \mathrm{d}r_b = 2^m \Gamma(m) \left(1 - e^{-\frac{f(\widetilde{r}_b)}{2}} \sum_{i=1}^{m-1} \frac{[f(\widetilde{r}_b)]^i}{i!\, 2^i}\right). \tag{D.1}$$

Plugging (D.1) into (4.14) results in

$$\begin{aligned} P_{\text{out}} &\approx \prod_{b=1}^{B} \int_0^{\infty} \frac{\widetilde{r}_b^{\widetilde{U}-1} e^{-\widetilde{r}_b/2}}{2^{m+\widetilde{U}} \Gamma(m) \Gamma(\widetilde{U})} \, 2^m \Gamma(m) \left(1 - e^{-\frac{f(\widetilde{r}_b)}{2}} \sum_{i=1}^{m-1} \frac{[f(\widetilde{r}_b)]^i}{i!\, 2^i}\right) \mathrm{d}\widetilde{r}_b \\ &\approx \prod_{b=1}^{B} \left(1 - \frac{1}{2^{\widetilde{U}}\, \Gamma(\widetilde{U})} \int_0^{\infty} \widetilde{r}_b^{\widetilde{U}-1} \, e^{-\frac{\widetilde{r}_b + f(\widetilde{r}_b)}{2}} \sum_{i=1}^{m-1} \frac{[f(\widetilde{r}_b)]^i}{i!\, 2^i} \, \mathrm{d}\widetilde{r}_b\right), \end{aligned} \tag{D.2}$$

where the first integral of the first line is unit, since it is the total probability of a central Chi-squared distribution. Setting the threshold as $f(\widetilde{r}_b) = \gamma\, \widetilde{r}_b$, an upper bound is obtained. Inverting the sum and integral in (D.2) gives

$$P_{\text{out}} < \prod_{b=1}^{B} \left(1 - \frac{1}{2^{\widetilde{U}}\, \Gamma(\widetilde{U})} \sum_{i=1}^{m-1} \frac{\gamma^i}{i!\, 2^i} \int_0^{\infty} \widetilde{r}_b^{\widetilde{U}-1+i} \, e^{-\frac{1+\gamma}{2} \widetilde{r}_b} \, \mathrm{d}\widetilde{r}_b\right). \tag{D.3}$$

Using [120, Eq. (3.351-3)], the integral is solved as

$$\int_0^{\infty} \widetilde{r}_b^{\widetilde{U}-1+i} \, e^{-\frac{1+\gamma}{2} \widetilde{r}_b} \, \mathrm{d}\widetilde{r}_b = \Gamma(\widetilde{U}+i) \left(\frac{2}{\gamma+1}\right)^{\widetilde{U}+i}. \tag{D.4}$$

From the properties of the Pochhammer symbol and the Gamma function, it follows that

$$(\widetilde{U})_i = \frac{(\widetilde{U}+i-1)!}{(\widetilde{U}-1)!} = \frac{\Gamma(\widetilde{U}+i)}{\Gamma(\widetilde{U})}. \tag{D.5}$$

Inserting (D.4) and (D.5) into (D.3), the expression (4.15) is obtained, and the proof is complete.

APPENDIX E

OP FOR MRT-FAMA NETWORKS

To obtain the OP for an MRT-s-FAMA network, some statistics of $|\tilde{h}_n|$, given in (5.7), and $|\tilde{h}_n^{(s)}|$, given in (5.9), must be found. The RV X_n, shown in (5.8), is Chi-square distributed, with $2mK$ DoFs, and the joint CDF of $X_1, \ldots, X_N$ is given by 3.15. Proceeding with the change of RV $|\tilde{h}_n|^2 = d_0^{-\alpha}\sigma^2(1-\delta)X_n$, we have the CDF $F_{|\tilde{h}_n|}(\tau_n) = F_{X_n}(\tau_n^2/d_0^{-\alpha}\sigma^2(1-\delta))$, therefore the joint CDF of $|\tilde{h}_1|, \ldots, |\tilde{h}_N|$ is

$$F_{|\tilde{h}_1|,\ldots,|\tilde{h}_N|}(\tau_1, \ldots, \tau_N) = \int_0^\infty \frac{r^{mK-1}e^{-\frac{r}{2}}}{2^{mK}\Gamma(mK)} \prod_{n=1}^{N} \left[1 - \mathrm{Q}_{mK}\left(\sqrt{\frac{\delta\, r}{1-\delta}}, \sqrt{\frac{\tau_n^2}{d_0^{-\alpha}\sigma^2(1-\delta)}}\right)\right] \mathrm{d}r. \tag{E.1}$$

The OP for MRT-s-FAMA, denoted by P_{out}, for a given SIR threshold γ, is calculated in (E.2), where: (a) follows from (5.6); (b) calculates the unconditional CDF of $|\tilde{h}_1|, \ldots, |\tilde{h}_N|$ by averaging the conditional CDF over the PDF of $|\tilde{h}_1^{(s)}|, \ldots, |\tilde{h}_N^{(s)}|$; (c) uses the fact that $|\tilde{h}_1|, \ldots, |\tilde{h}_N|$ and $|\tilde{h}_1^{(s)}|, \ldots, |\tilde{h}_N^{(s)}|$ are independent and substitute (E.1) and [88, Eq. (26)]; (d) changes the order of integration of variables $t_1, \ldots, t_N$, r_0 and r a and writes the multivariate integral as a product of N single integrals in the variable t_n; (e) comes from the fact that the first integral is one, as it is the total probability of conditional Nakagami-m RVs t_n and r_0; (f) applies the change of variables $y_n = \frac{2}{1-\delta}\frac{m_s}{\Omega_s}t_n^2$ and $\tilde{r} = 2\frac{m_s}{\Omega_s}r_0^2$ to the inner and outer integrals. Rewriting (f) in the form of (5.10) completes the proof.

$$
\begin{aligned}
P_{\text{out}} &\overset{(a)}{=} \text{Prob}(\text{SIR} < \gamma) = \text{Prob}\left(\frac{|\tilde{h}_1|^2}{|\tilde{h}_1^{(s)}|^2} < \gamma, \ldots, \frac{|\tilde{h}_N|^2}{|\tilde{h}_N^{(s)}|^2} < \gamma\right) \\
&= \text{Prob}\left(|\tilde{h}_1| < \sqrt{\gamma}\, |\tilde{h}_1^{(s)}|, \ldots, |\tilde{h}_N| < \gamma\, |\tilde{h}_N^{(s)}|\right) \\
&\overset{(b)}{=} \int_0^\infty \cdots \int_0^\infty F_{|\tilde{h}_1|,\ldots,|\tilde{h}_N| \,\mid\, |\tilde{h}_1^{(s)}|,\ldots,|\tilde{h}_N^{(s)}|}(\sqrt{\gamma}\, t_1, \ldots, \sqrt{\gamma}\, t_N)\, p_{|\tilde{h}_1^{(s)}|,\ldots,|\tilde{h}_N^{(s)}|}(t_1, \ldots, t_N)\, \mathrm{d}t_1, \ldots, \mathrm{d}t_N \\
&\overset{(c)}{=} \underbrace{\int_0^\infty \cdots \int_0^\infty}_{t_1 \cdots t_N} \int_{r=0}^\infty \frac{r^{mK-1}}{2^{mK}\Gamma(mK)} e^{-\frac{r}{2}} \prod_{n=1}^N \left[1 - \mathrm{Q}_{mK}\left(\sqrt{\frac{\delta\, r}{1-\delta}}, \sqrt{\frac{\gamma\, t_n^2}{d_0^{-\alpha}\sigma^2(1-\delta)}}\right)\right] \mathrm{d}r \\
&\quad \times \int_0^\infty \frac{2{m_s}^{m_s-1} r_0^{2m_s-1} e^{-\frac{m_s}{\Omega_s} r_0^2}}{\Gamma(m_s)\Omega_s^{m_s}} \prod_{n=1}^N \frac{2\, m_s\, r_0^{1-m_s}\, t_n^{m_s}}{\Omega_s(1-\delta)\delta^{(m_s-1)/2}}\, e^{-\frac{\delta\, m_s\, r_0^2 + m_s\, t_n^2}{(1-\delta)\Omega_s}} \\
&\quad \times \mathrm{I}_{m_s-1}\left(\frac{2\, m_s \sqrt{\delta}\, t_n\, r_0}{(1-\delta)\Omega_s}\right) \mathrm{d}r_0\, \mathrm{d}t_1, \ldots, \mathrm{d}t_N \\
&\overset{(d)}{=} \int_0^\infty \int_0^\infty \frac{r^{mK-1} e^{-\frac{r}{2}}}{2^{mK}\Gamma(mK)} \frac{2{m_s}^{m_s-1} r_0^{2m_s-1} e^{-\frac{m_s}{\Omega_s} r_0^2}}{\Gamma(m_s)\Omega_s^{m_s}} \\
&\quad \times \prod_{n=1}^N \int_{t_n=0}^\infty \left[1 - \mathrm{Q}_{mK}\left(\sqrt{\frac{\delta\, r}{1-\delta}}, \sqrt{\frac{\gamma\, t_n^2}{d_0^{-\alpha}\sigma^2(1-\delta)}}\right)\right] \\
&\quad \times \frac{2\, m_s\, r_0^{1-m_s}\, t_n^{m_s}}{\Omega_s(1-\delta)\delta^{(m_s-1)/2}} e^{-\frac{\delta\, m_s\, r_0^2 + m_s\, t_n^2}{(1-\delta)\Omega_s}} \mathrm{I}_{m_s-1}\left(\frac{2\, m_s \sqrt{\delta}\, t_n\, r_0}{(1-\delta)\Omega_s}\right) \mathrm{d}t_n\, \mathrm{d}r\, \mathrm{d}r_0 \\
&\overset{(e)}{=} \int_0^\infty \int_0^\infty \frac{2{m_s}^{m_s-1} r^{mK-1} r_0^{2m_s-1} e^{-\frac{r}{2} - \frac{m_s}{\Omega_s} r_0^2}}{2^{mK}\Gamma(mK)\Gamma(m_s)\Omega_s^{m_s}} \\
&\quad \times \prod_{n=1}^N \left[1 - \int_{t_n=0}^\infty \mathrm{Q}_{mK}\left(\sqrt{\frac{\delta\, r}{1-\delta}}, \sqrt{\frac{\gamma\, t_n^2}{d_0^{-\alpha}\sigma^2(1-\delta)}}\right)\right. \\
&\quad \times \left.\frac{2\, m_s\, r_0^{1-m_s}\, t_n^{m_s}}{\Omega_s(1-\delta)\delta^{(m_s-1)/2}} e^{-\frac{\delta\, m_s\, r_0^2 + m_s\, t_n^2}{(1-\delta)\Omega_s}} \mathrm{I}_{m_s-1}\left(\frac{2\, m_s \sqrt{\delta}\, t_n\, r_0}{(1-\delta)\Omega_s}\right) \mathrm{d}t_n\right] \mathrm{d}r\, \mathrm{d}r_0 \\
&\overset{(f)}{=} \int_0^\infty \int_0^\infty \frac{r^{mK-1} \tilde{r}^{m_s-1} e^{-\frac{r+\tilde{r}}{2}}}{2^{mK+m_s}\Gamma(mK)\Gamma(m_s)} \\
&\quad \times \prod_{n=1}^N \left[1 - \frac{1}{2}\int_0^\infty \mathrm{Q}_{mK}\left(\sqrt{\frac{\delta\, r}{1-\delta}}, \sqrt{\frac{d_0^\alpha\, \gamma\, y_n}{2\,\sigma^2(m_s/\Omega_s)}}\right)\right. \\
&\quad \times \left.\left(\frac{y_n}{\frac{\delta}{(1-\delta)}\tilde{r}}\right)^{\frac{m_s-1}{2}} e^{-\frac{y_n + \frac{\delta}{1-\delta}\tilde{r}}{2}}\, \mathrm{I}_{m_s-1}\left(\sqrt{\frac{\delta\, y_n\, \tilde{r}}{1-\delta}}\right) \mathrm{d}y_n\right] \mathrm{d}r\, \mathrm{d}\tilde{r}.
\end{aligned} \tag{E.2}
$$

REFERENCES

[1] F. Tariq, M. R. A. Khandaker, K.-K. Wong, M. A. Imran, M. Bennis, and M. Debbah, "A speculative study on 6G," *IEEE Wireless Commun.*, vol. 27, no. 4, pp. 118–125, Aug. 2020. Cited in page 1.

[2] *Framework and overall objectives of the future development of IMT for 2030 and beyond*, Rec. ITU-R M.2160-0, ITU, Geneva, Switzerland, Nov. 2023. Cited in page 1.

[3] L. Roberts, "The evolution of packet switching," *Proceedings of the IEEE*, vol. 66, no. 11, pp. 1307–1313, 1978. Cited in page 1.

[4] A. J. Paulraj and T. Kailath, "Increasing Capacity in Wireless Broadcast Systems Using Distributed Transmission/directional Reception (DTDR)," U.S. Patent 5 345 599A, Sep. 6, 1994. Cited in page 1.

[5] S. Alamouti, "A simple transmit diversity technique for wireless communications," *IEEE J. Sel. Areas Commun.*, vol. 16, no. 8, pp. 1451–1458, 1998. Cited in page 1.

[6] G. Foschini and M. Gans, "On limits of wireless communications in a fading environment when using multiple antennas," *Wireless Pers. Commun.*, vol. 6, no. 3, pp. 311–335, Mar. 1998. Cited in page 1.

[7] V. Tarokh, N. Seshadri, and A. Calderbank, "Space-time codes for high data rate wireless communication: performance criterion and code construction," *IEEE Trans. Inf. Theory*, vol. 44, no. 2, pp. 744–765, Mar. 1998. Cited in page 1.

[8] Lizhong Zheng and D. Tse, "Diversity and multiplexing: a fundamental tradeoff in multiple-antenna channels," *IEEE Trans. Inf. Theory*, vol. 49, no. 5, pp. 1073–1096, May 2003. Cited in page 1.

[9] S. Hara and R. Prasad, "Overview of multicarrier CDMA," *IEEE Commun. Mag.*, vol. 35, no. 12, pp. 126–133, 1997. Cited in page 1.

[10] P. Bender, P. Black, M. Grob, R. Padovani, N. Sindhushyana, and A. Viterbi, "CDMA/HDR: a bandwidth efficient high speed wireless data service for nomadic users," *IEEE Commun. Mag.*, vol. 38, no. 7, pp. 70–77, 7 2000. Cited in page 1.

[11] K.-K. Wong, R. Murch, R.-K. Cheng, and K. Letaief, "Optimizing the spectral efficiency of multiuser MIMO smart antenna systems," in *Proc. IEEE Wireless Commun. Netw. Conf. (WCNC)*, vol. 1, Chicago, IL, USA, Sep. 2000, pp. 426–430. Cited in page 1.

[12] S. Vishwanath, N. Jindal, and A. Goldsmith, "Duality, achievable rates, and sum-rate capacity of Gaussian MIMO broadcast channels," *IEEE Trans. Inf. Theory*, vol. 49, no. 10, pp. 2658–2668, Oct. 2003. Cited in page 1.

[13] K.-K. Wong, R. Murch, and K. Letaief, "A joint-channel diagonalization for multiuser MIMO antenna systems," *IEEE Trans. Wireless Commun.*, vol. 24, no. 5, pp. 773–786, May 2003. Cited in page 1.

[14] Q. Spencer, A. Swindlehurst, and M. Haardt, "Zero-forcing methods for downlink spatial multiplexing in multiuser MIMO channels," *IEEE Trans. Signal Process.*, vol. 52, no. 2, pp. 461–471, Feb. 2004. Cited in page 1.

[15] D. Gesbert, M. Kountouris, R. W. Heath, C.-b. Chae, and T. Salzer, "Shifting the MIMO paradigm," *IEEE Signal Proc. Mag.*, vol. 24, no. 5, pp. 36–46, Sep. 2007. Cited in page 1.

[16] H. Q. Ngo, E. G. Larsson, and T. L. Marzetta, "Energy and spectral efficiency of very large multiuser MIMO systems," *IEEE Trans. Commun.*, vol. 61, no. 4, pp. 1436–1449, Apr. 2013. Cited in page 1.

[17] E. G. Larsson, O. Edfors, F. Tufvesson, and T. L. Marzetta, "Massive MIMO for next generation wireless systems," *IEEE Commun. Mag.*, vol. 52, no. 2, pp. 186–195, Feb. 2014. Cited in page 1.

[18] X. You *et al.*, "Toward 6G TKμ extreme connectivity: Architecture, key technologies and experiments," *IEEE Wireless Commun.*, vol. 30, no. 3, pp. 86–95, Jun. 2023. Cited in page 1.

[19] Q. Shang, X. Chen, F. Tang, X. Cai, and M. Zhao, "Nash equilibrium-based spectrum pricing and allocation in satellite-terrestrial network," in *Proc. IEEE Int. Conf. Commun. Workshops (ICC Workshops)*, Denver, CO, USA, Jun. 2024, pp. 1901–1906. Cited in page 2.

[20] T. S. Rappaport *et al.*, "Millimeter wave mobile communications for 5G cellular: It will work!" *IEEE Access*, vol. 1, pp. 335–349, 2013. Cited in page 2.

[21] J. G. Andrews *et al.*, "What Will 5G Be?" *IEEE Journal on Selected Areas in Communications*, vol. 32, no. 6, pp. 1065–1082, Jun. 2014. Cited in page 2.

[22] J. Madden, *White Paper: 5G mmWave Repeaters Cut Costs in Half*, Mobile Experts, Aug. 2021. Cited in page 2.

[23] D. Johhson, "The 5G dilemma: More base stations, more antennas—less energy?" *IEEE Spectrum*, Oct. 2018, Accessed: Mar. 18, 2026. [Online]. Available: https://spectrum.ieee.org/will-increased-energy-consumption-be-the-achilles-heel-of-5g-networks Cited in page 2.

[24] T. S. Rappaport *et al.*, "Wireless communications and applications above 100 GHz: Opportunities and challenges for 6G and beyond," *IEEE Access*, vol. 7, pp. 78 729–78 757, 2019. Cited in page 2.

[25] N. Bhushan, Junyi Li, D. Malladi, R. Gilmore, D. Brenner, A. Damnjanovic, R. Sukhavasi, C. Patel, and S. Geirhofer, "Network densification: the dominant theme for wireless evolution into 5G," *IEEE Commun. Mag.*, vol. 52, no. 2, pp. 82–89, Feb. 2014. Cited in page 2.

[26] L. Song, X. Hu, G. Zhang, P. Spachos, K. N. Plataniotis, and H. Wu, "Networking systems of AI: On the convergence of computing and communications," *IEEE Internet of Things J.*, vol. 9, no. 20, pp. 20 352–20 381, Oct. 2022. Cited in page 3.

[27] K. B. Letaief, W. Chen, Y. Shi, J. Zhang, and Y.-J. A. Zhang, "The roadmap to 6G: AI empowered wireless networks," *IEEE Commun. Mag.*, vol. 57, no. 8, pp. 84–90, Aug. 2019. Cited in page 3.

[28] C.-X. Wang, M. D. Renzo, S. Stanczak, S. Wang, and E. G. Larsson, "Artificial intelligence enabled wireless networking for 5G and beyond: Recent advances and future challenges," *IEEE Wireless Commun.*, vol. 27, no. 1, pp. 16–23, Feb. 2020. Cited in page 3.

[29] Y. Satio, Y. Kishiyama, A. Benjebbour, T. Nakamura, A. Li, and K. Higuchi, "Non-orthogonal multiple access (NOMA) for cellular future radio access," in *Proc. IEEE 77th Veh. Technol. Conf. (VTC Spring)*, Dresden, Germany, Jun. 2013, pp. 1–5. Cited in page 3.

[30] K. Higuchi and Y. Kishiyama, "Non-orthogonal access with random beamforming and intra-beam SIC for cellular MIMO downlink," in *Proc. IEEE 78th Veh. Technol. Conf. (VTC Fall)*, Las Vegas, NV, USA, Sep. 2013, pp. 1–5. Cited in page 3.

[31] P. Wang, J. Xiao, and L. Ping, "Comparison of orthogonal and non-orthogonal approaches to future wireless cellular systems," *IEEE Veh. Technol. Mag.*, vol. 1, no. 3, pp. 4–11, Sep. 2006. Cited in page 3.

[32] Z. Ding, X. Lei, G. K. Karagiannidis, R. Schober, J. Yuan, and V. K. Bhargava, "A survey on non-orthogonal multiple access for 5G networks: Research challenges and future trends," *IEEE J. Sel. Areas Commun.*, vol. 35, no. 10, pp. 2181–2195, Oct. 2017. Cited in page 3.

[33] Y. Mao, O. Dizdar, B. Clerckx, R. Schober, P. Popovski, and H. V. Poor, "Rate-splitting multiple access: Fundamentals, survey, and future research trends," *IEEE Commun. Surveys Tut.*, vol. 24, no. 4, pp. 2073–2126, Fourthquarter 2022. Cited in page 3.

[34] K. Wong, K. Tong, Y. Zhang, and Z. Zhongbin, "Fluid antenna system for 6G: When Bruce Lee inspires wireless communications," *Electron. Lett.*, vol. 56, no. 24, pp. 1288–1290, Nov. 2020. Cited 3 times in pages 3, 8, and 17.

[35] K.-K. Wong, K.-F. Tong, Y. Shen, Y. Chen, and Y. Zhang, "Bruce Lee-inspired fluid antenna system: Six research topics and the potentials for 6G," *Frontiers in Commun. & Netw.*, vol. 3, no. 853416, Mar. 2022. Cited 2 times in pages 3 and 17.

[36] K.-K. Wong, A. Shojaeifard, K.-F. Tong, and Y. Zhang, "Fluid antenna systems," *IEEE Trans. Wireless Commun.*, vol. 20, no. 3, pp. 1950–1962, Mar. 2021. Cited 7 times in pages 4, 8, 10, 17, 22, 23, and 79.

[37] K.-K. Wong and K.-F. Tong, "Fluid antenna multiple access," *IEEE Trans. Wireless Commun.*, vol. 21, no. 7, pp. 4801–4815, Jul. 2022. Cited 5 times in pages 4, 19, 22, 31, and 77.

[38] K.-K. Wong, D. Morales-Jimenez, K.-F. Tong, and C.-B. Chae, "Slow fluid antenna multiple access," *IEEE Trans. Commun.*, vol. 71, no. 5, pp. 2831–2846, May 2023. Cited 15 times in pages 4, 30, 31, 32, 33, 41, 43, 47, 48, 77, 79, 89, 90, 91, and 92.

[39] K.-K. Wong, K.-F. Tong, Y. Chen, Y. Zhang, and C.-B. Chae, "Opportunistic fluid antenna multiple access," *IEEE Trans. Wireless Commun.*, vol. 22, no. 11, pp. 7819–7833, Nov. 2023. Cited 4 times in pages 4, 34, 61, and 62.

[40] N. C. Beaulieu and K. T. Hemachandra, "Novel simple representations for Gaussian class multivariate distributions with generalized correlation," *IEEE Trans. Inf. Theory*, vol. 57, no. 12, pp. 8072—8083, Dec. 2011. Cited 3 times in pages 4, 34, and 42.

[41] K.-K. Wong, K.-F. Tong, Y. Chen, and Y. Zhang, "Closed-form expressions for spatial correlation parameters for performance analysis of fluid antenna systems," *Electron. Lett.*, vol. 58, no. 11, pp. 454–457, May 2022. Cited 7 times in pages 4, 11, 23, 25, 41, 56, and 92.

[42] M. Khammassi, A. Kammoun, and M.-S. Alouini, "A new analytical approximation of the fluid antenna system channel," *IEEE Trans. Wireless Commun.*, vol. 22, no. 12, pp. 8843–8858, Dec. 2023. Cited 4 times in pages 4, 23, 24, and 34.

[43] W. K. New, K.-K. Wong, H. Xu, K.-F. Tong, and C.-B. Chae, "Fluid antenna system: New insights on outage probability and diversity gain," *IEEE Trans. Wireless Commun.*, vol. 23, no. 1, pp. 128–140, Jan. 2024. Cited in page 4.

[44] H. Xu, K.-K. Wong, W. K. New, and K.-F. Tong, "On outage probability for two-user fluid antenna multiple access," in *Proc. IEEE Int. Conf. Commun. (ICC)*, Rome, Italy, May 2023, pp. 2246–2251. Cited 3 times in pages 4, 24, and 34.

[45] P. Ramírez-Espinosa, D. Morales-Jimenez, and K.-K. Wong, "A new spatial block-correlation model for fluid antenna systems," *IEEE Trans. Wireless Commun.*, vol. 23, no. 11, pp. 15 829–15 843, Nov. 2024. Cited 10 times in pages 4, 23, 24, 25, 56, 57, 62, 63, 65, and 78.

[46] M. Nakagami, "The m-distribution—A general formula of intensity distribution of rapid fading," in *Statistical Methods in Radio Wave Propagation*, W. C. Hoffman, Ed. Pergamon, 1960, pp. 3–36. Cited 4 times in pages 4, 42, 60, and 75.

[47] L. Yuan, Q. Du, N. Yang, F. Fang, and N. Yang, "Performance analysis of IRS-aided short-packet NOMA systems over Nakagami-m fading channels," *IEEE Trans. Veh. Technol.*, vol. 72, no. 6, pp. 8228–8233, Jun. 2023. Cited in page 4.

[48] H. Zhao, Y. Liu, Y. Ni, J. Zhou, S. Qiao, and K. He, "Performance analysis of RIS-assisted D2D communication under Nakagami-m fading," *IEEE Trans. Veh. Technol.*, vol. 73, no. 1, pp. 1447–1452, Jan. 2024. Cited in page 4.

[49] R. Kumar, M. K. Shukla, V. Kumar, and R. Tripathi, "Dual-hop mixed FSO-RF wireless powered relaying system: Performance analysis with nonlinear energy harvesting," *IEEE Trans. Green Commun. Netw.*, vol. 9, no. 3, pp. 991–1002, Sep. 2025. Cited in page 4.

[50] M. Farooq, A. Khan, M. Alhussein, H. Mahmood, K. Aurangzeb, and S. Bhatia Khan, "Outage analysis of a cognitive radio system with Nakagami-m fading and cooperative decode and forward relaying," *IEEE Access*, vol. 12, pp. 144 565–144 578, 2024. Cited in page 4.

[51] M. Gao, G. Xu, Z. Song, Y. Cheng, and D. Niyato, "Performance analysis of random 3D mmWave-assisted UAV communication system," *IEEE Trans. Veh. Technol.*, pp. 1–16, 2024. Cited in page 4.

[52] S. Ghosh, K. Singh, H. Jung, C.-P. Li, and T. Q. Duong, "On the performance of rate splitting multiple access for ISAC in device-to-multi-device IoT communications," *IEEE Trans. Cogn. Commun. Netw.*, vol. 11, no. 1, pp. 333–348, Feb. 2025. Cited in page 4.

[53] K.-K. Wong, A. Shojaeifard, K.-F. Tong, and Y. Zhang, "Performance limits of fluid antenna systems," *IEEE Commun. Lett.*, vol. 24, no. 11, pp. 2469–2472, Nov. 2020. Cited 2 times in pages 8 and 17.

[54] S. Lee, *Be water, my friend: The teachings of Bruce Lee.* New York, NY, USA: Flatiron Books, 2020. Cited 2 times in pages 8 and 9.

[55] W.-J. Lu *et al.*, "Fluid antennas: Reshaping intrinsic properties for flexible radiation characteristics in intelligent wireless networks," *IEEE Commun. Mag.*, vol. 63, no. 5, pp. 40–45, May 2025. Cited in page 9.

[56] G. L. Stüber, *Principles of Mobile Communication*, 4th ed. Cham, Switzerland: Springer International Publishing, 2017. Cited 3 times in pages 11, 23, and 24.

[57] L. Zhu and K.-K. Wong, "Historical review of fluid antenna and movable antenna," *arXiv preprint*, Jan. 2024. [Online]. Available: http://arxiv.org/abs/2401.02362 Cited in page 11.

[58] L. Zhu, W. Ma, and R. Zhang, "Modeling and performance analysis for movable antenna enabled wireless communications," *IEEE Trans. Wireless Commun.*, vol. 23, no. 6, pp. 6234–6250, Jun. 2024. Cited in page 11.

[59] L. Zhu *et al.*, "A tutorial on movable antennas for wireless networks," *IEEE Commun. Surveys Tut.*, vol. 28, pp. 3002–3054, 2026. Cited in page 11.

[60] K.-F. Tong, B. Liu, and K.-K. Wong, "Designs and challenges in fluid antenna system hardware," *Electronics*, vol. 14, no. 7, p. 1458, Apr. 2025. Cited in page 12.

[61] Y. Shen *et al.*, "Design and experimental validation of mmWave surface wave enabled fluid antennas for future wireless communications," *IEEE Antennas & Wireless Prop. Lett.*, vol. 25, no. 4, pp. 1467–1471, Apr. 2026. Cited 2 times in pages 12 and 13.

[62] H. Wang, Y. Shen, K.-F. Tong, and K.-K. Wong, "Continuous electrowetting surface-wave fluid antenna for mobile communications," in *Proc. IEEE Region 10 Conference (TENCON)*, Hong Kong, China, Nov 2022, pp. 1–3. Cited in page 13.

[63] Z. Dong *et al.*, "Movable antenna for wireless communications: Prototyping and experimental results," *IEEE Trans. Wireless Commun.*, vol. 25, pp. 6586–6599, 2026. Cited in page 14.

[64] J. Zhang *et al.*, "A novel pixel-based reconfigurable antenna applied in fluid antenna systems with high switching speed," *IEEE Open J. Antennas & Propag.*, vol. 6, no. 1, pp. 212–228, Feb. 2025. Cited in page 14.

[65] B. Liu, T. Wu, K.-K. Wong, H. Wong, and K.-F. Tong, "Wideband pixel-based fluid antenna system: An antenna design for smart city," *IEEE Internet Things J.*, vol. 13, no. 4, pp. 6850–6862, Feb. 2026. Cited 2 times in pages 14 and 15.

[66] K.-K. Wong, C. Wang, S. Shen, C.-B. Chae, and R. Murch, "Reconfigurable pixel antennas meet fluid antenna systems: A paradigm shift to electromagnetic signal and information processing," *IEEE Wireless Commun.*, vol. 33, no. 1, pp. 191–198, Feb. 2026. Cited in page 14.

[67] B. Liu, K.-F. Tong, K.-K. Wong, C.-B. Chae, and H. Wong, "Programmable meta-fluid antenna for spatial multiplexing in fast fluctuating radio channels," *Optics Express*, vol. 33, no. 13, pp. 28 898–28 915, Jun. 2025. Cited 2 times in pages 15 and 16.

[68] D. Ma, B. Liu, J. Yang, Y. Fang, T. Wu, and K.-F. Tong, "Meta-fluid antenna-enabled multi-user ISAC: Architecture implementation, algorithm design, and full-wave validation," *IEEE J. Sel. Topics Signal Process.*, vol. 20, no. 3, pp. 247–261, Apr. 2026. Cited in page 15.

[69] H. Hong *et al.*, "A contemporary survey on fluid antenna systems: Fundamentals and networking perspectives," *IEEE Trans. Netw. Sci. Eng.*, vol. 13, pp. 2305–2328, 2026. Cited in page 16.

[70] W. K. New *et al.*, "A tutorial on fluid antenna system for 6G networks: Encompassing communication theory, optimization methods and hardware designs," *IEEE Commun.*

Surveys Tut., vol. 27, no. 4, pp. 2325–2377, Aug. 2025. Cited 3 times in pages 16, 17, and 19.

[71] P. D. Alvim, H. S. Silva, F. O. Barcelos, P. R. de Moura, U. S. Dias, O. S. Badarneh, and R. A. A. de Souza, "On the performance of fluid antenna systems under α-μ fading channels," *IEEE Wireless Commun. Lett.*, vol. 13, pp. 108–112, Jan. 2024. Cited in page 17.

[72] W. K. New, K.-K. Wong, H. Xu, K.-F. Tong, and C.-B. Chae, "An information-theoretic characterization of MIMO-FAS: Optimization, diversity-multiplexing tradeoff and q-outage capacity," *IEEE Trans. Wireless Commun.*, vol. 23, no. 6, pp. 5541–5556, Jun. 2024. Cited 3 times in pages 17, 26, and 27.

[73] A. Shojaeifard *et al.*, "MIMO evolution beyond 5G through reconfigurable intelligent surfaces and fluid antenna systems," *Proc. IEEE*, vol. 110, no. 9, pp. 1244–1265, Sep. 2022. Cited in page 18.

[74] K.-K. Wong, K.-F. Tong, and C.-B. Chae, "Fluid antenna system—part III: A new paradigm of distributed artificial scattering surfaces for massive connectivity," *IEEE Commun. Lett.*, vol. 27, no. 8, pp. 1929–1933, Aug. 2023. Cited in page 18.

[75] F. Rostami Ghadi, K.-K. Wong, W. K. New, H. Xu, R. Murch, and Y. Zhang, "On performance of RIS-aided fluid antenna systems," *IEEE Wireless Commun. Lett.*, vol. 13, no. 8, pp. 2175–2179, Aug. 2024. Cited in page 18.

[76] X. Lai, J. Yao, K. Zhi, T. Wu, D. Morales-Jimenez, and K.-K. Wong, "FAS-RIS: A block-correlation model analysis," *IEEE Trans. Veh. Technol.*, vol. 74, no. 2, pp. 3412–3417, Feb. 2025. Cited in page 18.

[77] J. Yao *et al.*, "A framework of FAS-RIS systems: Performance analysis and throughput optimization," *IEEE Trans. Wireless Commun.*, vol. 25, pp. 1333–1348, 2026. Cited in page 18.

[78] H. Xiao *et al.*, "Fluid Reconfigurable Intelligent Surfaces: Joint On-Off Selection and Beamforming With Discrete Phase Shifts," *IEEE Wireless Commun. Lett.*, vol. 14, no. 10, pp. 3124–3128, Oct. 2025. Cited in page 18.

[79] H. Yang, H. Xu, K.-K. Wong, C.-B. Chae, R. Murch, S. Jin, and Y. Zhang, "Position index modulation for fluid antenna system," *IEEE Trans. Wireless Commun.*, vol. 23, no. 11, pp. 16 773–16 787, Nov. 2024. Cited in page 18.

[80] X. Guo, Y. Xu, D. He, C. Zhang, H. Hong, K.-K. Wong, W. Zhang, and Y. Wu, "Fluid antenna index modulation for MIMO systems: Robust transmission and low-complexity detection," *IEEE Trans. Commun.*, vol. 73, no. 12, pp. 15 955–15 970, Dec. 2025. Cited in page 18.

[81] J. Yao *et al.*, "Rethinking hardware impairments in multi-user systems: Can FAS make a difference?" *IEEE Trans. Mobile Comput.*, vol. 25, no. 4, pp. 4965–4978, Apr. 2026. Cited in page 19.

[82] J. Zheng, J. Zhang, H. Du, D. Niyato, S. Sun, B. Ai, and K. B. Letaief, "Flexible-position MIMO for wireless communications: Fundamentals, challenges, and future directions," *IEEE Wireless Commun.*, vol. 31, no. 5, pp. 18–26, Oct. 2024. Cited in page 19.

[83] J. Zou *et al.*, "Shifting the ISAC trade-off with fluid antenna systems," *IEEE Wireless Commun. Lett.*, vol. 13, no. 12, pp. 3479–3483, Dec. 2024. Cited in page 20.

[84] C. Wang *et al.*, "Fluid antenna system liberating multiuser MIMO for ISAC via deep reinforcement learning," *IEEE Trans. Wireless Commun.*, vol. 23, no. 9, pp. 10 879–10 894, Sep. 2024. Cited 2 times in pages 20 and 38.

[85] E. Bastug, M. Bennis, and M. Debbah, "Living on the edge: The role of proactive caching in 5G wireless networks," *IEEE Commun. Mag.*, vol. 52, no. 8, pp. 82–89, Aug. 2014. Cited in page 20.

[86] F. Rostami Ghadi, K.-K. Wong, K.-F. Tong, and Y. Zhang, "Cache-enabled fluid antenna systems: Modeling and performance," *IEEE Commun. Lett.*, vol. 28, no. 8, pp. 1934–1938, Aug. 2024. Cited in page 20.

[87] X. Shi, X. Shao, B. Zheng, and R. Zhang, "6DMA-aided cell-free massive MIMO communication," *IEEE Wireless Commun. Lett.*, vol. 14, no. 5, pp. 1361–1365, May 2025. Cited in page 21.

[88] T. Han, Y. Zhu, K.-K. Wong, G. Zheng, and H. Shin, "Cell-free fluid antenna multiple access networks," *IEEE Trans. Wireless Commun.*, no. 9, pp. 7237–7251, Sep. 2025. Cited 6 times in pages 21, 68, 70, 74, 77, and 98.

[89] D. Bepari, S. Mondal, A. Bhowal, K. Singh, H. Shin, K.-K. Wong, and D. W. K. Ng, "Fluid antennas: Pioneering a new era in next-generation wireless communications," *IEEE Commun. Surveys Tut.*, vol. 28, pp. 5596–5631, 2026. Cited in page 21.

[90] W. Kiat New, K.-K. Wong, H. Xu, F. Rostami Ghadi, R. Murch, and C.-B. Chae, "Channel estimation and reconstruction in fluid antenna system: Oversampling is essential," *IEEE Trans. Wireless Commun.*, vol. 24, no. 1, pp. 309–322, Jan. 2025. Cited in page 28.

[91] Z. Chai, K.-K. Wong, K.-F. Tong, Y. Chen, and Y. Zhang, "Port selection for fluid antenna systems," *IEEE Commun. Lett.*, vol. 26, no. 5, pp. 1180–1184, May 2022. Cited in page 28.

[92] M. Eskandari, A. G. Burr, K. Cumanan, and K.-K. Wong, "cGAN-Based slow fluid antenna multiple access," *IEEE Wireless Commun. Lett.*, vol. 13, no. 10, pp. 2907–2911, Oct. 2024. Cited in page 28.

[93] J. Zou, S. Sun, and C. Wang, "Online learning-induced port selection for fluid antenna in dynamic channel environment," *IEEE Wireless Commun. Lett.*, vol. 13, no. 2, pp. 313–317, Feb. 2024. Cited in page 28.

[94] C. Skouroumounis and I. Krikidis, "Large-scale fluid antenna systems with linear MMSE channel estimation," in *Proc. IEEE Int. Conf. Commun. (ICC)*, Seoul, Korea, Republic of, May 2022, pp. 1330–1335. Cited in page 28.

[95] ——, "Fluid antenna with linear MMSE channel estimation for large-scale cellular networks," *IEEE Trans. Commun.*, vol. 71, no. 2, pp. 1112–1125, Feb. 2023. Cited in page 28.

[96] H. Xu *et al.*, "Channel estimation for FAS-assisted multiuser mmWave systems," *IEEE Commun. Lett.*, vol. 28, no. 3, pp. 632–636, Mar. 2024. Cited in page 28.

[97] B. Xu, Y. Chen, Q. Cui, X. Tao, and K.-K. Wong, "Sparse bayesian learning-based channel estimation for fluid antenna systems," *IEEE Wireless Commun. Lett.*, vol. 14, no. 2, pp. 325–329, Feb. 2025. Cited in page 29.

[98] W. K. New, K.-K. Wong, H. Xu, K.-F. Tong, and C.-B. Chae, "Achievability of fluid antenna multiple access: A Han-Kobayashi's comparison," in *IEEE Globecom Workshops (GC Wkshps)*, Kuala Lumpur, Malaysia, Dec. 2023, pp. 1201–1206. Cited in page 31.

[99] T. Han and K. Kobayashi, "A new achievable rate region for the interference channel," *IEEE Trans. Inf. Theory*, vol. 27, no. 1, pp. 49–60, Jan. 1981. Cited in page 31.

[100] R. H. Etkin, D. N. C. Tse, and H. Wang, "Gaussian interference channel capacity to within one bit," *IEEE Trans. Inf. Theory*, vol. 54, no. 12, pp. 5534–5562, Dec. 2008. Cited in page 31.

[101] A. Haghi and A. K. Khandani, "Boundary of the gaussian Han-Kobayashi rate region," *IEEE Trans. Inf. Theory*, vol. 67, no. Apr., pp. 2034–2054, 4 2021. Cited in page 31.

[102] K.-K. Wong, K.-F. Tong, Y. Chen, and Y. Zhang, "Fast fluid antenna multiple access enabling massive connectivity," *IEEE Commun. Lett.*, vol. 27, no. 2, pp. 711–715, Feb. 2023. Cited 3 times in pages 31, 32, and 36.

[103] K. Wong, K. Tong, Y. Chen, and Y. Zhang, "Extra-large MIMO enabling slow fluid antenna massive access for millimeter-wave bands," *Elect. Lett.*, vol. 58, no. 25, pp. 1016–1018, Dec. 2022. Cited 2 times in pages 32 and 33.

[104] Y. Chen, S. Li, Y. Hou, and X. Tao, "Energy-efficiency optimization for slow fluid antenna multiple access using mean-field game," *IEEE Wireless Commun. Lett.*, vol. 13, no. 4, pp. 915–918, Apr. 2024. Cited in page 33.

[105] J. D. Vega-Sánchez, H. R. C. Mora, N. V. O. Garzón, and D. P. M. Osorio, "A tractable approximation for evaluating the performance of slow fluid antenna multiple access," *IEEE Open J. Commun. Soc.*, vol. 6, pp. 3614–3623, 2025. Cited in page 33.

[106] H. Yang, K.-K. Wong, K.-F. Tong, Y. Zhang, and C.-B. Chae, "Performance analysis of slow fluid antenna multiple access in noisy channels using Gauss-Laguerre and Gauss-

Hermite quadratures," *IEEE Commun. Lett.*, vol. 27, no. 7, pp. 1734–1738, Jul. 2023. Cited in page 33.

[107] H. Xu, K.-K. Wong, W. K. New, K.-F. Tong, Y. Zhang, and C.-B. Chae, "Revisiting outage probability analysis for two-user fluid antenna multiple access system," *IEEE Trans. Wireless Commun.*, vol. 23, no. 8, pp. 9534–9548, Aug. 2024. Cited in page 34.

[108] H. Hong *et al.*, "Fluid antenna multiple access for 6G: A holistic review," *IEEE Open J. Commun. Soc.*, vol. 7, pp. 2607–2633, 2026. Cited in page 34.

[109] N. Waqar, K.-K. Wong, C.-B. Chae, R. Murch, S. Jin, and A. Sharples, "Opportunistic fluid antenna multiple access via team-inspired reinforcement learning," *IEEE Trans. Wireless Commun.*, vol. 23, no. 9, pp. 12 068–12 083, Sep. 2024. Cited 2 times in pages 35 and 61.

[110] K.-K. Wong, C.-B. Chae, and K.-F. Tong, "Compact ultra massive antenna array: A simple open-loop massive connectivity scheme," *IEEE Trans. Wireless Commun.*, vol. 23, pp. 6279–6294, Jun. 2024. Cited in page 36.

[111] K.-K. Wong, "Transmitter CSI-free RIS-randomized CUMA for extreme massive connectivity," *IEEE Open J. Commun. Soc.*, vol. 5, pp. 6890–6902, 2024. Cited in page 36.

[112] H. Hong, K.-K. Wong, K.-F. Tong, H. Shin, and Y. Zhang, "Coded fluid antenna multiple access over fast fading channels," *IEEE Wireless Commun. Lett.*, vol. 14, no. 4, pp. 1249–1253, Apr. 2025. Cited in page 36.

[113] N. Waqar, K.-K. Wong, C.-B. Chae, and R. Murch, "Turbocharging fluid antenna multiple access," *IEEE Trans. Wireless Commun.*, vol. 25, pp. 4038–4052, 2026. Cited in page 36.

[114] H. Hong, K.-K. Wong, H. Xu, Y. Xu, H. Shin, R. Murch, D. He, and W. Zhang, "Downlink OFDM-FAMA in 5G-NR systems," *IEEE Trans. Wireless Commun.*, vol. 24, no. 12, pp. 10 116–10 132, Dec. 2025. Cited 2 times in pages 39 and 40.

[115] *Study on channel model for frequencies from 0.5 to 100 GHz: Release 19*, TR38.901 v19.2.0, 3GPP, Dec. 2025. [Online]. Available: https://www.3gpp.org/ftp/Specs/archive/38_series/38.901/38901-i00.zip Cited in page 39.

[116] J. G. Proakis and M. Salehi, *Digital Communications*, 5th ed. New York, NY, USA: McGraw-Hill, 2008. Cited 6 times in pages 44, 45, 82, 83, 94, and 95.

[117] N. Y. Ermolova and O. Tirkkonen, "Laplace transform of product of generalized Marcum Q, Bessel I, and power functions with applications," *IEEE Trans. Signal Process.*, vol. 62, no. 11, pp. 2938–2944, Jun. 2014. Cited 3 times in pages 47, 73, and 76.

[118] F. R. Ghadi, K.-K. Wong, F. Javier López-Martínez, H. Shin, and L. Hanzo, "Performance analysis of FAS-aided NOMA-ISAC: A backscattering scenario," *IEEE Internet of Things J.*, vol. 12, no. 23, pp. 51 326–51 340, Dec. 2025. Cited in page 49.

[119] E. W. Weisstein, "Laguerre-Gauss Quadrature," MathWorld–A Wolfram Resource, https://mathworld.wolfram.com/Laguerre-GaussQuadrature.html (accessed Aug. 14, 2025). Cited 2 times in pages 59 and 72.

[120] I. Gradshteyn and I. Ryzhik, *Table of Integrals, Series, and Products*, 7th ed., D. Zwillinger and A. Jeffrey, Eds. San Diego, USA: Elsevier Science & Technology, 2007. Cited 2 times in pages 59 and 97.

[121] H. Q. Ngo, A. Ashikhmin, H. Yang, E. G. Larsson, and T. L. Marzetta, "Cell-free massive MIMO: Uniformly great service for everyone," in *Proc. IEEE 16th Int. Workshop Signal Process. Advances Wireless Commun. (SPAWC)*, Jun. 2015, pp. 201–205. Cited in page 68.

[122] ——, "Cell-free massive MIMO versus small cells," *IEEE Trans. Wireless Commun.*, vol. 16, no. 3, pp. 1834–1850, Mar. 2017. Cited in page 68.

[123] N. Beaulieu and C. Cheng, "Efficient Nakagami-m fading channel simulation," *IEEE Trans. Veh. Techn.*, vol. 54, no. 2, pp. 413–424, Mar. 2005. Cited in page 78.

[124] M. K. Simon, *Probability Distributions Involving Gaussian Random Variables: A Handbook for Engineers and Scientists.* Boston, MA: Springer US, 2006. Cited in page 90.

[125] M. Abramowitz and I. A. Stegun, Eds., *Handbook of Mathematical Functions With Formulas, Graphs, and Mathematical Tables*, ser. NBS Applied Mathematics, Series 55. Washington, DC, USA: National Bureau of Standards, 1964. Cited in page 93.